Immunoanalytics – Core Facility and Research Group
Helmholtz Center Munich
Group leader: Prof. Dr. Elfriede Nößner

Profiling human tumor infiltrating leukocytes comparing renal cell and hepatocellular carcinoma

Dissertation
to obtain the Doctorate in Natural Sciences
at the Faculty of Medicine
Ludwig-Maximilians-University Munich

submitted by
Julia Schnappinger
from Munich
2018

Printed with permission of the Faculty of Medicine
Ludwig-Maximilians-University Munich

Supervisor: Prof. Dr. rer. nat. Eflriede Nößner

Co-supervisor: Prof. Dr. Ludger Klein

Dean of the faculty: Prof. Dr. med.dent. Reinhard Hickel

Day of oral examination: January 9th, 2019

To my beloved parents

Karin and Gerhard Schnappinger

1 Table of Contents

1 Table of Contents 4
2 Summary 8
3 Zusammenfassung 9
4 Introduction 11
4.1 The immune system 11
4.1.1 Innate and adaptive immunity 11
4.1.2 T cell immunity 13
4.1.2.1 Initiation of T cell immunity: TCR signaling and co-stimulation 13
4.1.2.2 Regulation of T cell immunity: signaling cross-talks and co-inhibition 15
4.1.2.3 T cell unresponsiveness: anergy and exhaustion 16
4.2 Tumor immunology 17
4.3 Renal cell carcinoma (RCC) 18
4.4 Hepatocellular carcinoma (HCC) 19
5 Objective of this thesis 20
6 Material and Methods 22
6.1 Materials 22
6.1.1 Consumables and Equipment 22
6.1.2 Reagents 23
6.1.3 Media and buffers for cell culture and tissue preparation 24
6.1.4 Buffers for flow cytometry 25
6.1.5 Cell lines 26
6.1.6 Primary antibodies for flow cytometry 26
6.1.7 Secondary antibodies for flow cytometry 29
6.1.8 Reagents for T-cell stimulation assays 29
6.1.9 Peripheral blood mononuclear cells and tissue suspensions 30
6.1.10 HCC Patients 30
6.1.11 RCC patients 32

6.2 Methods 33
6.2.1 Cell culture techniques 33
6.2.1.1 Determination of cell counts 33
6.2.1.2 Freezing and thawing of cells 33
6.2.1.3 Cultivation of adherent cell lines 33
6.2.1.4 Generation of activated T cells 34
6.2.2 Isolation techniques of leukocytes 34
6.2.2.1 Isolation of PBMC from whole blood samples 34
6.2.2.2 Preparation of tissue suspensions 35
6.2.3 Functional assays 36
6.2.3.1 Stimulation of TIL with ImmunoCult™ human T cell activators 37
6.2.3.2 Rationale of stimulation with ImmunoCult™ human T cell activators 37
6.2.3.3 Negative controls 39
6.2.3.4 Stimulation with PMA/Ionomycin 39
6.2.4 Multiparameter flow cytometry 40
6.2.4.1 Staining combinations 42
6.2.4.2 Sample Preparation for flow cytometry 43
6.2.4.3 Compensation beads and compensation matrix 45
6.2.4.4 Flow-Count Fluorospheres 46
6.2.4.5 Data acquisition 47
6.2.5 Statistical analysis 48
6.2.5.1 Mann-Whitney U test 48
6.2.5.2 Wilcoxon matched pairs signed-rank test 48
6.2.5.3 Kruskal-Wallis test, Friedmann test and Dunn´s Post-hoc comparisons 48
6.2.5.4 Spearman´s rank correlation 48
7 Results 50
7.1 Characterization of the organ-resident immune cell infiltrate comparing non-tumor with tumor tissue of kidney and liver 50
7.1.1 Experimental setup 50
7.1.1.1 Gating strategy 51

7.1.2 Composition of the organ-resident immune cell infiltrates 54
7.1.3 Patient-specific deviations of immune cell infiltrates 55
7.1.4 T cell subset distribution in leukocytes of non-tumor and tumor tissue of kidney and liver 59
7.2 Functional responsiveness of $CD8^+$ RCC-TIL and HCC-TIL 61
7.2.1 T cells with function 62
7.2.2 Functional profile of $CD8^+$ TIL 64
7.2.3 Can markers of proliferation (Ki-67), PD-1 or CD28 delineate T cell function of TIL? 67
7.3 Cell cycle state of TIL 71
7.4 The AKT-pathway in TIL 75
7.4.1 The AKT-pathway is poorly active in TIL 76
7.4.2 The influence of AKT on cell cycle progression in TIL 78
7.4.2.1 pAKT(S473) suppresses $p27^{kip1}$ in TIL 78
7.4.2.2 High percentages of cyclin E are independent of AKT phosphorylation 81
7.4.3 Cross-talk of AKT- and MAPK-pathway 83
7.4.3.1 Positivity of pAKT excludes positivity of pERK in TIL 83
7.4.3.2 Positivity of pERK predicts cell cycle state of TIL 85
7.5 The mTOR-pathway in TIL 88
7.5.1 The mTOR-pathway is impaired in TIL 89
7.5.2 $pmTOR^+prpS6^+$ divides TIL into two groups 91
7.5.3 Phosphorylated mTOR and rpS6 determine perforin positivity in TIL 92
7.6 T cell anergy in $CD8^+$ TIL 95
7.6.1 DGK-α expression divides RCC-TIL and HCC-TIL into two groups 97
7.6.2 DGK-α correlates with expression of FoxO1 in $CD8^+$ TIL 98
7.7 Exhaustion in $CD8^+$ TIL 99
7.7.1 PD-1 is enriched in $CD8^+$ TIL 99
7.7.2 RCC-TIL and HCC-TIL have low frequencies of T cells co-expressing PD-1 and LAG-3 102
7.7.2.1 Ki-67 is expressed in $PD\text{-}1^+LAG\text{-}3^+$ $CD8^+$ TIL 104

7.7.3 Transcription factors T-bet and Eomes, and PD-1 in $CD8^+$ TIL 107

7.7.3.1 $Tbet^{low}/Eomes^+/PD\text{-}1^+$ expression in $CD8^+$ HCC-TIL identifies two groups of HCC patients 108

7.7.3.2 $T\text{-}bet^{low}/Eomes^+$ TIL express granzyme B but not perforin 112

7.7.3.3 Cytotoxic state of CTL in TIL is defined by perforin expression 114

7.7.3.4 Frequency analysis of perforin and granzyme B co-expression in $CD8^+$ TIL 117

7.8 Individual profiles of $CD8^+$ TIL based on anergic characteristics, PD-1, cytotoxic molecules and Ki-67 119

8 Discussion 121

8.1 Hypo-responsiveness of $CD8^+$ RCC-TIL and HCC-TIL 121

8.2 Different types of unresponsiveness in $CD8^+$ RCC-TIL and HCC-TIL 126

8.3 “Best-fit” treatments based on $CD8^+$ TIL profiles 129

9 Abbreviations 131

10 References 136

11 Publications 143

12 Acknowledgements 144

13 Affidavit 146

2 Summary

Renal cell carcinoma (RCC) and hepatocellular carcinoma (HCC) are tumors that arise in immunologically different backgrounds. HCC develops almost always in the context of chronic inflammation in a categorical immuno-tolerogenic milieu of the liver while RCC has no evident inflammation driven etiology. Both tumors harbor tumor-infiltrating lymphocytes (TIL), but tumors are not eradicated although spontaneous tumor-specific immune responses have been reported. Through checkpoint blockade therapy, T cell responses can be re-invigorated to achieve clinically successful tumor eradication, but only in a small subgroup of patients. To provide a better understanding of the deviations in antitumor immune response hindering effective tumor control, several multi-parameter antibody panels were designed which might allow insight into the mechanisms of T cell hypo-responsiveness. The panels addressed the composition of the immune cell infiltrate as well as the functional response of $CD8^+$ T cells, combined with markers of cell cycle, cytotoxic state, signaling cascades downstream of the T cell receptor and co-stimulation. Furthermore, transcription factors associated with anergy and exhaustion were analyzed.

$CD8^+$ RCC-TIL and HCC-TIL did not respond to anti-CD3 stimulation with no rescue through added co-stimulation and still diminished response to PMA/I stimulation, in particular in RCC-TIL. Deeper depression of RCC-TIL compared to HCC-TIL was seen in many features including even less Ki-67 and cyclin E, pAKT(S473), as well as perforin in RCC-TIL compared to HCC-TIL. An overall very low presence of these markers was a hallmark in all TIL. A connection between mTOR- and rpS6-pathway activation and perforin expression could be established. An interrupted mTOR pathway in many T cells in TIL provided a rationale for observed perforin deficits. Subgroups of RCC-TIL and HCC-TIL showed increased DGK-α, indicating an anergic state. T cells defined by the transcription factors T-bet and Eomes and the exhaustion marker PD-1 were detected in all $CD8^+$ RCC-TIL but divided HCC-TIL into two groups that had or did not have T-bet^{low}/$Eomes^+$/PD-1^+ T cells. Patient groups based on features of $CD8^+$ TIL such as anergy, non-lytic state, PD-1, or senescence included TIL from both RCC and HCC. However, better lytic state (perforin$^+$granzyme B^+) characterized one group of HCC-TIL and distinguished them from RCC-TIL.

3 Zusammenfassung

Das Nierenzellkarzinom (renal cell carcinoma, RCC) und das Leberkarzinom (hepatocellular carcinoma, HCC) entstehen unter unterschiedlichen immunologischen Voraussetzungen. Das HCC entwickelt sich fast immer in der Folge einer vorausgehenden chronischen Entzündung, die durch Immuntoleranzmechanismen in der Leber begünstigt ist. Das RCC dagegen entsteht unabhängig von einer Entzündung. In beiden Tumorentitäten werden tumor-spezifische Immunantworten nachgewiesen, die jedoch zur Elimination des Tumors nicht ausreichend sind. Checkpoint Blockade Therapie, die eine inhibierte T-Zellantwort re-aktivieren kann, zeigt bei beiden Tumorentitäten klinisch erfolgreiche Tumorregression – allerdings nur bei einer kleine Patientengruppe.

Um die Veränderungen der T-Zellen, die einer erfolgreichen Bekämpfung des Tumors entgegen stehen, besser zu verstehen, wurden Gewebesuspensionen von RCC und HCC mittels Vielfarben-Durchflusszytometrie analysiert. Die Zusammensetzung des Immunzellinfiltrats wurde ebenso analysiert wie der funktionelle Zustand der $CD8^+$ tumor-infiltrierenden Leukozyten (TIL). Außerdem waren verschiedene Marker Teil der Analysen, die den Zellzyklus, die Signalkaskaden des T-Zellrezeptors sowie AKT- und mTOR-Signalwege abbilden. Des Weiteren wurden die TIL in Bezug auf Transkriptionsfaktoren, die im Zusammenhang mit T-Zell-Anergie und Erschöpfung stehen, sowie der zytotoxe Zustand der T-Zellen untersucht.

Weder Stimulation mit anti-CD3 noch mit anti-CD3/anti-CD28 löste eine funktionelle Antwort in $CD8^+$ RCC-TIL und HCC-TIL aus; auch eine Stimulation mit PMA/I konnte keine starke Reaktion induzieren, was besonders für RCC-TIL der Fall war. TIL beider Tumorentitäten wiesen niedrige Positivität an Ki-67, Cyclin E, pAKT(S473) sowie Perforin auf, wobei der Mangel in RCC-TIL stärker ausgeprägt war als es in HCC-TIL der Fall war. Des Weiteren konnte eine Verbindung zwischen dem mTOR-rpS6 Signalweg und Perforin hergestellt werden. Da die Signalweiterleitung von mTOR zu rpS6 in einigen TIL beider Tumorentitäten unterbrochen war, könnte dies den Mangel an Perforin in TIL erklären. In sowohl RCC-TIL als auch HCC-TIL zeigte ein Teil der T-Zellen Anzeichen von T-Zell-Anergie, die sich durch erhöhte Level an DGK-α darstellten. Ferner wurden T-Zellen identifiziert, die durch die Anwesenheit der Transkriptionsfaktoren T-bet und Eomes sowie durch den mit Erschöpfung assoziierten Marker PD-1 gekennzeichnet waren. Diese T-Zellen ($T\text{-}bet^{low}/Eomes^+/PD\text{-}1^+$) wurden in allen RCC-Patienten gefunden, allerdings nur in einer Untergruppe der HCC-Patienten. RCC-TIL und HCC-TIL konnten,

basierend auf T-Zelleigenschaften der Anergie, lytischem Status, der Anwesenheit von PD-1 oder seneszenter T-Zellen in Gruppen eingeteilt werden. Die Gruppen waren Tumorentität-übergreifend, jedoch die Gruppe mit ausgeprägtem lytischen T-Zellstatus beinhaltete fast ausschließlich TIL von HCC.

4 Introduction

4.1 The immune system

Protection against diseases and restoration of health is mediated by the immune system which recognizes and eliminates intruding pathogens such as viruses, bacteria and worms. Each organ or tissue has its own immunological challenges and requirements, such as preventing immune response to commensal bacteria in the gut or setting the right threshold of immune activation in organs that are constantly exposed to environmental challenges. The presence of different components and organ-specific characteristics of the immune system help to establish the appropriate immune network. Immune cells and also soluble factors are connected by activation and inhibition, resulting in a carefully balanced interplay (10).

4.1.1 Innate and adaptive immunity

First defense against intruding micro-organisms is mediated by innate immunity. Its cells recognize a broad spectrum of microorganisms by pattern-recognizing receptors (PRR) that bind to repetitive and conserved structures on the surface of micro-organisms (pathogen associated molecular patterns, PAMP). PRRs do not need to be induced which allows a fast recognition and elimination of pathogens within minutes or hours. Examples for PRRs are toll-like receptors (TLRs) which are expressed on the surface of macrophages. Their activation results in production of pro-inflammatory cytokines like IL-6 and TNF-α, and also in expression of co-stimulatory receptors that are necessary for induction of the adaptive immunity. Other cellular players of innate immunity are natural killer cells (NK cells) which are activated by cytokines released by macrophages (IFN-α and IFN-β). NK cells are specialized to identify virus-infected cells by recognizing altered structures of MHC I (major histocompatibility complex) on the cell surface, mediated by two families of receptors: killer cell lectin-like receptors (KLR) and killer cell immunoglobulin like receptors (KIR). Both groups have activating and inhibiting structures, and the presence of intact MHC I molecules prevents NK cells from eliminating healthy cells. Once activated, NK cells release cytokines (IFN-γ) and cytotoxic granules containing perforin and granzyme B which can eliminate target cells. Antigen presenting cells (APCs) like dendritic cells (DCs) connect both the innate and the adaptive immunity by phagocytosis, processing of pathogens and presentation of fragmented pathogens by MHC-II molecules to $CD4^+$ T cells. Furthermore, virus-infected DCs can also present viral

peptides by MHC-I molecules on their cell surface which leads to activation and differentiation of naïve $CD8^+$ T cells (10).

In contrast to innate immunity, adaptive immunity is highly specific against pathogens. Cellular components are B and T lymphocytes which become activated when they have recognized antigens by their highly specific receptors (B cell receptor: BCR; T cell receptor: TCR). The TCR is restricted to major histocompatibility complexes (MHC), meaning it can only recognize antigen-derived peptide fragments presented by MHC molecules I or II. There is a main difference between peptide MHC complex (pMHC) I and II, which is that MHC I is expressed on cells having a nucleus, as nearly all cells of the body have, whereas MHC II is present on APCs. Furthermore, the presented peptides are different: MHC I molecules present peptides that have been produced in the cytosol (e.g. virus particles) and MHC II molecules bind peptides that derive from vesicles and have been previously absorbed by phagocytes (10).

In addition to TCR, T cells also express co-receptors which can either bind to MHC I (co-receptor CD8) or to MHC II (co-receptor CD4). $CD4^+$ T cells are T helper cells (T_H cells) that cross talk to other cellular compartments of the innate or adaptive immune system. T_H1 cells activate $CD8^+$ T cells and macrophages, T_H2 cells induce antibody production by stimulation of B cells and T_H17 cells induce inflammation by activation of neutrophil granulocytes. Regulatory $CD4^+$ T cells (Treg) can stop immune responses or suppress unwanted responses against self-antigens or harmless pathogens. Treg cells can be identified by the surface markers CD3, CD4, CD25 and transcription factor FoxP3 (10).

One subgroup of $CD8^+$ T cells are cytotoxic T cells (CTL). They trigger apoptosis in their target cells by releasing cytotoxic proteins like perforin and granzyme B which enter the target cell through its plasma membrane. Once in the cytoplasm, granzyme B induces apoptosis of the target cell by activation of caspases. Exocytosis of cytotoxic granules perforin and granzyme B is also named degranulation. It can be addressed by detection of membrane glycoproteins of lysosomes (e.g. CD107a) on the cell surface. Apoptosis of the target cell can also be induced by engagement of FAS (CD95, death receptor) expressed on the target cell and FAS-L (CD95-L, ligand of death receptor) on activated CTL. Production of cytokines like IFN-γ is another key function of CTL. IFN-γ activates macrophages and upregulates expression of MHC I and MHC II molecules and the corresponding machinery of antigen presentation (10).

4.1.2 T cell immunity

T cell progenitors derive from the bone marrow and complete their development in the thymus. When released into the blood stream, naïve T cells migrate to secondary lymphoid organs and get in contact with APCs that present peptides produced by the cell itself, altered self-proteins by mutations or pathogens by MHC I molecules. After engagement of TCR with antigens presented by MHC I molecules on APCs, naïve T cells develop to effector cells (10). Furthermore, clonal selection enables to generate memory T cells which mediate a fast reaction against recurring pathogens.

$CD8^+$ T cell subgroups of naïve, effector and memory T cells can be discriminated amongst other markers (CD62-L, CD95, CD45RA, CD45RO) by the expression patterns of the transcription factors T-bet and Eomesodermin (Eomes) (11–15). T-bet and Eomes are also related to perforin and granzyme B expression which is a hallmark for CTL (11,12,16).

4.1.2.1 Initiation of T cell immunity: TCR signaling and co-stimulation

Ligation of TCR and cognate pMHC initiate a signal cascade, but TCR heterodimers lack kinase activity and are thus not capable by themselves to forward signals. TCR exists in complex with four CD3 molecules (ε-δ; γ-ε) which contain immunoreceptor tyrosine-based activation motifs (ITAMs) that are phosphorylated by tyrosine kinases Fyn and LCK (Src family) upon TCR-pMHC engagement. The phosphorylation state activates downstream protein kinase ZAP70 and LAT (linker of activation in T cells) by ZAP70. LAT transmits the TCR-pMHC signal to phospholipase C-γ (PLC-γ) and the MAPK signaling cascade. PLC-γ generates the second messengers DAG (diacylglycerol) and IP_3 (inositol-1,4,5-trisphosphat). IP_3 leads to a release of calcium ions (Ca^{2+}) from the endoplasmatic reticulum, resulting in dephosphorylation of NFAT (nuclear factor of activated T cells) which induces gene transcription of cytokines (e.g. IL-2) or co-inhibitory receptor PD-1 (programmed cell death protein 1).

Activation of MAP (mitogen-activated protein) kinase cascade by DAG results in activation of ERK (extracellular signal-related kinase) and association of transcription regulating complex AP-1 (activating protein 1). One part of AP-1 is protein kinase JNK (c-Jun N-terminale kinase) which is activated by ERK or LAT. The AP-1 complex induces transcription of cytokines (IL-2, IFN-γ, TNF-α) and degranulation. Furthermore, DAG activates protein kinase C-θ (PKC- θ), resulting in activation of NFκB (nuclear factor “kappa light chain” of activated B cells). NFκB is kept inactive by complex formation with

IκB (inhibitor of NFκB). IκB dissociates from NFκB when phosphorylated and when Ca^{2+} is present. The transcription factor NFκB can then enter the nucleus and activate gene transcription, e.g. of cytokines such as IL-2.

Combined function of AP-1, NFAT and NFκB is the stimulation of gene expression of cytokine IL-2 which is essential for T cell proliferation and differentiation into effector cells. IL-2 gene expression is only induced when AP-1, NFAT and NFκB are bound to the IL-2 promotor (10).

An overview of the TCR signaling and involved pathways, regulations and cross-talks is summarized in figure 1.

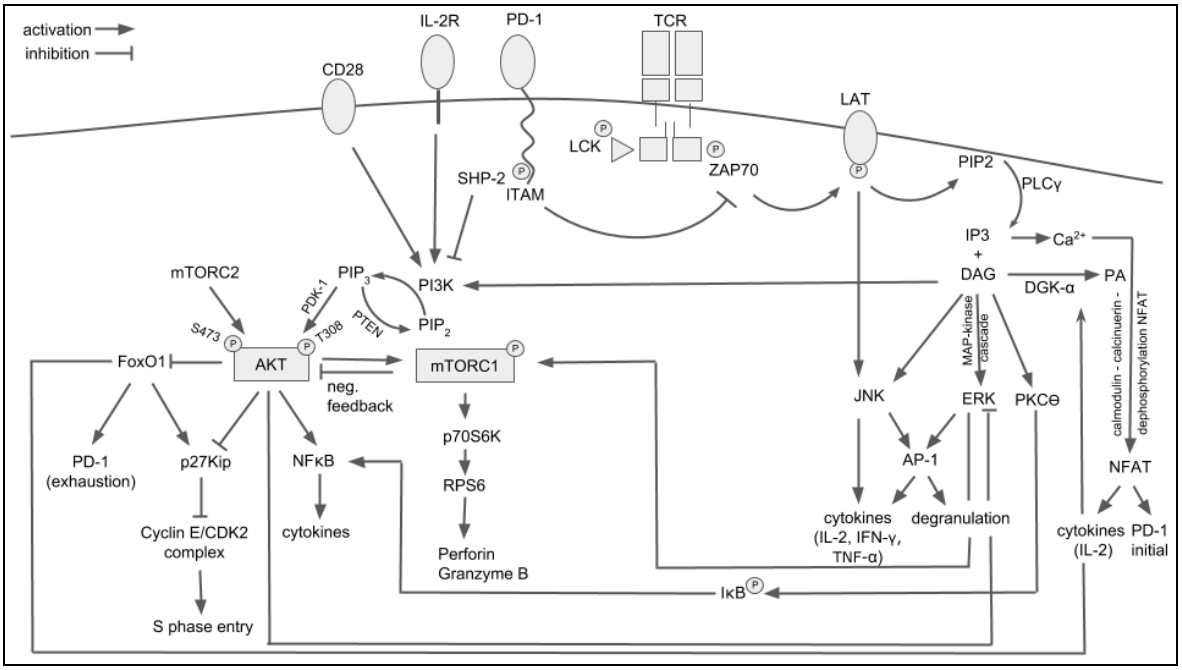

Figure 1: TCR signaling and its cross-talk to AKT- and mTOR-pathways
CD28: co-stimulatory receptor. IL-2R: receptor of IL-2. PD-1: co-inhibitory receptor. TCR: T cell receptor. LCK, Fyn: kinases of the Src family. ITAMs: immunoreceptor tyrosine-based activation motif. ZAP70: tyrosinase-protein kinase ZAP70. LAT: linker of activated T cells. PIP_2: phosphatidyl-inositol-4,5-bisphosphat. IP_3: inositol-1,4,5-trisphosphat. PLC-γ: phosphor lipase C- γ. DAG: diacylglycerol. DGK-α: diacylglycerolkinase-α. PA: phosphatidic acid. NFAT: nuclear factor of activated T cells. ERK: extracellular signal-related kinase. AP-1: activating protein 1. JNK: c-Jun N-terminale kinase. PI3K: phosphoinositide-3-kinase, PIP_3:phosphatidyl-inositol-3,4,5-trisphosphat. PTEN: phosphatase and Tensin homolog. PDK-1: phosphoinositide dependent kinase-1. AKT: protein kinase B. mTORC1/C2: mammalian target of rapamycin complex 1/2. FoxO1: forkhead box protein 1. $p27^{kip1}$: CDK inhibitor. CDK2: cylin dependent kinase 2. NFκB: nuclear factor “kappa light chain” of activated B cells. p70S6K: p70 ribosomal protein kinase S6. rpS6: ribosomal protein S6. IκB: inhibitor of NFκB.

Ligation of TCR by pMHC is the first signal to drive development of effector function and the second required signal is co-stimulation, mediated through the co-stimulatory receptor CD28 on T cells. It enhances the TCR signaling as well as it drives T cell proliferation and survival, activating the AKT (aka protein kinase B) and mTOR (mammalian target of rapamycin) -pathways.

In detail, the co-stimulatory receptor CD28 binds to its ligands CD80 and CD86 expressed on APCs leading to phosphorylation of the intracellular signaling domain YMNM of CD28. This results in activation of PI3K (phosphoinositide-3-kinase) (17), which can also be activated by IL-2 receptor (IL-2R) signaling (18). The functions of PI3K are mediated by PIP_3 (phosphatidyl-inositol-3,4,5-trisphosphat), which is produced by PI3K by phosphorylation of PIP_2 (phosphatidyl-inositol-4,5-bisphosphat). PI3K signaling can be inversely regulated by dephosphorylation of PIP_3 by phosphatase PTEN (phosphatase and tensin homolog) into PIP_2 (19). PIP_3 is necessary to activate PDK-1 (phosphoinositide dependent kinase-1) that subsequently phosphorylates serine/threonine kinase AKT at T308. AKT is fully activated together with at S473, mediated by mTORC2 (mammalian target of rapamycin, complex 2) (20). One downstream target of AKT is the transcription factor FoxO1 (forkhead box protein 1); phosphorylation of FoxO1 by AKT inhibits nuclear translocation and activity of FoxO1 (21). In its active not phosphorylated form, FoxO1 can enter the nucleus and then sustains expression of PD-1 (21), CDK inhibitor $p27^{kip1}$ (22) and DGK-α (18,23). Furthermore, AKT can induce activation of NFκB and can also initiate cell cycle progression by suppressing CDK (cyclin dependent kinase) inhibitor $p27^{kip1}$ and subsequently activating cyclin E/CDK2 complexes which lead to S phase entry (20,24-27). AKT is also capable to phosphorylate mTORC1 (mammalian target of rapamycin, complex 1) (20), but mTORC1 can also inhibit AKT as a negative feedback loop (28). Downstream signaling of mTORC1 is mediated by its catalytic subunit raptor (regulatory-associated protein of mTOR). Raptor phosphorylates p70 ribosomal protein kinase S6 (p70S6) which leads to phosphorylation of ribosomal protein S6 (rpS6) that finally induces gene translation (29). Furthermore, mTORC1 promotes effector differentiation of $CD8^+$ T cells by gene regulation of cytotoxic effector molecules perforin, granzyme B or IFN-γ (30).

4.1.2.2 Regulation of T cell immunity: signaling cross-talks and co-inhibition

Cross-inhibition between different pathways leads to negative regulation of an upstream component of another pathway resulting in inhibition of the other pathway´s signal (31). Cross-inhibition between AKT- and MAPK-pathways have been reported (20,31), indicating that T cells can either proliferate as induced by AKT-pathway or be functional active by ERK (and MAPK cascade) mediated degranulation. Cross-activation between different signaling pathways was also found and is defined by positive regulation of upstream components of one pathway by a mediator of a second pathway thereby increasing the first pathway´s activity (31). This has been reported for the mTOR-pathway and the MAPK cascade; ERK can lead to mTORC1 activation (31), indicating that T cell function like degranulation induced by MAPK cascade (ERK) and mTORC1 mediated

production of the cytotoxic molecules perforin and granzyme B are both necessary to provide target cell toxicity.

After intruded microorganism or degenerated cells are eliminated, activation of CTL needs to be terminated. Co-inhibitory receptors or inhibitory checkpoints are expressed on the surface of CTL after activation and negatively regulate a wide spectrum of T cell function like proliferation, cytokine production and expression of cytotoxic molecules like perforin and granzyme B (32). Examples for inhibitory receptors are, amongst others, lymphocyte activation gene 3 (LAG-3), TIM-3 (T cell immunoglobulin and mucin-domain containing-3), programmed cell death protein 1 (PD-1), or CTLA-4 (cytotoxic T cell associated protein 4). In more detail, LAG-3 associates with the TCR and engages with MHC molecules. Downstream functions are decreased intracellular levels of Ca^{2+} (33) which lead to suppression of NFAT and MAP kinase cascades. PD-1 is a transmembrane receptor of the immunoglobulin superfamily and after ligation with its ligands PD-L1 or PD-L2 (expressed on APCs or tumor cells), downstream impact of PD-1 is suppression of PI3K (34) which results in suppression of AKT and mTOR pathway and subsequent decrease of proliferation and cytokine production. CTL-A4 is transmembrane glycoprotein of the immunoglobulin superfamily. As a homologue of CD28, the ligands of CTLA-4, CD80 and CD86 are well described, but downstream signaling of CTL-A4 has not been fully understood yet (32).

4.1.2.3 T cell unresponsiveness: anergy and exhaustion

Different states of T cell unresponsiveness have been reported, and T cell anergy and exhaustion are explained in the following.

T cell anergy has been described as a mechanism of unresponsiveness, in which T cells are functionally inactivated after stimulation without co-stimuation. Anergic T cells remain alive but are in a hyporesponsive state (35). First experiments that induced T cell anergy were performed with murine T cells. T cells were stimulated with fixed APCs which cannot upregulate co-stimulatory ligands, then anergic T cells developed, producing less IL-2 as when co-cultured with live APCs (36). This led to the conclusion that anergy arises from incomplete T cell activation, e.g. ligation of TCR but lacking the co-stimulatory signal (35). Indeed, stimulation with antigens only engaged to TCR alone without additional co-stimulation induced anergy in T_H1 cells (37). Besides the incomplete activation by lacking the co-stimulatory signal, anergic T cells were in a growth arrested state and showed a block in the MAPK pathway by poor activation of ERK and JNK pathways which can be completely reverted by IL-2 (35). Interestingly, PMA and Ionomycin usually induce IL-2

production and proliferation, however, anergic T cells were only partly revived after PMA/I treatment (35). The anergic state was connected to high expression of DGK-α as anergic T_H1 cells were characterized by overexpression of DGK-α, suppression of ERK activation and reduced IL-2 production after anti-CD3/anti-CD28 stimulation (38). In the tumor microenvironment, hypo-responsiveness was found in human T cells engineered with a chimeric antigen receptor (CAR) after trafficking to tumors, proliferated but rapidly lost their functional activity resulting in limited therapeutic effect. These CAR-T cells were characterized by high levels of DGK-α and blocking DGK-α decreased the defects in tumor cell killing (39). Also $CD8^+$ tumor-infiltrating leukocytes (TIL) of renal cell carcinoma (RCC) showed hallmarks of anergy being unresponsive to anti-CD3 stimulation, demonstrating reduced phosphorylation of ERK and JNK, and they had high levels of DGK-α. Low dose IL-2 and also inhibition of DGK-α led to improved ERK phosphorylation and lytic granule exocytosis (40).

T cell exhaustion defines a state of dysfunction characterized by loss of IL-2 production, proliferation and killing capacity. Exhaustion is thought to develop due to antigen persistence in chronic infection and cancer, and is described by multiple expression of co-inhibitory receptors on the surface of CTL (41,42). The state of exhaustion has been shown to be reverted by blocking the inhibitory checkpoints PD-1 and CTL-A4 *in-vivo* in a mouse model of chronic LCMV infection (43) and blocking of CTLA-4 and PD-L1 resulted in major tumor regression in patients with metastatic melanoma (44).

4.2 Tumor immunology

The immune system does not only protect from intruding microorganisms but also eliminates degenerated cells such as tumor cells. Indeed, TIL were found in different tumors, amongst others also in RCC (45,46) and in hepatocellular carcinoma (HCC) (47). Correlations between the levels of the immune cell infiltration of tumors and the clinical outcome have been investigated. A strong infiltration has been associated with good clinical outcome in different tumor entities (48). Additionally, the tumor infiltrating immune cells in human colorectal cancers were characterized and provided a better prediction of patient survival as the histopathological methods that were used to stage colorectal cancer (49). Taken together, this indicates that characterization of the immune contexture meaning type, density and location of immune cells has developed into a useful adjunct tool to predict patients´ prognosis (48,49).

Nevertheless, the question remains why tumors emerge and progress although TIL invade into tumors. Different mechanisms of tumor immune escape have been described (50):

Loss of antigenicity was found due to loss of immunogenic tumor antigen expression or defects in the antigen presentation such as loss of MHC expression or dysregulation of antigen processing machinery. Decreased immunogenicity of tumors has been reported by upregulation of immuno-inhibitory ligands such as PD-L1 and the presence of co-inhibitory molecules like PD-1, LAG-3 or TIM-3 and their ligation inhibiting the function of TIL. A suppressive tumor microenvironment also plays a role in tumor immune escape by the presence of inhibitory immune cell subsets such as regulatory T cells or myeloid-derived suppressor cells (MDSCs). Additionally, the intruding TIL can have deficits themselves; TCRs might not recognize tumor associated antigens (TAAs) or T cells recognize the corresponding TAA but T cell function is intrinsically impaired. With regard to RCC, $CD8^+$ TIL that recognize the corresponding TAA (6,46) were found in the tumor microenvironment but did not eliminate tumor cells but TIL regained anti-tumor functionality after cultivation (4–6,40).

It has been described above (see p. 15) that T cell immunity can be regulated by co-inhibitory receptors (inhibitory checkpoints) and the hyporesponsive state of T cell exhaustion is characterized by expression of multiple co-inhibitory receptors on T cells. Blocking of the inhibitory checkpoints PD-1 and CTLA-4 successfully reverted T cell exhaustion in a mouse model of chronic LCMV infection (43). Checkpoint inhibitors have also entered clinical treatment and the promising response rates of tumor regression in some patients led to the approval of several checkpoint inhibitor antibodies (anti-PD-1, anti-PD-L1, anti-CTLA-4) by the U.S: Food and Drug Administration (FDA) for treatments of several tumor entities. For example, treatment with ipilimumab (anti-CTLA-4) was approved after successful studies in melanoma in 2011 (51). Among other tumor entities, successful studies of nivolumab (anti-PD-1) in HCC patients showed overall response rates of 18% (52) and approval of nivolumab by the FDA was granted in September 2017. Furthermore, nivolumab was approved as second-line treatment for RCC in 2016 (53) and was additionally approved in combination with ipilimumab by the FDA just recently (April 2018) as frontline therapy for intermediate and poor-risk patients with advanced RCC (54,55).

4.3 Renal cell carcinoma (RCC)

Renal cell carcinoma (RCC) derives from luminal cells of the proximal tubulus and is an epithelial tumor. Due to lack of symptoms, RCC is diagnosed in late stages and one third of initially surgically treated patients relapse or are diagnosed with metastasis (56). Within several subgroups of RCC, clear cell RCC (ccRCC) is most frequent (70%) followed by papillary (10% – 15%) and chromophobe (5%) tumors.

RCC is considered as an immune responsive tumor defined by several criteria: i) in the 1990 (before discovery of immune checkpoints), it was shown that some patients responded to immunotherapy using high-dose IL-2 or IL-2 and IFN-α (1–3), ii) in rare cases, spontaneous remission of primary tumors or metastasis have been observed (9) and iii) TIL isolated from RCC tissues showed anti-tumor activity after cultivation *in-vitro* (4–6). Altogether, these findings indicate that immunotherapy of RCC might be successful but it still remains unclear why RCCs are strongly infiltrated by effector cells but tumor are not rejected (45) and response rates to checkpoint blockade therapy are not higher than 25% (52).

For non-metastatic ccRCC, first line therapy suggests tumor resection whereby nephrectomy should be prevented if possible (57). First line therapy for metastatic ccRCC indicates VEGF-inhibitors or sunitinib. Yet, resistance develops commonly after target therapy. Checkpoint inhibitor nivolumab (anti-PD-1) is an approved second line treatment option after resistance to tyrosine kinase inhibitors (57). However, objective response rates of 25% (52) are promising but further optimization is needed.

4.4 Hepatocellular carcinoma (HCC)

Hepatocellular carcinoma (HCC) is the sixth most common cancer worldwide, survival rates of HCC patients are very low and only 20% of patients are still alive one year after diagnosis (8). Because HCC develops from underlying liver diseases, HCC patients suffer from liver dysfunction and the malignancy of the tumor. To evaluate treatment options for HCC patients, the Barcelona Clinic Liver Cancer (BCLC) stages allow classification of HCC patients not only by tumor burden characterized by pTNM (pathological tumor node metastasis) staging but also severity of the underlying liver disease, and general health conditions of the patients are taken into account (58,59). Depending on the different BCLC stages, different treatment options as surgery, liver transplantation, radiofrequency ablation (RFA), transarterial chemoembolization (TACE) are suggested. The multi-kinase inhibitor sorafenib prolongs survival up to three months (58,59). Until now, first and second line therapy in Germany do not recommend immunotherapy for HCC patients (58).

Nevertheless, HCC is an interesting candidate for immunotherapy because it develops in the context of an immune-tolerant milieu of the liver. Due its physiologic function which is filtration of toxic waste, environmental agents and bacteria from the GI tract, the liver is exposed to an enormous load of antigens (7). Tolerogenic mechanisms prevent the liver from organ-autoimmune damage due to ongoing stimulation by antigens (7,60,61). Amongst others, tolerogenic mechanisms are decreased surface expression of co-stimulatory molecules (61), cross-presenting liver sinusoidal endothelial cells (LSECs) that

induce memory T cells instead of CTL (62) and increased expression of PD-L1 on hepatocytes, hepatic stellate cells, LSECs and Kupffer cells (7). Taken together, the tolerogenic milieu eases HCC development when underlying diseases additionally foster inflammation.

Indeed, HCC develops from underlying diseases or infections (8,63); for example chronic viral infection with hepatitis B (HBV) or C (HCV) are risk factors that cause liver tumors (7). After HBV vaccines have been introduced in 1980s, a decrease of HCC was reported. However, obesity, diabetes and subsequent non-alcoholic steatohepatitis (NASH) are growing risk factors for HCC (7). Furthermore, alcohol abuse first leads to fibrotic and in long term to cirrhotic modifications of the liver and 90% of HCC developed from cirrhosis (8). It appears logical that the tolerogenic milieu of the liver and concurrent immune suppression in combination with chronic inflammation eases tumor development (7). When tumors are established, the immunosuppressive microenvironment of the tumor hampers successful tumor eradication by the immune system (7). Despite unfavorable conditions for tumor eradication, spontaneous tumor-specific adaptive immune responses have been reported in HCC patients and tumor-specific CTL against the tumor-associated antigens (TAAs) NY-ESO and glypican–3 (GPC3) have been identified (7). This indicates that anti-tumor immunity does exist in HCC, but effector activity is suppressed. This raises hope that antitumor immunity might be reinvigorated if the underlying immune suppressive mechanisms are counteracted. Therefore, HCC was regarded as a candidate for immunotherapy and indeed, nivolumab (anti-PD-1) showed clinical responses in a subset of 20% of patients (52).

5 Objective of this thesis

RCC is characterized as an immune responsive tumor harboring TIL that show anti-tumor activity when removed from the tumor and cultured in vivo (1–6). Already in the 1980s, it was shown that RCC patients respond to systemic cytokine therapy (high dose IL-2) and immune-modifiers such as IFN-α (1–3). The environment of HCC is influenced by immune-tolerogenic mechanisms that favor tumor formation once the liver has been damaged (7,8). In both RCC and HCC, spontaneous tumor-specific immune responses have been reported (7,9) which makes both tumor entities good candidates for immunotherapy. Indeed, current trials using nivolumab have shown objective response rates of 25% (55,64) in ccRCC and of 20% in non-viral HCC (52). It still remains unclear why response rates are relatively low.

This thesis aims to further elucidate defects of tumor infiltrating lymphocytes (TIL) beyond the checkpoint inhibition that prevent tumor eradication with special focus on the comparison of $CD8^+$ TIL of ccRCC and non-viral HCC. Due to the distinct immunological environments of RCC and HCC, it was hypothesized that defects of RCC-TIL and HCC-TIL might be different. Furthermore, it was of interest to identify targets that might help to improve immunotherapy outcome in both tumor entities.

Tissue suspensions of RCC and HCC tissues were prepared and analyzed without previous cultivation or separation of specific leukocyte subsets in order to best preserve the features of the immune cell composition and its possible deviation from active immunity. With the help of multi-parameter flow cytometry, the composition of the immune cell infiltrate in general as well as the functional state of $CD8^+$ T cells in particular was addressed. Markers with regard to cell cycle progression, signaling cascades of the T cell receptor and the co-stimulatory pathway, markers associated with anergy and exhaustion as well as the cytotoxic state were assessed to obtain insight into the mechanisms of T cell hypo-responsiveness.

6 Material and Methods

6.1 Materials

6.1.1 Consumables and Equipment

Table 1: Consumables and equipment

Consumable/Equipment	Company
ArC amine reactive compensation Kit	Thermo Fisher Scientific/Caltag, Waltham, Massachusetts
Balance, PC 400 DeltaRange	Mettler, Gießen, Germany
Cell Strainer 100 µm	BD Pharmingen, Heidelberg, Germany
Centrifuge, Megafuge 2.0 R	Heraeus Instruments, Hanau, Germany
Cover glass for Neubauer counting chambers, 20 x 26 mm, depth 0,4 mm	Hirschmann Laborgeräte, Eberstadt, Germany
Freezing vials, 1,5 ml	Nunc, Wiesbaden, Germany
Incubator	Hereaus Instruments, Hanau, Germany
Light microscopes: Leica DMLS Zeiss Axioskop	Leica Microsystems, Heidelberg, Germany Carl Zeiss Micro Imaging GmbH, Göttingen, Germany
Mr Frosty™ freezing container	Thermo Fisher Scientific/Caltag, Waltham, Massachusetts
Mulit-well plates, polysterene 96-wellplates (non-tissue culture treated)	Corning Incorporated, Corning, NY, USA
Multistepper	Eppendorf, Hamburg, Germany
Neubauer counting chamber, depth 0,1 mm	Gesellschaft für Laborbedarf Würzburg, Würzburg, Germany
Nitrogen tank	Messer Griesheim, Krefeld, Germany
Nutating mixer	VWR International, Ismaning, Germany
Pasteur pipettes, glass	Josef Peske GmbH & Co KG, München, Germany
Pipettes and tips 1 to10 µl, 10 to 200 µl, 200 to 1000 µl	Eppendorf, Hamburg, Germany
Pipette tips for pipettor glass: 2 ml, 5 ml, 10 ml, 20 ml disposable: 10 ml, 25 ml	Hirschmann Laborgeräte, Eberstadt, Germany Greiner bio-one, Frickenhausen, Germany
Pipettor Pipetus®	Hirschmann Laborgeräte, Eberstadt, Germany

Consumable/Equipment	Company
Sterile laminar flow hood	BDK Luft- und Reinraumtechnik GmbH, Sonnenbühl-Genkingen, Germany
Syringes for multistepper, 2,5 ml, 5 ml	Hartenstein, Würzburg, Germany Eppendorf, Hamburg, Germany
Syringes for tissue sample preparation (10ml)	BD Biosciences, Heidelberg, Germany
Tissue culture flasks, 75 cm^2	Greiner bio-one, Frickenhausen, Germany
Tubes for flow cytometry, polypropylene 1 ml, 5 ml	Greiner bio-one, Frickenhausen, Germany Becton Dickinson Falcon, Heidelberg, Germany
Tubes, Polypropylene, 1,5 ml, 2 ml, 15 ml, 50 ml	Eppendorf, Hamburg, Germany
Vortexer MS1 Minishaker	KA Werke GmbH & Co KG, Staufen, Germany
Water bath	Köttermann Labortechnik, Uetze, Germany

6.1.2 Reagents

Table 2: Reagents

Reagent	Company
Accutase®	PAA Laboratories, Cölbe, Germany
Aqua ad iniectabilia	B. Braun, Melsungen, Germany
ArC amine reactive compensation Kit	Thermo Fisher Scientific/Caltag, Waltham, Massachusetts
Brefeldin A	eBioscience, Frankfurt, Germany
BSA (bovine serum albumin)	Sigma-Aldrich, Taufkirchen, Germany
Collagenase IA	Sigma-Aldrich, Taufkirchen, Germany
CompBeads (anti-mouse IgG, κ)	BD Biosciences, Heidelberg, Germany
Dimethylformamide	Sigma-Aldrich, Taufkirchen, Germany
Distilled and filtered water, non-sterile	Millipore, Schwalbach, Germany
DNase I	Sigma-Aldrich, Taufkirchen
Dulbecco's phosphate buffered saline (DPBS)	GIBCO by Life Technologies, Darmstadt, Germany
Ethanol	Merck, Darmstadt, Germany
Ethylenediaminetetraacetic acid (EDTA)	GIBCO by Life Technologies, Darmstadt, Germany
Fetal bovine serum (FBS)	Biochrome, Berlin, Germany
Ficoll® (Pancoll, density 1.077 g/ml)	Pan Biotech, Aidenbach, Germany

Reagent	Company
Flow-Count Fluoroshperes	Beckman Coulter, Galway, Ireland
Glucose monohydrate	Merck, Darmstadt, Germany
HCl solution (2 mol/l, 2 N)	Merck, Darmstadt, Germany
Heparin-sodium	B. Braun, Melsungen, Germany
HEPES	Sigma Aldrich, Taufkirchen, Germany
Human serum (HS)	In-house production (Helmholtz-Center Munich)
Ionomycin	Sigma Aldrich, Taufkirchen, Germany
L-glutamine	GIBCO by Life Technologies, Darmstadt, Germany
LIVE/DEAD™ Fixable Blue Dead Cell Staining Kit	Thermo Fisher Scientific/Caltag, Waltham, Massachusetts, USA
Monensin (BD GolgiStop©)	BD Pharmingen, Heidelberg, Germany
Non-essential amino acids	GIBCO by Life Technologies, Darmstadt, Germany
Paraformaldehyde (PFA)	Merck, Darmstadt, Germany
Penicillin/streptomycin	GIBCO by Life Technologies, Darmstadt, Germany
Percoll ®	Sigma Aldrich, Taufkirchen, Germany
Phorbol- 12- myristate- 13- acetate (PMA)	Sigma Aldrich, Taufkirchen, Germany
Recombinant IL-2	Cancernova GmbH, Reute, Germany
Saponin	Merck, Darmstadt, Germany
Sodium azide	Merck, Darmstadt, Germany
Sodium pyruvate	GIBCO by Life Technologies, Darmstadt, Germany
Trypan blue	Sigma-Aldrich, Taufkirchen, Germany
Trypsin-EDTA	GIBCO by Life Technologies, Darmstadt, Germany

6.1.3 Media and buffers for cell culture and tissue preparation

Table 3: Media and buffers

Medium / buffer	Formulate / Company
2 x Trypsin / EDTA	PBS + 20 % 10 x trypsin / EDTA
Buffer for digestion	RPMI 1640 + 0.1% BSA + 1% Penicillin/streptomycin + 10 mM HEPES + 800 (U/ml collagenase Ia)

Medium / buffer	Formulate / Company
Dulbecco's phosphate buffered saline (DPBS)	GIBCO by Life Technologies, Darmstadt, Germany
Erythrocytes lysis buffer (10X)	16.5 g ammonium chloride 2 g potassium chloride 74 mg Na-EDTA ad 200 ml aqua dest. pH adjustment: 7.3 – 7.4
Freezing Medium Classic without serum	Ibidi GmbH, Martinsried, Germany
Hanks Balanced Salt Solution (HBSS) containing Mg^{2+} and Ca^{2+} (1.26 mM $CaCl_2$/0.5 mM $MgCl_2$)	GIBCO by Life Technologies, Darmstadt, Germany
Hanks Balanced Salt Solution (HBSS), 10X without Mg^{2+} and Ca^{2+}	GIBCO by Life Technologies, Darmstadt, Germany
LCL-Medium	RPMI III + 10% FBS
Opti-MEM	GIBCO by Life Technologies, Darmstadt, Germany
Phosphate buffered saline (PBS)	GIBCO by Life Technologies, Darmstadt, Germany
Roswell Park Memorial Institute (RPMI)-1640 medium without L-glutamine	GIBCO by Life Technologies, Darmstadt, Germany
RPMI III	RPMI 1640 + 2 mM L-glutamine + 1 mM sodiumpyruvat + 1 mM non-essential amino acids
Thawing and stimulation medium for PBMC, activated T cells, NIL and TIL	RPMI III + 10% human serum

6.1.4 Buffers for flow cytometry

Table 4: Buffers for flow cytometry

Buffer	Formulate/Company
BD Cytofix/Cytoperm Fixation/Permeabilisation Kit	BD Biosciences, Heidelberg
BD Horizon™ Brilliant Stain Buffer	BD Biosciences, Heidelberg, Germany
BD Phosflow™ Perm Buffer III	BD Biosciences, Heidelberg, Germany
Cytofix™ Fixation Buffer	BD Biosciences, Heidelberg, Germany
FACS fixation buffer	in-house production: PBS + 1% PFA
FACS permeabilization buffer containing saponin (0.1%; 0.35%)	PBS + 0.1 or 0.35% saponin + 2% HS

Buffer	Formulate/Company
Fluorescence activated cell sorting (FACS) buffer	PBS + 2 mM EDTA + 1 % HS + 0,1% sodium azide
Transcription Factor Buffer Set	BD Biosciences, Heidelberg, Germany

6.1.5 Cell lines

Table 5: Cell lines

Name	Characteristics	Medium for cultivation	Source
activated T cells	PBMC transduced to stably express the HLA-A2 restricted tyrosinase-specific TCR T58 (see p. 34)	directly thawed before experiments	in-house production
P815	mouse-mastocytoma cell line TIB-64™	LCL-medium	ATCC, Rockville, Maryland, USA

6.1.6 Primary antibodies for flow cytometry

Table 6: Primary antibodies for flow cytometry

Target/ epitope	Species	Isotype	Clone	Fluoro-chrome	Dilution	Appli-cation	Company
CD3	mouse	IgG1 κ	SK7	PerCp-Cy™5.5	1:10	surface	eBioscience, Frankfurt, Germany
CD3	mouse	IgG1 κ	UCHT1	Alexa Fluor® A700	1:25	surface	Biolegend, London, UK
CD4	mouse	IgG1 κ	RPA-T4	APC-eFluor 780	1:25	surface	eBioscience, Frankfurt, Germany
CD8a	mouse	IgG1 κ	RPA-T8	V500	1:8	surface	BD Biosciences, Heidelberg, Germany
CD14	mouse	IgG2a κ	M5E2	PB	1:8	surface	Biolegend, London, UK
CD19	mouse	IgG1 κ	HIB19	Alexa Fluor® A700	1:8	surface	BD Biosciences, Heidelberg, Germany

Target/ epitope	Species	Isotype	Clone	Fluoro-chrome	Dilution	Appli-cation	Company
CD19	mouse	IgG1 κ	HIB19	BV421	1:50	surface	BD Biosciences, Heidelberg, Germany
CD20	mouse	IgG2b κ	2H7	Alexa Fluor® A700	1:50	surface	Biolegend, London, UK
CD20	mouse	IgG2a	H1	BV421	1:50	surface	BD Biosciences, Heidelberg, Germany
CD45	mouse	IgG1 κ	HI30	Pe-Cy7	1:25	surface	Biolegend, London, UK
CD56	mouse	IgG1 κ	B159	V450	1:10	surface	BD Biosciences, Heidelberg, Germany
CD56	mouse	IgG2b	NCAM16.2	BV421	1:50	surface	BD Biosciences, Heidelberg, Germany
CD107a	mouse	IgG1 κ	H4A3	APC	1:10	surface	Biolegend, London, UK
cyclin E	mouse	IgG2b κ	HE12	FITC	1:2,5	intra-cellular	Santa Cruz Biotechnology, Dallas, USA
DGK-α	mouse	IgG2a κ	3G7	unmarked	1:100	intra-cellular	LSBio, Seattle, USA
Eomes	mouse	IgG1 κ	WD1928	PE	1:100	intra-cellular	eBioscience, Frankfurt, Germany
FoxO1	mouse	polyclonal	polyclonal	unmarked	1:50	intra-cellular	Cell Signaling, Leiden, Netherlands
granzyme B	mouse	IgG1 κ	GB11	PE-TexasRed®	1:8	intra-cellular	Thermo Fisher Scientific/ Caltag, Waltham, Massachusetts
Ki-67	mouse	IgG1 κ	Ki-67	Alexa Fluor® A488	1:10	intra-cellular	Biolegend, London, UK
LAG-3 (CD223)	mouse	IgG1	17B4	ATTO 647N	1:100	intra-cellular	Biomol, Hamburg, Germany

Target/ epitope	Species	Isotype	Clone	Fluoro-chrome	Dilution	Appli-cation	Company
$p27^{kip1}$	mouse	IgG1 κ	F-8	PE	1:10	intra-cellular	Santa Cruz Biotechnolog, Dallas, USA
pAKT (S473)	mouse	IgG1 κ	M89-61	V450	1:10	intra-cellular	BD Biosciences, Heidelberg, Germany
perforin	mouse	IgG2b, κ	dG9	FITC	1:10	intra-cellular	BD Biosciences, Heidelberg, Germany
pmTOR (S2448)	mouse	IgG1 κ	O21-404	Alexa Fluor® 647	1:10	intra-cellular	BD Biosciences, Heidelberg, Germany
p-p44/42 MAPK (pERK; T202/Y204)	rabbit	polyclonal	polyclonal	unmarked	1:100	intra-cellular	Cell Signaling, Leiden, Netherlands
PD-1 (CD279)	mouse	IgG1 κ	eBioJ105	PE	1:8	surface	eBioscience, Frankfurt, Germany
PD-1 (CD279)	mouse	IgG1 κ	eBioJ105	PerCp-eFluor 710	1:8	surface	eBiosciencen Frankfurt, Germany
prps6 (S244)	mouse	IgG1 κ	N5-676	PE	1:10	intra-cellular	BD Biosciences, Heidelberg, Germany
T-bet	mouse	IgG1 κ	4B10	eFluor™ 660	1:10	intra-cellular	eBioscience, Frankfurt, Germany
IFN-γ	mouse	IgG1 κ	4S.B3	PerCp-Cy™5.5	1:10	intra-cellular	Biolegend, London, UK

6.1.7 Secondary antibodies for flow cytometry

Table 7: Secondary antibodies for flow cytometry

Specificity	Species	Clone	Fluoro-chrome	Dilution	Application	Company
anti-mouse IgG2a	goat	polyclonal	Alexa Fluor® 488	1:200	intracellular	Thermo Fisher Scientific/Caltag, Waltham, Massachusetts
anti-rabbit	goat	polyclonal	Alexa Fluor® 647	1:500	intracellular	Thermo Fisher Scientific/Caltag, Waltham, Massachusetts

6.1.8 Reagents for T-cell stimulation assays

ImmunoCult™ (StemCell™ Technologies) human T cell activators consist of tetrameric antibody complexes designed for T cell activation and expansion without the use of magnetic beads.

Table 8: Immuno™ Cult T cell activators

ImmunoCult™ T cell activator	Antibodies
CD3	Anti-human CD3 monospecific tetrameric antibody complex
CD3/CD28	Anti-human CD3 monospecific tetrameric antibody complex Anti-human CD28 monospecific tetrameric antibody complex

Table 9: Antibodies for T cell stimulation assays

Target/ epitope	Species	Isotype	Clone	Company
CD3	mouse	IgG2a	OKT3	In-house production
CD28	mouse	IgG1	CD28.2	BD Pharmingen, Heidelberg, Germany
used as isotype control	mouse	IgG1	MOPC21	BD Pharmingen, Heidelberg, Germany

6.1.9 Peripheral blood mononuclear cells and tissue suspensions

Peripheral blood mononuclear cells (PBMC) were obtained from healthy donors (n=16). Donors consented to the donation and blood collection was approved by the ethics committee.

Table 10: PBMC and tissue suspensions

Name	Characteristics	Source
NIL (infiltrating leukocytes from non-tumor-harboring tissue samples)	Tissue suspension of non-tumor tissue generated by mechanically mincing and enzymactic digestion	Tissue from macroscopically tumor-free area of tumor-harboring organ (liver or kidney) of HCC or RCC patients
PBMC (peripheral blood mononuclear cells)	peripheral blood mononuclear cells isolated from whole blood of healthy donors	Healthy donors
TIL (tumor-infiltrating leukocytes)	Tissue suspension of tumor tissue generated by mechanically mincing and enzymatic digestion of tissue samples	Macroscopically judged tumor-harboring area of liver or kidney of HCC or RCC patients

6.1.10 HCC Patients

Tissues, blood samples and corresponding data from HCC patients (tumor samples n=14 and corresponding non-tumor tissue n=10) were provided by the Biobank under the Administration of the Human Tissue and Cell Research (HTCR) Foundation at the Hospital of the University of Munich. Tissues and data from a database approved by a data protection officer from the HTCR Foundation were provided anonymized (double-coded). The framework of HTCR Foundation (65), which includes obtained written informed consent from all donors, has been approved by the ethics commission of the Faculty of Medicine in the University of Munich (No. 025-12) as well as the Bavarian State Medical Association (No. 11142). All HCC-patients were negatively tested for hepatitis A, B or C infection (non-viral HCC). Infiltrating leukocytes from hepatic non-tumor-harboring tissue samples are named as h-NIL and tumor infiltrating leukocytes are named as HCC-TIL when compared with samples of RCC patients.

Table 11: Clinical-pathological characteristics of non-viral HCC patients
[1]The age classes of the patients were provided within ranges by the HTCR
[2]classification according to guidelines of Union International Contre le Cancer (UICC); T: extent of the primary tumor. N: absence or presence of regional lymph node metastasis. M: absence or presence of distant metastasis. L: lymphatic invasion, V: venous invasion. R: residual tumor after resection. G: histopathological grading. x: not specified

Patient ID and tissue type	Sex	Age range[1] (at time of tumor resection)	TNM-Stage[2]	Pathological abnormalities of tumor tissue
HCC4 (NIL, TIL)	male	70-79	pT2 pN0 Mx L0 V2 R0 G2	steatosis, fibrosis, cirrhosis
HCC7 (NIL)	male	60-69	pT2 pN0 Mx L0 V1 R0 G3	fibrosis
HCC9 (TIL)	male	70-79	pT4 pNx Mx L1 V0 R1 G3	steatosis
HCC12 (TIL)	male	60-69	pTx pNx Mx Lx Vx Rx G2	steatosis
HCC13 (NIL, TIL)	male	70-79	pT1 pN0 Mx L0 V0 R1 G2	fibrosis
HCC16 (NIL, TIL)	female	70-79	pT1 pNx Mx L0 V0 R0 G2	steatosis
HCC17 (NIL, TIL)	male	60-69	pT2 pNx M1 L0 V1 R1 G2	none
HCC19 (NIL, TIL)	female	40-49	pT1 pN0 Mx L0 V0 R0 G2	none
HCC20 (NIL, TIL)	male	60-69	pT2a pN0 Mx[3] L0 V1 R0 G2	steatosis
HCC21 (NIL, TIL)	female	70-79	pT1 pNx Mx L0 V0 R0 G2	steatosis
HCC22 (TIL)	male	70-79	pT3 pNx Mx L0 V1 G2	none
HCC23 (TIL)	female	70-79	pT4 pNx Mx L0 V0 G2	cirrhosis
HCC24 (TIL)	female	20-29	pT2 pN0 Mx L0 V1 R0 G2	fibrosis
HCC25 (TIL)	female	70-79	pT3 pN0 Mx L0 V0 R0 G2	none
HCC26 (TIL)	male	70-79	pT2 pN0 Mx L0 V1 R0 G2	cirrhosis

6.1.11 RCC patients

Tissue samples of RCC patients (tumor and corresponding non-tumor samples n=10) were histologically diagnosed as clear cell renal cell carcinoma and were obtained from untreated patients that underwent tumor resections at the Urologische Klinik Dr. Castringius Planegg (Munich, Germany). Patients consented to the donation, samples were anonymized and analysis was approved by the ethics committee by a clearance certificate. Infiltrating leukocytes from renal non-tumor-harboring tissue samples are named as r-NIL and tumor infiltrating leukocytes are named as RCC-TIL when compared with samples of HCC patients.

Table 12: Clinical-pathological characteristics of RCC patients
[1]classification according to guidelines of Union International Contre le Cancer (UICC); T: extent of the primary tumor. N: absence or presence of regional lymph node metastasis. M: absence or presence of distant metastasis. L: lymphatic invasion, V: venous invasion. R: residual tumor after resection. G: histopathological grading. x: not specified

Patient ID and tissue type	Sex	Age (at time of tumor resection)	TNM-Stage[1]
RCC108 (NIL, TIL)	female	81	pT3a L0 V0 R0 G2
RCC115 (NIL, TIL)	male	73	pT1b L0 V0 G2
RCC117 (NIL, TIL)	male	74	pT3a pN0 L0 V0 G3 R0
RCC118 (NIL, TIL)	male	57	pT3b pN0 L0 V1 R1 G3
RCC121 (NIL, TIL)	male	63	pT3a L0 V0 R0 G3
RCC124 (NIL, TIL)	male	72	pTx Lx Vx Rx Gx
RCC128 (NIL, TIL)	male	67	pT3a L0 V0 R0 G2
RCC129 (NIL, TIL)	female	72	pT1a pN0 L0 V0 R0 G1
RCC130 (NIL, TIL)	female	74	pT3a pN0 L0 V0 R0 G3
RCC132 (NIL, TIL)	female	74	pT3a L0 V2 G3
RCC133 (NIL, TIL)	male	68	pT3a pN0 L0 V0 G3

6.2 Methods

6.2.1 Cell culture techniques

To prevent contamination with bacteria, yeast or fungi, all cell culture techniques were performed with sterile materials, solutions and media under sterile conditions inside a laminar flow work bench.

6.2.1.1 Determination of cell counts

Cell counts were determined using a Neubauer counting chamber and trypan blue staining, which stains dead cells. To count live cells, an aliquot of the cell suspension (10 µl) was diluted with trypan blue staining solution (1:10) and transferred into the Neubauer counting chamber. Using light microscopy, living cells were counted within four large squares. The total cell count per milliliter of cell suspension was calculated the following:

$$\text{cells/ml} = \text{mean cell count of four large squares} \times \text{dilution factor} \times 10^4$$

6.2.1.2 Freezing and thawing of cells

For long term storage, 5×10^6 cells were resuspended in cell freezing medium and aliquots of 1 ml per 1.5 ml freezing vial were transferred into a Mr Frosty™ freezing container to prevent fast freezing of the cells. Mr Frosty™ freezing containers were stored at -80 °C until samples were transferred to a liquid nitrogen tank. For thawing, frozen cell suspensions were placed in a water bath (37 °C) until 2/3 of the cell suspension was thawed, then transferred into 2 ml FBS and centrifuged for 5 min at 300 g at room temperature. After removing the supernatant, the cell pellet was resuspended in the thawing medium.

6.2.1.3 Cultivation of adherent cell lines

Mouse myoblastoma cell line P815 was grown in T75 cm^2 with LCL medium until confluent and then passaged 1:10 by detaching cells with 2 x trypsin/EDTA.

6.2.1.4 Generation of activated T cells

Peripheral blood mononuclear cells (PBMC) of healthy donors were seeded at 1 x 10^6 cells in 1 ml per well in anti-CD3 and anti-CD28 antibody coated 24-well plates. After three days, activated T cells were harvested and transduced to stably express the HLA-A2 restricted tyrosinase-specific TCR T58 (66). The activated T cells used in this project underwent a second activation in anti-CD3 and anti-CD28 antibody coated wells with medium containing 100 U/ml IL-2, resulting in a T cell population of mainly cytotoxic ($CD3^+CD8^+$) T cells. Aliquots of 1 ml cell suspension per 1.5 ml freezing tubes were frozen and one aliquot contained 5 x 10^6 cells/ml. Freezing tubes were transferred into a Mr Frosty™ freezing container and stored at -80°C until samples were transferred to a liquid nitrogen tank.

6.2.2 Isolation techniques of leukocytes

Isolation steps were performed fast and under sterile conditions. Sterile plastic pipettes were used to prevent activation of cells.

6.2.2.1 Isolation of PBMC from whole blood samples

Peripheral blood mononuclear cells (PBMC) were isolated from venous whole blood samples of healthy donors. Syringes (50 ml) were prepared with 1000 U heparin per 50 ml blood to prevent blood coagulation. Whole blood samples were diluted directly after blood donation with RPMI 1640 at a ratio of 1:1 and a maximum of 35 ml of the blood/RPMI 1640 solution were pipetted onto 15 ml Ficoll in a 50 ml tube. For separation of the different blood components, the blood samples were centrifuged at 600 g for 20 min at room temperature without brake. The different blood components separate according to their density: erythrocytes and granulocytes sink to the bottom of the tube, PBMC accumulate in the interphase and thrombocytes and diluted plasma constitute the upper phase. The interphase was removed using a 10 ml plastic pipette and transferred to a 50 ml tube. After dilution with RPMI 1640 at a ratio of 1:1, the solution was centrifuged at 597 g for 10 min at room temperature to remove the remaining ficoll. The supernatant was discarded and the cell pellet was resuspended in RPMI III for cell counting. The yield of PBMC was donor dependent and ranged from 20 x 10^7 to 30 x 10^7 cells per 100 ml whole blood. Cell suspensions were frozen as aliquots of 1 ml cell suspension per 1.5 ml freezing tubes whereas one aliquot contained a 5 x 10^6 cells/ml. Freezing tubes were

transferred into a Mr Frosty™ freezing container and stored at -80°C until samples were transferred to a liquid nitrogen tank.

6.2.2.2 Preparation of tissue suspensions

Fresh postoperative tumor and corresponding non-tumor tissue from HCC and RCC patients were evaluated by a pathologist who also selected the sections from each tissue sample for further processing. Tissue samples were collected in RPMI 1640 post-operation and immediately transferred to the lab for processing. The size of the tissue samples ranged from 1 cm x 1 cm x 0.5 cm to 3 cm x 2 cm x 1 cm. In the lab, one small part of each tissue was cut off, wrapped in aluminium foil, shock-frozen in liquid nitrogen and thereafter stored in -80°C until use.

The remaining part of the fresh tissue samples was minced by hand with scalpel and scissors, adding HBSS without Ca^{2+} and Mg^{2+} in small volumes to prevent the tissue pieces from drying out. Tissue suspensions were transferred into a 50 ml tube using a spoon. The volume of tissue suspensions ranged from 2-5 ml. Because only leukocytes that had infiltrated into the tissue were desired for the experiments, the leukocytes in the blood vessels of the tissue were removed by washing the tissue suspension several times with ~ 20 ml of HBSS without Ca^{2+} and Mg^{2+} until the supernatant appeared no longer red. The supernatants of theses washing steps were pooled and named supernatant-1. As these supernatants are thought to contain leukocytes that had not infiltrated into the tissue, they were designated tumor-circulating leukocytes (TCL). The pellet that remained after the washings was incubated for 20 min with 5 mmol/l EDTA in HBSS without Ca^{2+} and Mg^{2+} to detach leukocytes from the tissue cells. After centrifugation at 472 g for 5 min at room temperature, the supernatant was transferred into a fresh 50 ml tube and named supernatant-2. The tissue pellet was resuspended in digestion buffer containing collagenase IA (0.5 mg/ml) and DNase I (0.19 mg/ml) and incubated for 30 min at 37°C. Samples were then centrifuged at 472 g for 5 min at room temperature. The supernatant was pooled with supernatant-2. The remaining pellet was squeezed between two glass petri dishes. While HBSS containing Ca^{2+} and Mg^{2+} was added to prevent the cells from drying out, the cell suspension was forced through a 100 µm filter using the rubber part of a 10 ml syringe. The petri dish was washed with HBSS containing Ca^{2+} and Mg^{2+}, the wash medium was combined with the tissue suspension. Supernatants-1 and -2 and the cell suspension were centrifuged at 472 g for 10 min at room temperature. The supernatants were discarded and the pellet of supernatant-1 containing the TCL was resuspended in RPMI 1640 and counted. Yields were patient-dependent and ranged from

0.3 x 10^6 to 10 x 10^6 cells. Pellets of supernatant 2 and the cell suspension both containing the RCC-TIL and HCC-TIL or corresponding NIL were pooled and counted. Only small non trypan blue stained cells were counted, larger cells were regarded as tumor cells and neglected. The yield of tissue-infiltrated leukocytes was sample-dependent and ranged from 0.5 x 10^6 to 38 x 10^6 cells.

TCL, NIL and TIL were centrifuged at 472 g for 5 min at room temperature, the supernatants were discarded and cell pellets were resuspended in freezing medium. Cell suspensions were frozen as aliquots of 1 ml cell suspension per 1.5 ml freezing tubes whereas one aliquot contained a maximum of 5 x 10^6 cells/ml. Freezing tubes were transferred into a Mr Frosty™ freezing container and stored at -80°C until samples were transferred to a liquid nitrogen tank.

6.2.3 Functional assays

Tissue suspensions of NIL and TIL were analyzed in parallel together with one sample of activated T cells. Previously prepared activated T cells and tissues suspensions of NIL and TIL had been stored in liquid nitrogen. They were thawed and rested for 1 h in thawing and stimulation medium. Cells were counted, diluted to 1 x 10^6 cells/ml and transferred to a non-tissue culture treated 96-well plate (100 µl per well) that had been previously coated with human T cell activators (see p. 37). Degranulation of $CD8^+$ T cells upon stimulation was measured by detection of CD107a; therefore 5 µl of CD107a detecting antibody (see p. 26) was added into each well. After stimulation, cytotoxic T cells release their lytic granules and CD107a, which is a membrane protein of lysosomes and lytic granules of cytotoxic T cells, becomes relocated to the cell surface where it can be detected with specific antibodies. The lytic granules of cytotoxic lymphocytes under normal conditions contain the lytic proteins. The degranulation is the first step of the cytotoxic process leading to the release. For detection of intracellular cytokines like IFN-γ upon stimulation, monensin and brefeldin A were present during stimulation at a dilution of 1:1000 (according to the manufacturer´s protocol) to inhibit intracellular transport processes. This prevents the cytokine release and leads to enrichment of cytokines inside the cells. After cell permeabilisation, the retained cytokines can be detected with fluorochrome-labeled antibodies. The staining-combination used to address $CD8^+$ T cell stimulation as well as the used buffers are in detail described on p. 42.

6.2.3.1 Stimulation of TIL with ImmunoCult™ human T cell activators

To mimic target cell stimulation of the TCRs, activated T cells and tissues suspensions were stimulated with ImmunoCult™ (StemCell™ Technologies) anti-CD3 human T cell activators that consist of anti-CD3 monospecific tetrameric antibody complexes. To address the additional contribution of co-stimulation through CD28, human T cell activator anti-CD3 plus anti-CD28 (CD28 monospecific tetrameric antibody complexes) was used. A flat bottom not-tissue-culture-treated 96-well plate was coated with 50 µl per well of a solution of human T cell activators and PBS at ratio of 1:100. The plate was stored at 4°C for 3 days. At the day of stimulation, the solution of the human T cell activators was aspirated, wells were washed with PBS (100 µl per well) and unspecific binding was prevented by blocking with 2% BSA in PBS (100 µl per well) for 30 min. After blocking, the solution was aspirated and wells were washed with PBS (50 µl per well), PBS was aspirated and 2 x 10^5 cells per well of activated T cells or tissue suspension were added. Fluorochrome-labeled CD107a-antibody (5 µl per well), monensin and brefeldin A (1:1000; according to the manufacturer´s protocol) to address degranulation and cytokine induction were added to the wells.

6.2.3.2 Rationale of stimulation with ImmunoCult™ human T cell activators

Naturally T cell responses are triggered by peptide MHC complexes (pMHC). However, the characteristics of the human material, with undetermined MHC types and unknown antigenic repertoire, does not allow specific stimulation with natural pMHCs: Primary tumor cells of the patient´s tumor tissues might seem to be a good alternative to pMHC stimulation. However, tumor cells might not be able to provide the pMHC stimulation as they might have lost antigen presentation or lost MHC or might express inhibitory ligands. Thus, if the T cell does not response to primary tumor cell stimulation, the underlying cause is difficult to interpret since it might be the tumor cell not providing the stimulus, or the T cells not being able to respond. Anti-CD3 stimulation allows to address the question whether a T cell can activate the TCR signaling cascade leading to functional response. Therefore, it can be concluded that a T cell that does not respond to anti-CD3 stimulation might have intrinsic defects in its response capacity. On the contrary, a T cell responding to anti-CD3 stimulation might be non-responsive in the tumor microenvironment due to the tumor immune escape mechanisms as the presence of inhibitory immune cells or soluble metabolites (50).

An established method to provide target cell stimulation to T cell populations uses the P815 mouse mastocytoma cell line loaded with anti-CD3 antibody (and when appropriate anti-CD28). Although the antibodies bind to the Fc receptors on the cell surface, the loading with anti-CD3 antibody cannot be fully controlled and variations in the amount of anti-CD3 (and when appropriate anti-CD28) can result in variable T cell responses. Human T cell activators are commercial available and consist of anti-human CD3 monospecific tetrameric antibodies at a defined concentration. They are a stable and reproducible system for delivering the same signal to all T cell samples stimulation allowing comparison across T cell samples from different origin.

Human T cell activators are usually used for long-term T cell expansion rather than for short stimulation of T cells to measure effector activity. The optimal concentration of T cell activators for short term stimulation to induce effector function had to be determined. This was done by comparing the stimulation to anti-CD3 loaded P815. Briefly, P815 cells were detached with accutase, centrifuged at 472 g for 5 min at room temperature, resuspended in Opti-MEM and counted. 1 x 10^6 cells were loaded with 5 µg of OKT3 together with 5 µg of isotype antibody or anti-CD28 antibody. The cell suspension was incubated on a shaker for 30 min at room temperature, washed with Opti-MEM and resuspended in stimulation medium. P815 cells and activated T cells were counted, diluted to 0.1 x 10^6 cells/50 µl, and mixed at a ratio of 1:1 resulting in a total volume of 100 µl medium. Anti-CD107a antibody (5 µl), monensin and brefeldin A (1:1000; according to the manufacturer´s protocol) were added and samples were incubated for 5 hours at 37 °C. In parallel, 0.1 x 10^6 activated T cells in 100 µl of stimulation medium were added into 96-wells coated with 1:20, 1:100, 1:200 dilutions of anti-CD3 human T cell activator (described above, p. 37). Also here, 5 µl of anti-CD107a antibody, monensin and brefeldin A (1:1000, according to the manufacturer´s protocol) were added and samples were incubated for 5 h at 37°C. Then, cells of the stimulation with P815 or with human T cell activator were harvested and stained for FACS-analysis with the surface markers anti-CD45 (Pe-Cy7), anti-CD3 (Alexa Fluor® A700) and anti-CD8 (V500), followed by fixation and permeablilation with BD Cytofix/Cytoperm Fixation/Permeabilisation Kit and staining of IFN-γ (PerCp-Cy5.5).

As seen in figure 2, CD3-loaded P815 stimulation resulted in 10% single positive T cells for IFN-γ, 4% for CD107a and 2.5% T cells double positive for both markers. These results are similar to the frequencies achieved with a dilution of 1:100 of human T cell activator. Adding CD28 to the CD3 stimulation had no effect in the P815 system with regards to T cells being single positive of CD107a (10%) or single positive of IFN-γ (4.5%). T cells being double positive (8.8%) for both markers had increased compared

with anti-CD3 loaded P815 cells. Similar results were obtained with human T cell activator at a dilution of 1:100, and IFN-γ single positive T cells were even higher (31%). In summary, human T cell activator at a dilution of 1:100 can be used for stimulation of effector function in T cells and yields comparable results to the previously used CD3-loaded P815 cell system.

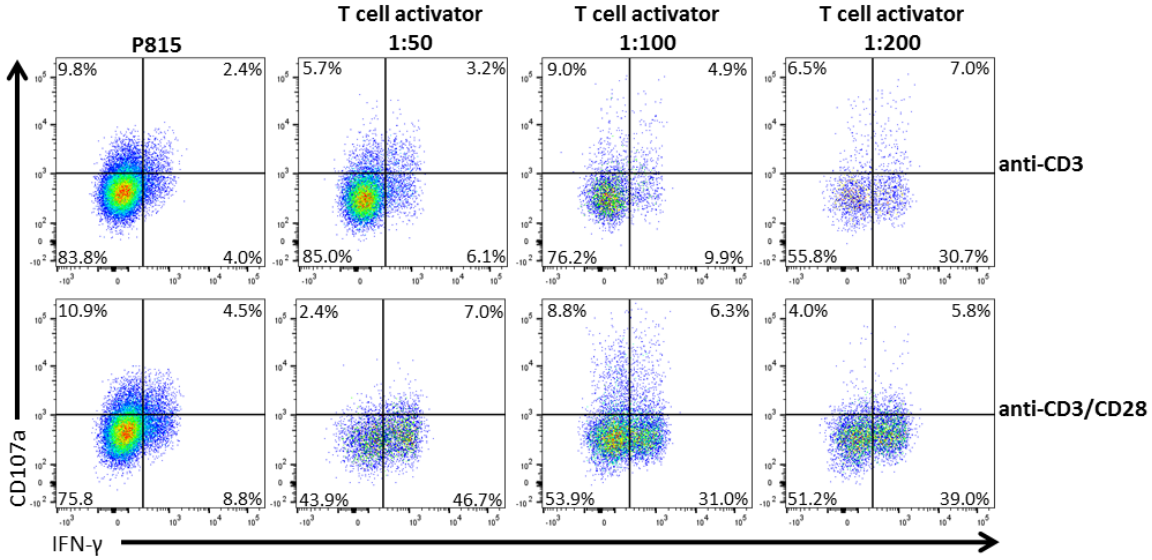

Figure 2: T cell stimulation with anti-CD3 or anti-CD3/CD28-loaded P815 cells, compared with anti-CD3 or anti-CD3/CD28 T cell activators
Activated T cells were stimulated either with anti-CD3/isotye and anti-CD3/CD28 loaded P815 cells or with anti-CD3 and anti-CD3/CD28 T cell activator coated, on a 96-well plate at a dilution of 1:50, 1:100 or 1:200. Degranualation (CD107a) and IFN-γ production were measured by flow cytometry.

6.2.3.3 Negative controls

One aliquot of activated T cells or TIL was used as negative control. Here, monensin, brefeldin A and anti-CD107a antibodies were added to 5 x 10^5 cells at the beginning of the stimulation, but these cells were not treated with a stimulus. After 5 hours at 37 °C, negative controls and stimulated samples were prepared for flow cytometry in parallel.

6.2.3.4 Stimulation with PMA/Ionomycin

Activated T cells or TIL were thawed, resuspended in thawing and stimulation medium, counted and diluted to 2 x 10^5 cells in 200 µl of stimulation medium. 50 ng/ml of phorbol-12-myristate-13-acetate (PMA), 500 ng/ml Ionomycin as well as anti-CD107a antibody (5 µl) and monensin and brefeldin A (1:1000, according to the manufactor´s protocol) were added. Samples were incubated for 5 h at 37 °C. Thereafter, cells were harvested and stained with antibodies for surface markers followed by cell permeabilisation as indicated (see p.42).

6.2.4 Multiparameter flow cytometry

Flow cytometry allows the analysis of marker expression on a single cell level using fluorochrome labelled antibodies that bind to surface or to intracellular markers of the cell. The cell suspension is forced through a thin capillary which results in a monodisperse stream of cells that passes a laser beam. Photomultipliers (PMT) detect the light scatter. The forward scatter (FSC) is proportional to the size of the cells whereas the sideward scatter (SSC) correlates to the granularity of the cells. When passing the laser beam, the fluorochromes of the antibodies absorb light of a certain wavelength. To allow the use of a variety of fluorochromes with different absorption spectra, several lasers with different wavelengths are combined. The absorbed light results in a higher energy level of the electrons and during the relaxation of the electron back to the ground state, a photon with a higher wavelength than the absorbed light is emitted. This results in a characteristic emission spectrum for each fluorochrome. The emitted light is detected by PMTs which intensify the signals of the photons and convert them into electricity. With the help of different filters, one specific channel for the emission of one specific fluorochrome is shielded from the emission of other fluorochromes to minimize the interference of different emission wavelengths. Because the emission spectra of different fluorochromes overlap and interference cannot completely be prevented by the optical filters, an electronic subtraction (compensation) is necessary to eliminate remaining interferences. With the help of programs for the analysis of flow cytometry data (e.g. FlowJo®, TreeStar), the compensation can be performed. Furthermore, the frequency of cells with the same marker on the cell surface can be determined. It is also possible to address the expression level of surface or intracellular molecules by determining the fluorescence intensity per cell.

There are different possibilities to display flow cytometry data: a histogram shows the distribution of cells which are characterized by a single parameter and the fluorescence intensity can be determined. Two parameters can be displayed as a dot-plot where each single cell is displayed by a dot with an x-coordinate representing one fluorescence and a y-coordinate representing the second fluorescence.

Data for the experiments in this thesis were acquired by a LSR II cytometer (BD) consisting of four lasers which allows to measure up to 18 different fluorochromes. The used lasers, filters and fluorochromes were combined as following (table 13):

Table 13: Characteristics of used fluorochromes, lasers and filters for detection at the LSR II

Fluoro-chrome	Excitation maximum (nm)	Emission maximum (nm)	Laser	Laser wavelength (nm)	Detection filter (nm)
Alex Fluor® 488	495	520	Coherent Sapphire blue	488	530/30
Alexa Fluor® 647	650	668	HeNe (red)	633	670/20
Alexa Fluor® A700	696	719	HeNe (red)	633	730/45
APC	650	660	HeNe (red)	633	660/20
Alexa Fluor® A488	650	660	HeNe (red)	633	660/20
APC-eFluor 780	650	785	HeNe (red)	633	780/60
BV421	407	421	Coherent VioFlame PLUS violet	405	450/50
FITC	494	520	blue Coherent Sapphire blue	488	530/30
Indo-1 violet	358	461	Lightwave Xcyte (UV laser)	355	250/50
PB	401	452	Coherent VioFlame PLUS violet	405	450/50
PE-TexasRed®	496	613	blue Coherent Sapphire blue	488	610/20
PE	496	578	blue Coherent Sapphire blue	488	575/26
PE-Cy7	496	785	blue Coherent Sapphire blue	488	780/60
PerCp-Cy™5.5	482	690	blue Coherent Sapphire blue	488	695/40

Fluoro-chrome	Excitation maximum (nm)	Emission maximum (nm)	Laser	Laser wavelength (nm)	Detection filter (nm)
V450	404	450	Coherent VioFlame PLUS violet	405	450/50
V500	415	500	violet Coherent VioFlame PLUS violet	405	525/50

6.2.4.1 Staining combinations

Antibody combinations were selected to allow the analysis of the composition of infiltrating leukocytes, T-cell subsets, phenotype and function in tumor and corresponding non-tumor tissue of HCC and RCC patients and healthy donors.

Table 14: Antibody combinations

Number	Aim of the combination	Surface markers	Markers stained intracellularly
1	leukocyte infiltrate activation and exhaustion	LIVE/DEAD™ Fixable Blue Dead Cell Stain (indo-1 violet) CD45 Pe-Cy7 CD3 PerCp-Cy™5.5 CD8 V500 CD4 APC-eFluor 780 CD19 Alexa Fluor® A700 CD20 Alexa Fluor® A700 CD14 PB CD56 V450 PD-1 PE	Ki-67 Alexa Fluor® A488 LAG-3 ATTO 647N
2	AKT-pathway cell cycle	LIVE/DEAD™ Fixable Blue Dead Cell Stain (indo-1 violet) CD45 Pe-Cy7 CD3 PerCp-Cy™5.5	pAKT(S473) V450 p27kip PE Cyclin E FITC
3	mTOR-pathway cytotoxic proteins	LIVE/DEAD™ Fixable Blue Dead Cell Stain (indo-1 violet) CD45 Pe-Cy7 CD3 PerCp-Cy™5.5	pmTOR(S2448) APC prps6(S244) PE perforin FITC
4	anergy exhaustion	LIVE/DEAD™ Fixable Blue Dead Cell Stain (indo-1 violet) CD45 Pe-Cy7 CD3 PerCp-Cy™5.5 CD8 V500 CD4 APC-eFluor 780 CD19 Alexa Fluor® A700 CD20 Alexa Fluor® A700 CD56 V450	PD-1 PE DGK-α (unmarked, secondary antibody: Alexa Fluor® 647) Foxo1 (unmarked, secondary antibody: Alexa Fluor® 488)

Number	Aim of the combination	Surface markers	Markers stained intracellularly
5	exhaustion, differentiation, cytotoxicity	LIVE/DEAD™ Fixable Blue Dead Cell Stain (indo-1 violet) CD45 Pe-Cy7 CD3 Alexa Fluor® A700 CD8 V500 CD4 APC-eFluor 780 CD56 V450 PD-1 PerCp-Cy™5.5	Tbet eFluor™660 Eomes PE perforin FITC granzyme B PE-TexasRed®
6	stimulation	LIVE/DEAD™ Fixable Blue Dead Cell Stain (indo-1 violet) CD107 APC CD45 Pe-Cy7 CD8 V500 CD4 APC-eFluor 780 CD19 BV421 CD20 BV421 CD56 BV421 PD-1 PE	CD3 Alexa Fluor® A700 IFNγ PerCp™-Cy5.5 Ki-67 PE-TexasRed® CD28 FITC

6.2.4.2 Sample Preparation for flow cytometry

T cells and tissue suspensions had been stored in liquid nitrogen and were thawed and rested for 1 hour before being prepared for flow cytometry analysis or stimulation. It was the intension to determine the features of the immune cells that they had acquired *in situ* in the tissue context. Culture *in vitro*, exposure to medium and supplements (cytokines, FBS, etc.) were kept to a minimum, as they are known to alter the immune cells. Tissue suspensions of tumor and non-tumor tissues of 2-5 patients were analyzed in parallel always together with one healthy control PBMC to allow normalization of stainings performed on different days. Master mixes of antibody combinations were prepared to reduce variability.

Cell suspensions of 1 x 10^5 to 5 x 10^5 cells per antibody combination were used and incubation steps were performed in the dark at 4 °C. For washing the cells, the indicated buffers were added, cell suspensions were centrifuged and the supernatant was removed to a volume of 50 µl. If not indicated differently, centrifugation steps were performed at 472 g for 5 min at room temperature.

Samples used for staining combination 1 were washed with 500 µl PBS/EDTA (2 mM), staining reagents for viability (LIVE/DEAD™ Fixable Blue Dead Cell Stain) and antibodies for surface staining were added and cells were incubated for 20 min. Unbound antibodies and LIVE/DEAD™ Fixable Blue Dead Cell Stain were removed by washing with 500 µl of FACS buffer. For detecting intracellular markers, the cells need to be fixed and permeabilized. Therefore, the cell pellet was resuspended in 500 µl 1% PFA in PBS and

incubated for 15 min. After centrifugation of the cell suspensions, the supernatant was removed and cells were permeabilized for intracellular staining by resuspending the pellet in 500 µl of 0.1% saponin. Cell suspensions were immediately centrifuged, supernatants were discarded and the pellet was resuspended in 0.35% saponin. After centrifugation and removal of the supernatant, antibodies for intracellular staining were added and incubated for 20 min. Unbound antibodies were removed by washing the cells with 500 µl of 0.1% saponin and a second time with 500 µl of 0.35% saponin. Shortly before data acquisition, Flow-count Fluorospheres (Beckmann coulter) were added to allow determining the absolute cell numbers of populations within the leukocyte infiltrate.

Staining combinations 2 and 3 were designed to detect phosphorylated proteins using a commercial buffer set (BD Phosflow™). Cells were washed with 500 µl PBS/EDTA (2 mM), staining reagent for viability (LIVE/DEAD™ Fixable Blue Dead Cell Stain) was added and cell suspensions were incubated for 10 min in the dark at room temperature. Unbound staining reagent was removed by washing the cells with 500 µl of FACS-buffer. For fixation, 200 µl of Cytofix™ Fixation Buffer (BD) were added and cells were incubated for 15 min at 37°C. The supernatant was removed after centrifugation (380 g, 8 min, RT) and cells were permeabilized with 500 µl of BD Phosflow™ Perm Buffer III (stored at -20°C and used directly without warming) for 30 min. Cells were centrifuged (380 g, 8 min, room temperature), supernatants were discarded and antibodies for surface molecules and for phosphorylated intracellular signaling proteins were added. After incubation for 30 min, cells were washed with 500 µl of FACS-buffer, centrifuged (380 g, 8 min, room temperature) and the supernatant was discarded. Secondary antibody was added and cells were incubated for 30 min. Cells were analyzed after washing with 500 µl of FACS-buffer, centrifugation (380 g, 8 min, room temperature) and removal of the supernatant.

Staining combinations 4 and 5 were established to detect cell differentiation states based on transcription factor expression. To make transcription factors accessible for labelling with antibodies, the Transcription Factor Buffer Set (BD) was applied. Cell suspensions were washed with 500 µl PBS/EDTA (2 mM), staining reagents for viability (LIVE/DEAD™ Fixable Blue Dead Cell Stain), antibodies for surface staining were added and cells were incubated for 20 min. Unbound antibodies were removed by washing with 500 µl of FACS buffer. The Transcription Factor Buffer Set (BD) was used for fixation and permeabilisation. The pellet was resuspended in 1 ml of Fix/Perm working solution (dilution of 1:4 of the Fix/Perm Buffer and diluent buffer) and after incubation for 45 min, 1 ml of Perm/Wash working solution (pre-diluted 1:5 with deionized water) was directly added. Cell suspensions were centrifuged and supernatants were removed. Cells were

washed twice with 1 ml of Perm/Wash working solution, antibodies for intracellular antigens were added and cells were incubated for 40 min. After washing cells twice with Perm/Wash working solution (2 ml), samples stained for combination 5 were analyzed. Regarding staining combination 4, secondary antibody was added to cell suspensions. After incubation (30 min), cells were washed twice with 2 ml of Perm/Wash working solution and were analyzed.

Samples used for staining combination 6 had been incubated at 37 °C in medium and stimulated to induce effector function. Cell suspensions were washed with 500 µl PBS/EDTA (2 mM), staining reagent for viability (LIVE/DEAD™ Fixable Blue Dead Cell Stain) was added and cell suspensions were incubated for 10 min in the dark at room temperature. Unbound staining reagent was removed by washing the cells with 500 µl of FACS-buffer and all of the supernatant was removed. To prevent interactions between the three antibodies labelled with BD Horizon Brilliant™ polymer dye BV421 (anti-CD19, anti-CD20 and anti-CD56), all surface antibodies were diluted into BD Horizon™ Brilliant Stain Buffer (50 µl per sample) and this mixture was then used to resuspend the pellet. Cells were incubated for 20 min and unbound antibodies were removed by washing with 500 µl of FACS buffer. Cells were resuspended in 250 µl of Fixation and Permeabilisation Solution (BD Cytofix/Cytoperm™ Fixation/Permeabilisation Kit). After incubation for 20 min, 500 µl of BD Perm/Wash™ buffer (pre-diluted 1:10 with deionized water) were added, samples were centrifuged and the supernatant was removed. The pellets were washed with 500 µl of BD Perm/Wash™ buffer (pre-diluted 1:10 with deionized water), supernatants were removed and intracellular antibodies were added. After incubation of 30 min, cells were washed twice with 500 µl of BD Perm/Wash™ buffer (pre-diluted 1:10 with deionized water) and analyzed.

6.2.4.3 Compensation beads and compensation matrix

To correct the interference of different fluorochrome emissions, a compensation matrix based on measurements of compensation beads is necessary. The compensation beads are a 1:1 mixture of two types of beads, one that is coated by antibodies that bind the κ-light chain of the fluorochrome labelled antibodies (positive bead) and the other type that does not bind the antibodies (negative bead). 1 µl of the fluorochrome labelled antibody of interest was added to the compensation beads, incubated for 20 min and unbound antibody was removed by washing with FACS-buffer. The negative and positive compensation beads now allow the measurement of two distinct populations that are either negative or positive for the fluorescence of interest. These values can then be used

to create the compensation matrix. For each fluorochrome that is used in a staining combination, compensation beads need to be prepared.

The compensation control of the LIVE/DEAD™ Fixable Blue Dead Cell Stain (Thermo Fisher Scientific) to detect dead cells was prepared using ArC™ amine reactive compensation Kit (Thermo Fisher Scientific). One drop of component A (ArC™ beads that bind LIVE/DEAD™ Fixable Blue Dead Cell Stain) were incubated with 1 µl of LIVE/DEAD™ Fixable Blue Dead Cell Stain for 20 min. Unbound LIVE/DEAD™ Fixable Blue Dead Cell Stain was removed by washing with PBS/EDTA (2 mM). Thereafter, one drop of ArC™ negative beads was added and the solution allowed the measurement of two distinct populations positive and negative for the fluorescence of the LIVE/DEAD™ Fixable Blue Dead Cell Stain.

6.2.4.4 Flow-Count Fluorospheres

Flow cytometry allows qualitative analysis of cells and thereby the leukocyte composition can be determined as frequencies of cell types within specified populations. Quantitative enumeration of actual cell numbers of a specific subset within the leukocyte infiltrate requires the in-sample presence of a reference that has a defined number. Flow-Count Fluorospheres (Beckmann Coulter) can be added to the cell suspension ready for FACS acquisition providing a reference number of events. This was done with staining combination 1, where the composition of the infiltrate was determined. Flow-Count Fluorospheres consist of 10 µm polystyrene fluorospheres with a fluorescence emission range of 525 nm – 700 nm when excited at 488 nm. After the staining procedure was completed, the remaining volume in the staining tube was measured and the same volume of counting beads was added to get a dilution of 1:1 (according to the manufacturer's recommendation). During data acquisition, the stopping gate was defined by the registered events of the counting beads and 3 x 10^4 events were recorded (acquisition of a minimum of 1 x 10^4 counting beads was required to allow statistical calculation). The analyzing software FlowJo® (TreeStar) was used to determine the recorded events of the counting beads and the leukocyte populations of interest. The absolute cell count/µl was calculated the following:

$$\text{absolute cell count/µl} = \frac{\text{concentration of beads/µl x cell count [population of interest]}}{\text{Flow-Count Fluorosphere events count x dilution factor}}$$

The calculated absolute cell counts per µl refer to the amount of cells in the tube that was used for data acquisition. Cell counts independent from the volume in the tube were calculated by multiplying the cell counts/µl by the volume of the cell suspension in the tube, resulting in the number of cells that were present in the tube. To compare cell counts of infiltrating leukocytes across different tumors, cell count per ml tissue was calculated the following:

Because one vial of frozen TIL was thawed and used for all staining combinations 1-5 and Flow-Count Fluorospheres were only used in staining combination 1, cell counts within the tube used for acquisition of Flow-Count Fluorospheres had to be multiplied by the number of staining combinations. This resulted in the number of leukocytes that were present in the freezing vial. Because isolated TIL were frozen in different numbers of aliquots depending on the total number of isolated TIL, the number of cell counts in one freezing vial was multiplied by the number of freezing vials to achieve the total number of infiltrated leukocytes in the tissue sample. To compare cell counts across different tissue suspensions, which were prepared from differently sized tissues, the volume of the original tissue was considered und the cell numbers were normalized to 1 ml of tissue volume.

The resulting formula is the following:

$$\text{absolute cell count/ml tissue} = \frac{\text{absolute cell count/µl x tube volume x 5 x number of freezing vials}}{\text{solid volume of the tissue after mechanical dissociation [ml]}}$$

The formula contains the following determinants: absolute cells counts/µl as determined with the help of the flow count beads; µl of volume in the staining tube; factor 5, since one vial of tissue suspension was divided over 5 staining combinations where only one was used for cell counting, number of freezing vials of the original tissue suspension, solid volume of the tissue after mechanical dissociation.

6.2.4.5 Data acquisition

Flow cytometry data were acquired by LSR II (BD) using FACSDIVA™ (BD) software. Compensation beads for each fluorochrome were acquired and the compensation matrix was calculated by FACSDIVA™ (BD) software. If necessary, the compensation matrix was slightly adjusted manually using the analyzing software FlowJo® (TreeStar). For data acquisition at the LSR II (BD), PMT values for FSC and SSC were selected to position the cell population in the middle of the FSC/SSC-dot plot. The PMT settings of the different

channels for each fluorochrome were modified to achieve a high resolution by positioning the negative peak close to zero and the positive peak to the right of the x axis. Between 1 x 10^4 and 50 x 10^4 were recorded within the alive/$CD45^+$ cell population.

6.2.5 Statistical analysis

Statistical analysis was performed with GraphPad Prism (7^{th} edition, GraphPad Software, San Diego, California, USA). For all statistical tests, the level of 95% was selected. N.s. means not significant and significance between samples was indicated by *($p<0.05$), **($p<0.01$), ***($p<0.001$) or ****($p<0.0001$).

6.2.5.1 Mann-Whitney U test

The Mann-Whitney U test was used as a non-parametric test to determine if mean values of two unpaired data sets were significantly different.

6.2.5.2 Wilcoxon matched pairs signed-rank test

Wilcoxon matched pairs signed-rank test is a non-parametric statistical test to compare the mean of two related groups of samples. This test was applied for samples depending from each other.

6.2.5.3 Kruskal-Wallis test, Friedmann test and Dunn´s Post-hoc comparisons

To compare three or more groups, the non-parametric Kruskal-Wallis test was used to determine significance of unpaired or unmatched groups and the non-parametric Friedmann test was applied when significance of paired or matched groups were analyzed. Because both tests can only state whether or not more than two groups of samples are significant different, Dunn´s Post-hoc comparisons were applied to evaluate which means of which groups are significantly different.

6.2.5.4 Spearman´s rank correlation

Spearman´s rank correlation was applied to test correlation between two variables (x and y) of non-parametric distributions. The correlation coefficient r^2 describes the correlation and ranges from zero to one, e.g. $r^2=1$ (perfect correlation) or $r^2=0.6$ (60% of

the variance in x can be explained by variation in y). To test if the detected correlation was caused by random sampling, the P value was calculated. A small P value allows rejecting the hypothesis that the correlation is due to random sampling.

7 Results

7.1 Characterization of the organ-resident immune cell infiltrate comparing non-tumor with tumor tissue of kidney and liver

Immune contexture was defined by density, subtypes and differentiation state of tumor infiltrating leukocytes (TIL) (48). Their interplay determines the anti-tumor immune response to a large extent and immune contexture of TIL was found to relate not only to prognosis but also to prediction of treatment and response to immunotherapy (48). Multi-parameter flow cytometry was used to determine the composition of the immune cell infiltrate of RCC-TIL and HCC-TIL, discriminating leukocyte subgroups of monocytes/macrophages, B cells, NK cells and T cells, with further distinction of the CD4 and CD8 T cell subsets.

7.1.1 Experimental setup

Tissue suspensions of tumor and corresponding non-tumor tissue of kidney (RCC-TIL, r-NIL, see p. 32) and liver (HCC-TIL, h-NIL, see p. 30) were analyzed by multi-parameter flow cytometry (table 15). Furthermore, peripheral blood mononuclear cells (PBMC) of healthy donors (HD-PBMC) served as a control for the staining procedure and were also compared to TIL and NIL.

Table 15: Antibody staining combination to address leukocyte infiltrates in NIL and TIL (staining combination 1). The markers PD-1, LAG-3 and Ki-67 are further addressed later (see p.102).

Target/ Epitope	Fluorochrome	Cell subset/ function
Viability: LIVE/DEAD™ Fixable Blue Dead Cell Stain	Indo-1-violet	staining of dead cells
CD45	Pe-Cy7	leukocytes
CD3	PerCp-Cy™5.5	T cells
CD8	V500	$CD8^+$ T cells
CD4	APC-eFluor 780	$CD4^+$ T cells
CD19/CD20	Alexa Fluor® A700	B cells
CD56	V450	NK cells
CD14	PB	monocytes
PD-1	PE	activation/exhaustion marker
Ki-67	Alexa Fluor® A488	proliferation marker
LAG-3	ATTO 647N	activation/exhaustion marker

7.1.1.1 Gating strategy

The gating strategy to identify leukocyte subgroups within the cell suspensions of tumor and non-tumor tissues is exemplified in figure 3 (see p. 53). First, $CD45^+$ leukocytes were separated from $CD45^-$ tumor cells by plotting size granularity (SSC-A; y axis) against CD45 (x axis). Within $CD45^+$ cells, live cells were gated as cells negative for marker of dead cells (LIVE/DEAD™ Fixable Blue Dead Cell Stain). Next, doublets or cell aggregates were excluded by gating on single cells, plotting forward scatter height (FSC-H, y axis) against forward scatter area (FSC-A, x axis). The resulting population of leukocytes/alive/singlets was separated into monocytes/macrophages and lymphocytes based on FSC/SSC characteristics. The population with higher FSC/SSC features, designated as myeloid population, was further described by the monocytes/macrophage marker CD14, which revealed a $CD14^+$ population and a $CD14^-$ population. A minor fraction of the $CD14^-$ population was B cells and T cells, as detected by plotting CD14 against CD19/CD20 or CD3. The $CD14^-$ population was therefore regarded as neutrophils, because they were positive for CD45 but no other marker defining the leukocyte population. However, the $CD14^-$ population has a large granularity (as they are part of the myeloid gate defined by large granularity) making it unlikely that this population corresponds to NK cells. Lymphocytes were further analyzed within the small FSC/SSC

gate. B cells were detected by positivity for CD19/CD20 and the remaining lymphocytes, which include T cells and NK cells, were evaluated in the NOT-CD19 gate. T cells were described as $CD3^{+}CD56^{\pm}CD19^{-}CD20^{-}CD14^{-}$, NK cells as $CD3^{-}CD56^{+}CD19^{-}CD20^{-}CD14^{-}$ and B cells as $CD3^{-}CD56^{-}CD19^{+}CD20^{+}CD14^{-}$. Frequencies of each leukocyte population were then calculated as percentages of $CD45^{+}$/alive/singlets cells. T cell subsets ($CD8^{+}CD4^{-}$ and $CD8^{-}CD4^{+}$ cells) were defined within preselected $CD3^{+}$ gate by plotting CD8 on the y axis and CD4 on the x axis.

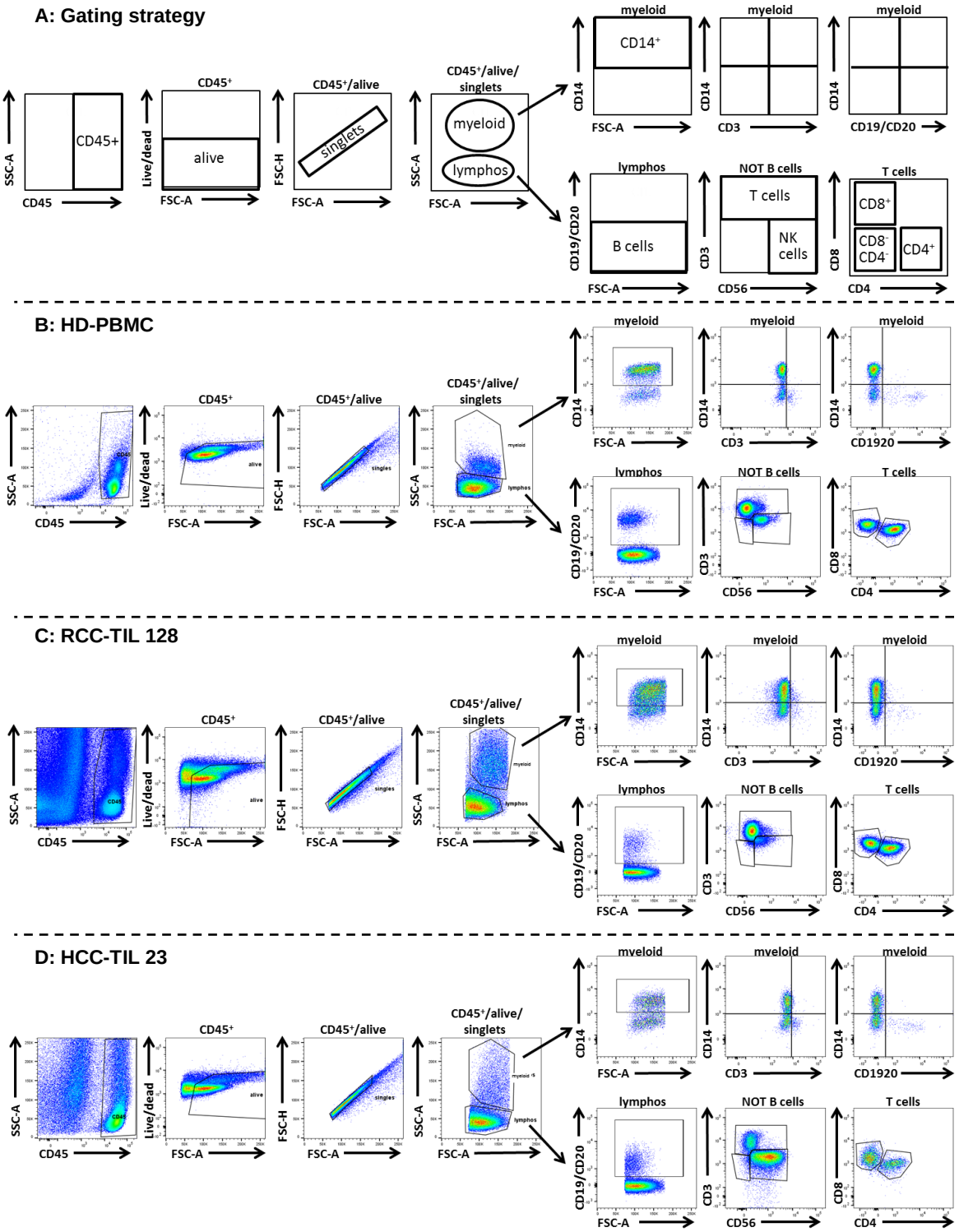

Figure 3: Gating strategy to determine leukocyte subgroups in PBMC, RCC and HCC tumor cell suspensions (TIL) and corresponding non-tumor suspensions (NIL)

Cell suspensions were stained (table 15, see p. 51) and analyzed by flow cytometry. Monocytes ($CD3^-CD56^-CD19^-CD20^-CD14^+$), B cells ($CD3^-CD56^-CD19^+CD20^+CD14^-$), T cells ($CD3^+CD56^{+/-}CD56^-CD19^-CD20^-CD14^-$), NK cells ($CD3^-CD56^+CD19^-CD20^-CD14^-$) and T cell subgroups ($CD8^+CD4^-$ and $CD8^-CD4^+$) were identified in healthy donor PBMC, NIL and TIL of RCC and HCC patients. A: schematic depiction of the gating strategy. B: healthy donor PBMC. C: RCC-TIL. D: HCC TIL.

7.1.2 Composition of the organ-resident immune cell infiltrates

The composition of immune cells is summarized in figure 4 A by stacked bar diagrams for HD-PBMC, r-NIL, RCC-TIL, h-NIL and HCC-TIL. Each leukocyte population is represented by a different color, the height of the bar represents the mean of the population within one organ type. T cells dominated the immune cell infiltrate in organs with lowest frequencies observed in tissue suspension of non-tumor kidney (r-NIL) and liver (h-NIL). Renal-NIL showed the highest percentages of monocytes/macrophages among the analyzed organs whereas h-NIL were marked by the highest frequencies of NK cells. This is consistent with previous findings that had reported a network of dendritic cells in the kidney (67) and also high percentages of NK cells in the liver (68).

A

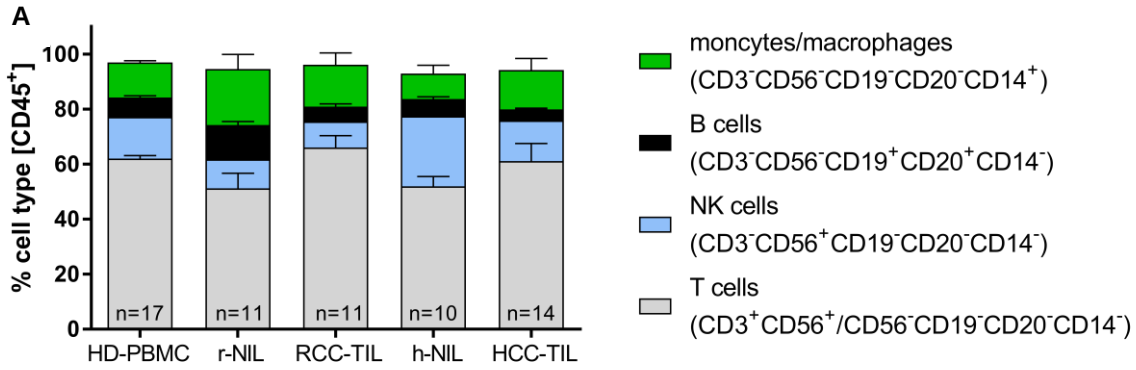

B

sample type	T cells (mean, range, %)	NK cells (mean, range, %)	B cells (mean, range, %)	monocytes/ macrophages (mean, range, %)
HD-PBMC (n=17)	60.9 (49.8 – 70.7)	15.8 (10.4 – 21.0)	7.8 (3.9 – 13.2)	11.5 (7.9 – 15.7)
r-NIL (n=11)	51.0 (12.3 – 77.3)	10.5 (3.4 – 23.2)	10.3 (7.0 – 18.3)	21.0 (4.8 – 57.4)
RCC-TIL (n=11)	66.7 (33.2 – 87.1)	8.7 (2.8 – 15.0)	5.4 (0.8 – 13.2)	13.2 (2.4 – 51.6)
h-NIL (n=10)	52.1 (36.7 – 67.4)	28.1 (16.1 – 40.8)	7.3 (2.3 – 10.1)	9.0 (0.7 – 33.3)
HCC-TIL (n=14)	61.1 (13.8 – 93.0)	14.6 (2.2 – 60.6)	4.2 (0.9 – 7.0)	14.1 (0.6 – 46.8)

C

statistical significance			
T cells	none		
NK cells	h-NIL/r-NIL: **	RCC-TIL/h-NIL: ***	h-NIL/HCC-TIL:**
B cells	HD-PBMC/HCC-TIL: *	r-NIL/RCC-TIL: **	r-NIL/HCC-TIL: ****
monocytes/macrophages	none		

Figure 4: Organ-resident immune cell infiltrates in tumor and non-tumor tissues of kidney and liver
Tissue suspensions and HD-PBMC were stained for flow cytometry (table 15, see p. 51) and leukocyte population frequencies were determined within the gated $CD45^+$/live/singlet cells (leukocytes). A: Leukocyte subsets of HD-PBMC, r-NIL, RCC-TIL, h-NIL and HCC-TIL are summarized in stacked bars, each leukocytes subset is represented by a different color. The height of the bars represents means and deviation is marked by standard error of the mean (SEM). B: Means and ranges of leukocyte populations of different samples. C: Summary of statistical significance addressed by Kruskal-Wallis test and Dunn´s Post-hoc comparisons (*p<0.05; **p<0.01; ***p<0.001; ****p<0.0001).

7.1.3 Patient-specific deviations of immune cell infiltrates

The tissue-specific comparison of the immune cell infiltrate revealed similar frequencies of leukocyte subsets in HD-PBMC, RCC-TIL and HCC-TIL. The percentages of T cells of r-NIL and h-NIL were similar, but r-NIL and h-NIL were different in frequencies of NK cells, B cells and monocytes/macrophages. Next, deviations in the immune cell infiltrates of non-tumor and tumor tissues were analyzed in more detail.

In RCC-TIL and HCC-TIL, frequencies of T cells were increased compared with r-NIL or h-NIL, respectively. The difference was statistically significant between r-NIL and RCC-TIL, and two patients were identified in r-NIL and h-NIL that had elevated percentages of T cells compared with corresponding RCC-TIL or HCC-TIL (figure 5 A). Frequencies of NK cells were in general decreased in RCC-TIL and HCC-TIL compared with r-NIL or h-NIL, the difference was significant between h-NIL and HCC-TIL. With regard to kidney resident NK cells, two groups of patients were identified. Five patients had increased percentages of NK cells in r-NIL whereas five patients were marked by decreased frequencies in r-NIL compared with RCC-TIL (figure 5 B). In RCC-TIL and HCC-TIL, percentages of B cells were significantly decreased compared to frequencies in r-NIL or h-NIL. Two patients of RCC and HCC were identified by increased percentages of B cells in NIL compared with TIL (figure 5 C). Frequencies of monocytes and macrophages ($CD14^+$) were comparable in NIL and TIL of RCC and HCC patients, however, two groups of patients were detected. Six RCC patients and four HCC patients were marked by increased percentages whereas four RCC patients and six HCC patients showed decreased frequencies of monocytes/macrophages in NIL compared with TIL (figure 5 D).

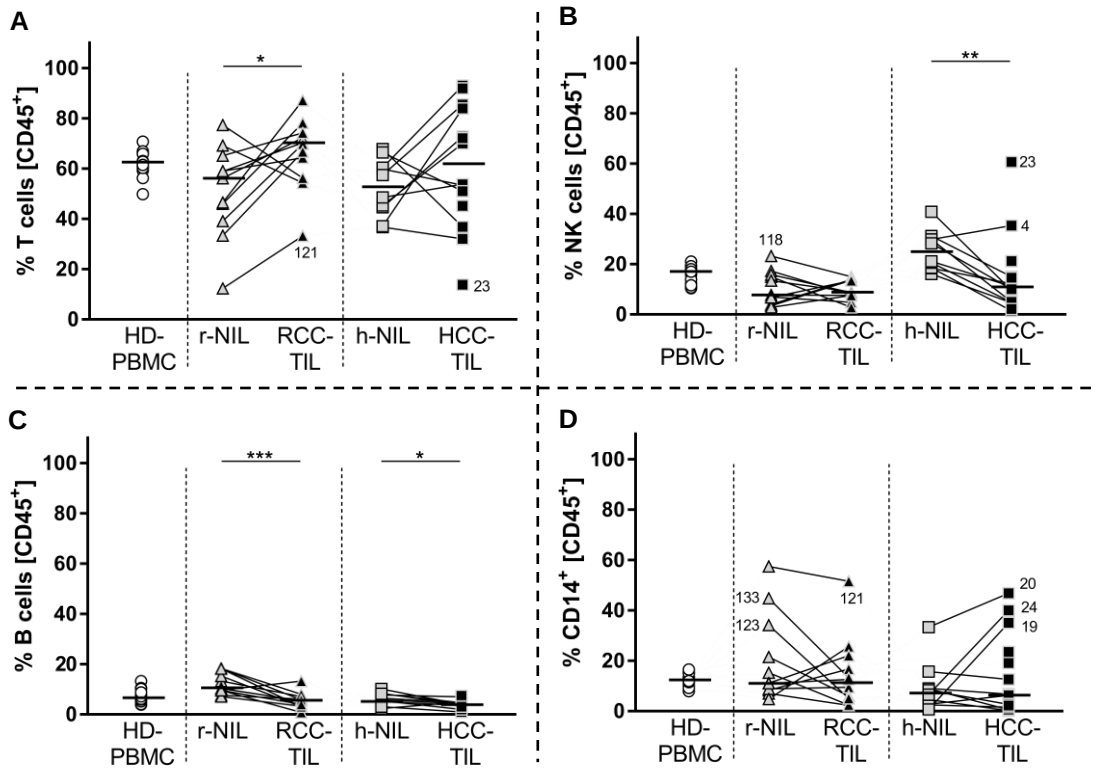

Figure 5: Composition of organ-resident immune cell infiltrates in non-tumor and tumor tissues of kidney and liver
Cell suspensions were stained for flow cytometry (table 15, see p. 51), leukocyte population frequencies were determined within the gated $CD45^+$/live cells (leukocytes) of tumor and non-tumor tissue of kidney and liver. Percentages of T cells (A), NK cells (B), B cells (C) and $CD14^+$ monocytes/macrophages (D) are shown. One symbol represents one patient or healthy donor, horizontal lines indicate the median of one group and vertical dashed lines separate HD-PBMC, kidney and liver resident T cells. Small numbers indicate patient-IDs and significance was statistically determined by Mann-Whitney U test within one group (*p<0.05; **p<0.01; ***p<0.001; ****p<0.0001). Only significant differences between samples are indicated.

Figure 6 A (see p. 58) summarizes the immune cell composition comparing RCC and HCC. Two groups of patients were identified in HCC-TIL with regard to percentages of T cells, one group with frequencies above and the other group with frequencies below those of HD-PBMC. Interestingly, the group of HCC-TIL with high percentages of T cells had low frequencies of monocytes/macrophages and also the RCC-TIL marked by low percentages of CD3 had high frequencies of monocytes/macrophages (figure 6 B). Percentages of NK cells and B cells were comparable in RCC-TIL, HCC-TIL and HD-PBMC, however, two outliers with increased frequencies of NK cells were found in HCC-TIL. Frequencies of monocytes/macrophages divided HCC-TIL in two groups, one group defined by increased and one group marked by decreased percentages compared with HD-PBMC. One outlier of RCC-TIL had increased frequencies of monocytes/macrophages, however, different groups of patients were not identified for RCC-TIL.

With regard to the two groups of HCC-TIL with high and low frequencies of T cells and monocytes/macrophages, it was next addressed if high percentages of T cells related with

high cell count of T cells in the tumor (figure 6 C). Of note is that the absolute cell count could not be determined of all patients due to experimental settings.

The cell count analysis revealed that two of five HCC-TIL with high percentages of T cells had high ($6.5 \times 10^5 – 2.8 \times 10^6$) and the other three patients had low ($0.1 \times 10^5 – 1.5 \times 10^6$) cell counts of T cells per ml tissue whereas all three HCC-TIL with low percentages of T cells had low cell counts ($0.1 \times 10^5 – 1.0 \times 10^6$). Similar findings were found for RCC-TIL: two of six RCC-TIL with high percentages of T cells were marked by high cell counts ($7.5 \times 10^5 – 5.6 \times 10^6$) and four had low cell counts ($0.1 \times 10^5 – 1.0 \times 10^6$) of T cells per ml tissue. One RCC patient having TIL with low frequencies of T cells had low cell counts (3.5×10^5). This indicates that high percentages of T cells cannot relate to high cell counts of T cells in the tissue. Therefore the analysis of frequencies as done by flow cytometry gating strategy needs to be interpreted with regard to cell type composition, however, the frequencies of cell types cannot be extrapolated to absolute cell numbers.

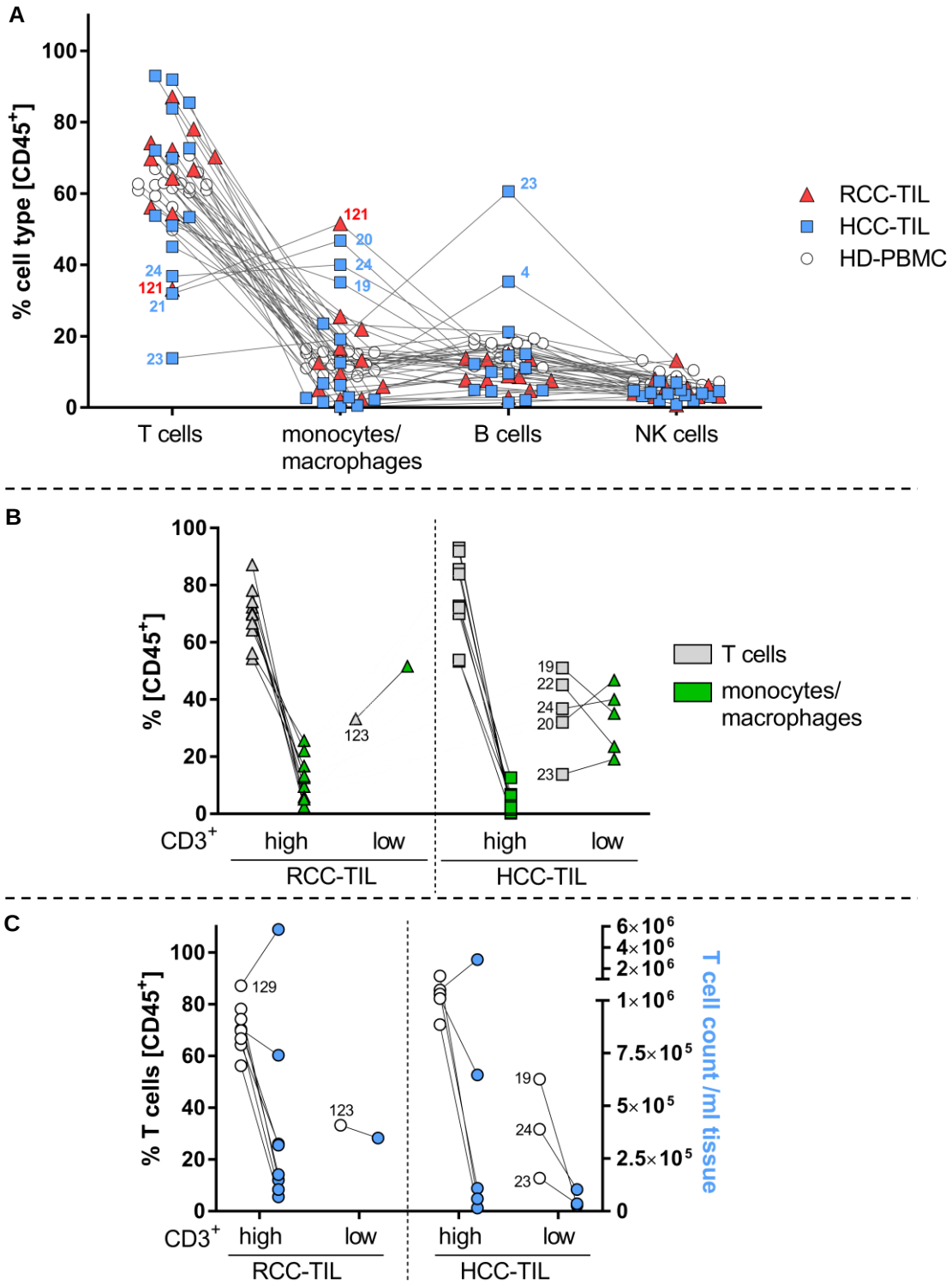

Figure 6: Patient-specific composition of immune cell infiltrates in tumor tissues of kidney and liver
Cell suspensions were stained for flow cytometry (table 15, see p. 51) A: Leukocyte population frequencies were determined within gated CD45$^+$/live cells (leukocytes) as described above (see p. 51); lines connect cell subtypes from one tissue. B: Relation of T cells and monocytes in groups of RCC-TIL and HCC-TIL with high and low percentages of T cells. Lines connect T cells and monocytes/macrophages from the same patient. C: Relation of percentages and absolute cell counts of T cells in RCC-TIL and HCC-TIL with high and low percentages of T cells. Cell counts were determined by Flow-Count Fluorospheres (see p. 46). Lines connect percentages and cell counts/ml tissue of T cells from the same patient. One symbol represents one individual and numbers are patient-IDs.

7.1.4 T cell subset distribution in leukocytes of non-tumor and tumor tissue of kidney and liver

In addition to cell density, the type of immune cell that is present in the tissue is important for the immune response (48). Based on the co-receptors CD4 and CD8, the T cell population can be subdivided into $CD8^+CD4^-$, $CD8^-CD4^+$, $CD8^-CD4^-$ and $CD8^+CD4^+$ within the gated $CD3^+CD56^+/CD56^-$ population.

Figure 7 A-D illustrates that the CD8 and CD4 subset distribution in leukocytes of non-tumor kidney was similar to that found in PBMC, while elevated percentages of $CD8^+CD4^-$ and correspondingly reduced percentages of $CD8^-CD4^+$ were observed in RCC-TIL. In h-NIL, $CD8^+CD4^-$ T cells were highly elevated compared with PBMC and also with HCC-TIL. Corresponding $CD8^-CD4^+$ T cell frequency was low in h-NIL and $CD8^+CD4^-$ T cell frequencies were high. $CD8^-CD4^-$ T cells were present at very low frequencies in tissue and absent in PBMC. $CD8^+CD4^+$ T cells were neither found in NIL nor TIL of liver and kidney tissue. Median values of each subset of all samples are summarized in figure 7 E.

To determine the tissue-individual T cell subset composition, the ratio of $CD8^+CD4^-$ to $CD8^-CD4^+$ T cells (CD4:CD8-ratio) was calculated (figure 7 F). T cells from non-tumor kidney and T cells from HD-PBMC showed a similar median CD4:CD8-ratio of 2 (range: 1.3 – 4.5). In contrast, T cells from non-tumor liver had much lower ratios (median 1; range: 0.2 – 0.8). T cells of both tumor tissues had intermediate ratios of 1.1 (RCC-TIL, range: 0.5 – 5.3) and 1.0 (HCC-TIL, range: 0.3 – 7.8) whereby TIL of five HCC patients had very high values exceeding the value of PBMC.

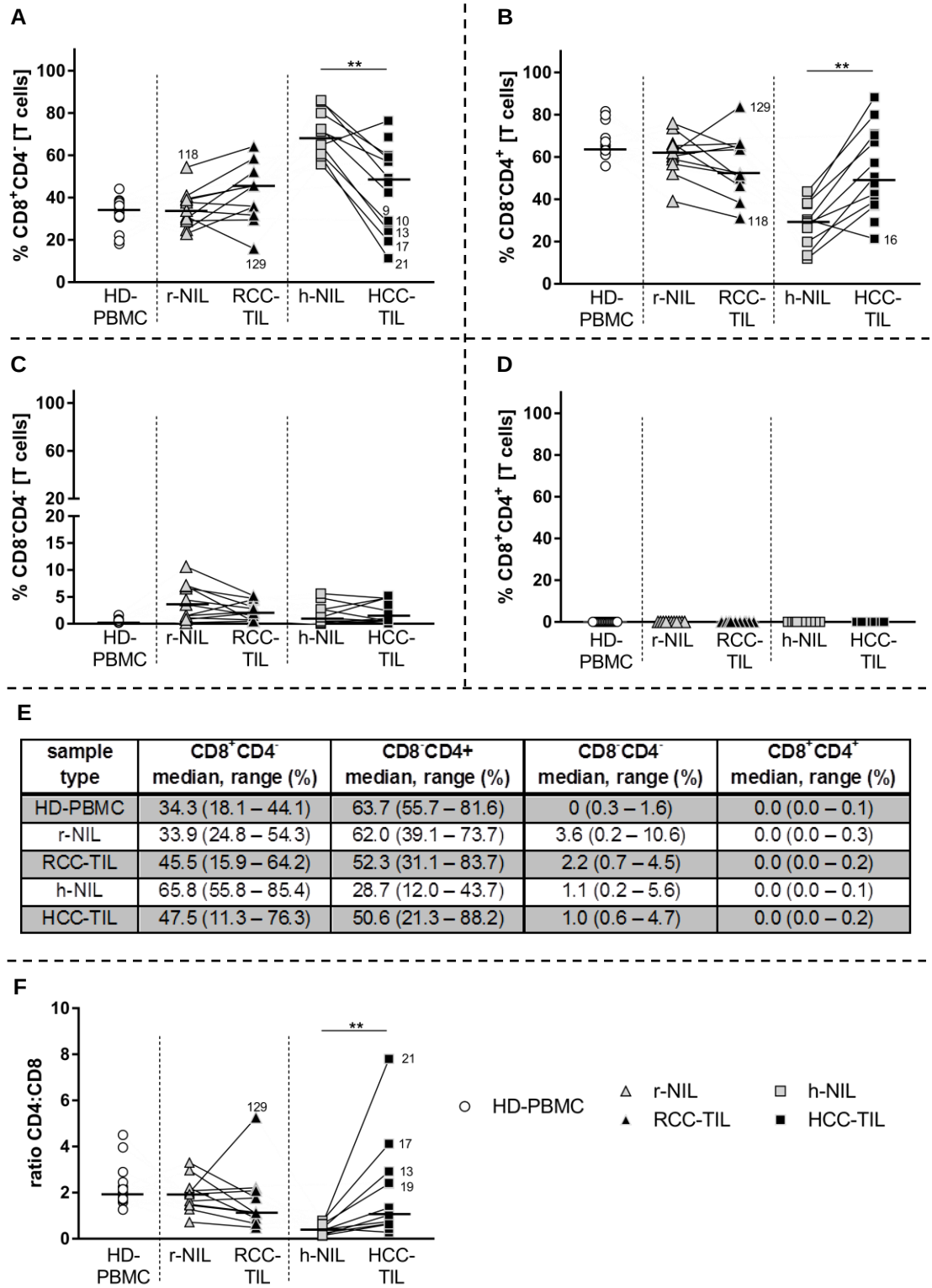

E

sample type	$CD8^+CD4^-$ median, range (%)	$CD8^-CD4+$ median, range (%)	$CD8^-CD4^-$ median, range (%)	$CD8^+CD4^+$ median, range (%)
HD-PBMC	34.3 (18.1 – 44.1)	63.7 (55.7 – 81.6)	0 (0.3 – 1.6)	0.0 (0.0 – 0.1)
r-NIL	33.9 (24.8 – 54.3)	62.0 (39.1 – 73.7)	3.6 (0.2 – 10.6)	0.0 (0.0 – 0.3)
RCC-TIL	45.5 (15.9 – 64.2)	52.3 (31.1 – 83.7)	2.2 (0.7 – 4.5)	0.0 (0.0 – 0.2)
h-NIL	65.8 (55.8 – 85.4)	28.7 (12.0 – 43.7)	1.1 (0.2 – 5.6)	0.0 (0.0 – 0.1)
HCC-TIL	47.5 (11.3 – 76.3)	50.6 (21.3 – 88.2)	1.0 (0.6 – 4.7)	0.0 (0.0 – 0.2)

Figure 7: T cell subsets in organ-resident leukocytes of non-tumor and tumor tissue of kidney and liver

Tissue suspensions were stained for flow cytometry (table 15, see p. 51), T cell subsets were determined within the gated $CD3^+/CD56^{+/-}$ T cells. A: $CD8^+CD4^-$ subset. B: $CD8^-CD4^+$ subset. C: $CD8^-CD4^-$ subset. D: $CD8^-CD4^-$ subset. E: Medians of all subsets in HD-PBMC and in organ-resident T cells of non-tumor and tumor tissues F: CD4:CD8 ratio. One symbol represents one patient or healthy donor, horizontal lines indicate the median of one group and vertical dashed lines separate HD-PBMC, kidney and liver resident T cells. Small numbers indicate patient-IDs. Significance was statistically determined by Mann-Whitney U test within one group (*p<0.05; ** p<0.01; *** p<0.001; ****p<0.0001). Only significant differences between samples are indicated.

7.2 Functional responsiveness of $CD8^+$ RCC-TIL and HCC-TIL

Besides density and subsets, the immune contexture also includes the functional responsiveness as an important parameter to describe a tissue immune state (48). Functional unresponsiveness of $CD8^+$ RCC-TIL to CD3 stimulation has been reported (4,40,69). In this thesis, the question was asked if the addition of CD28 co-stimulation improved functional activity. Moreover, a comparison between RCC-TIL and HCC-TIL was performed.

During a 5 h stimulation period, Interferon-gamma (IFN-γ) induction and degranulation (addressed by appearance of CD107a on the T cell surface) were measured and analyzed by flow cytometry (table 16). Since the patient's specific peptide-MHC combinations were not known, indirect stimulation with anti-CD3 was performed either alone or in combination with anti-CD28. PMA and Ionomycin (PMA/I) were used to reveal the T cells´ full response capacity. PMA/I activates T cells downstream of the proximal TCR signaling and thus allows stimulation of T cells circumventing proximal defects. Phorbol esters as PMA are direct activators of the protein kinase C (PKC); ionomycin also activates PKC in human T cells and induces Ca^{2+}/Calmodulin pathways (70). Therefore, if TIL had proximal defects in the signaling cascade, they could be overcome by stimulation with PMA/I.

Table 16: Staining combination for analysis of T cell function (staining combination 6)

Target/epitope	Fluorochrome	Cell subset/function
Viability: LIVE/DEAD™ Fixable Blue Dead Cell Stain	Indo-1-violet	staining of dead cells
CD107	APC	degranulation marker
CD45	Pe-Cy7	leukocytes
CD3	Alexa Fluor® A700	T cells
CD8	V500	$CD8^+$ T cells
CD4	APC-eFluor 780	$CD4^+$ T cells
CD19/CD20	BV421	B cells
CD56	BV421	NK cells
PD-1	PE	exhaustion marker
IFN-γ	PerCp-Cy5.5™	IFN-γ production
Ki-67	PE-TexasRed®	proliferation marker
CD28	FITC	co-stimulatory molecule

7.2.1 T cells with function

Figure 8 summarizes the results from all analyzed samples depicting T cells with function as percentage of the gated live $CD3^+CD8^+$ T cells. As expected, frequencies of $CD3^+CD8^+$ T cells with function were low in unstimulated samples of RCC-TIL (median 4%; range: 1% - 5%), HCC-TIL (median 4%; range: 3% - 10%) and activated T cells (median 5%; range: 1% - 13.5%). Stimulation with anti-CD3 did not increase the frequency of T cells with function among RCC-TIL (median 5%; range: 4% - 24%) and HCC-TIL (median 5%; range: 4.5 % - 18%) whereas activated T cells responded to anti-CD3 stimulation showing significant higher levels of T cells with function (median 76%; range: 42% - 97%). When additional co-stimulation by anti-CD3/CD28 stimulation was provided, activated T cells responded even better with a median frequency of T cells with function of 85% (range: 77% - 98%), while T cells with function remained low in RCC-TIL (median 9%; range: 3% - 17%) and HCC-TIL (median 11%; range: 5% - 20%). Stimulation with PMA/I enabled response in a fraction of T cells of RCC-TIL (median 45%; range: 26% - 85%) and HCC-TIL (median 54%; range: 37% - 78%), but frequencies remained significantly below those of activated T cells (median 98%; range: 91% - 99%), indicating that functional blockades exist in TIL that are in pathways downstream of the PMA/I. Of note is that two of four RCC-TIL responded well to PMA/I stimulation whereas two RCC-TIL responded poorly suggesting that subgroups of RCC-TIL might exist.

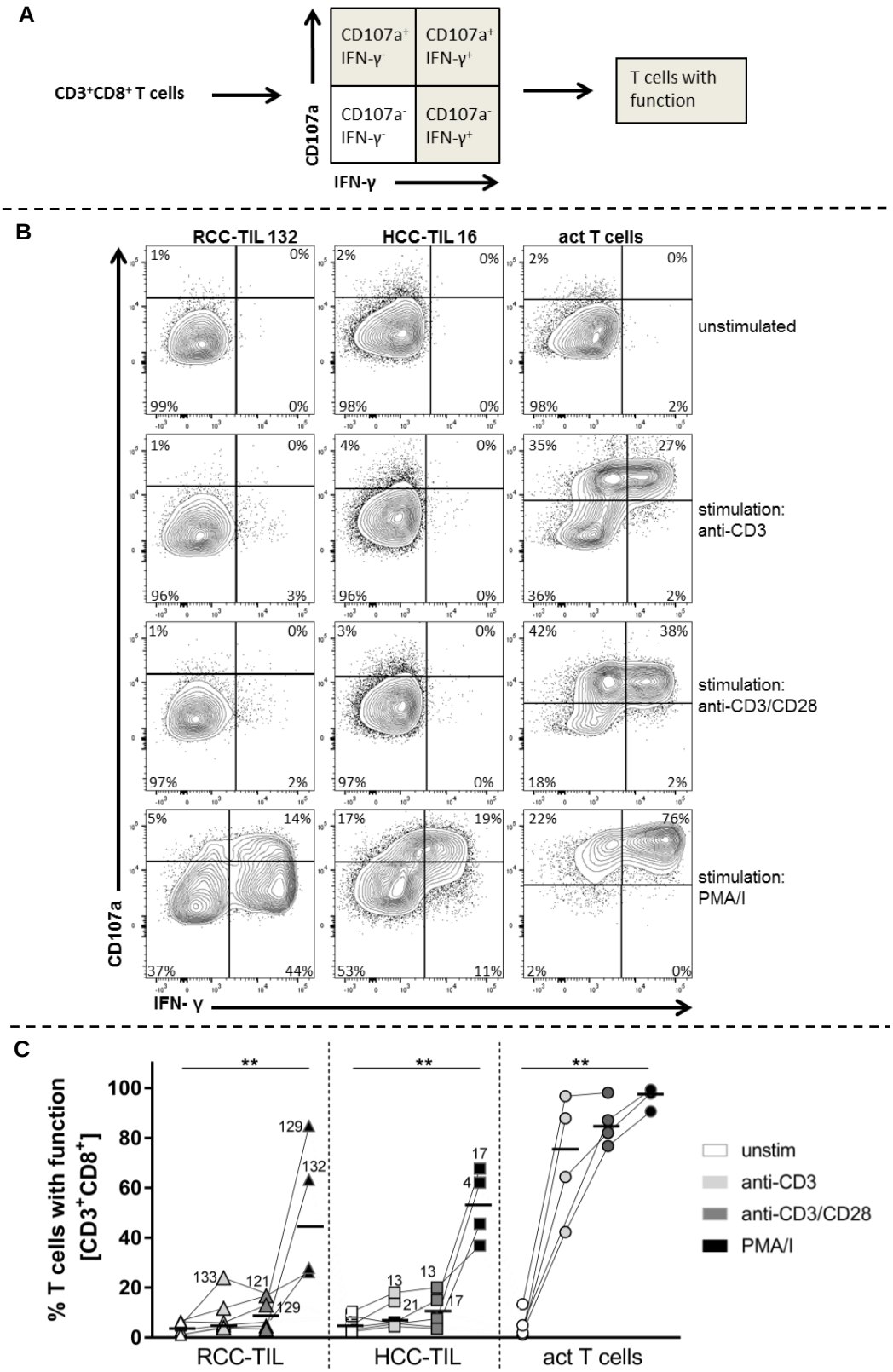

Figure 8: T cells with function in activated T cells, RCC-TIL and HCC-TIL upon different stimulation
Tissue suspensions and activated T cells (act T cells) were thawed, stimulated with anti-CD3, anti-CD3/CD28 and PMA/Ionomycin (PMA/I) as described above (see p. 37) and stained for flow cytometry (table 16, see p. 61). After gating of $CD3^+CD8^+$ T cells, T cells with function were determined as positive for IFN-γ, CD107a or both. A: Schematic gating strategy. B: Exemplary dot plots. C: Frequencies of T cells with function as percentages of $CD3^+CD8^+$ T cells in RCC-TIL, HCC-TIL and activated T cells. Shades of grey of the symbols correspond to different stimulation methods (white: unstimulated (unstim), light grey: anti-CD3, dark grey: anti-CD3/CD28, black: PMA/I). One symbol represents one sample of activated T cells or one patient,

horizontal lines are median values of one group, dashed lines separate groups. Significance was statistically determined by Kruskal-Wallis test and Dunn´s Post-hoc comparisons (*p<0.05; **p<0.01; ***p<0.001; ****p<0.0001). Only significant differences between samples are indicated. Numbers are patient-IDs.

7.2.2 Functional profile of $CD8^+$ TIL

The subset of $CD8^+$ T cells that responded to stimulation was subdivided according to the type of function they performed, i.e. only degranulation, only IFN-γ production or being poly-functional with degranulation and IFN-γ production. This resulted in a functional profile of $CD8^+$ T cells (figure 9 A).

Upon anti-CD3 stimulation (figure 9 B), the profile of responding T cells was comparable between RCC-TIL and HCC-TIL but different to that of activated T cells. $CD8^+$ T cells of both RCC-TIL and HCC-TIL were dominated by degranulating cells without IFN-γ production ($CD107a^+IFN\text{-}\gamma^-$; mean RCC-TIL 58%; mean HCC-TIL 60%) whereas the main subgroup of activated T cells was poly-functional ($CD107a^+IFN\text{-}\gamma^+$; mean 53%). Interestingly, medium frequencies of $CD107a^-IFN\text{-}\gamma^+$ (mean RCC-TIL 36%, mean HCC-TIL 31%) were higher in TIL compared with activated T cells (mean 14%). Both TIL had low percentages of poly-functional ($CD107a^+IFN\text{-}\gamma^+$) cells (mean RCC-TIL 6%, mean HCC-TIL 9%).

The analysis of individual patients (figure 9 C) revealed, that a group of four HCC-TIL and four RCC-TIL had high percentages of degranulating T cells without IFN-γ production ($CD107a^+IFN\text{-}\gamma^-$; range HCC-TIL: 69 – 92%; range RCC-TIL: 56 -93%). Those TIL had corresponding low frequencies of T cells producing IFN-γ only ($CD107a^-IFN\text{-}\gamma^+$; range RCC-TIL: 6 - 37%; range HCC-TIL: 6 – 25%). On the contrary, two HCC-TIL and four RCC-TIL had low percentages of $CD107a^-IFN\text{-}\gamma^+$ T cells (range RCC-TIL: 23 – 26%, range HCC-TIL: 20 – 34%) corresponding to high frequencies of $CD107a^-IFN\text{-}\gamma^+$ cells (range RCC-TIL: 67 – 70%; range HCC-TIL: 54 – 79%).

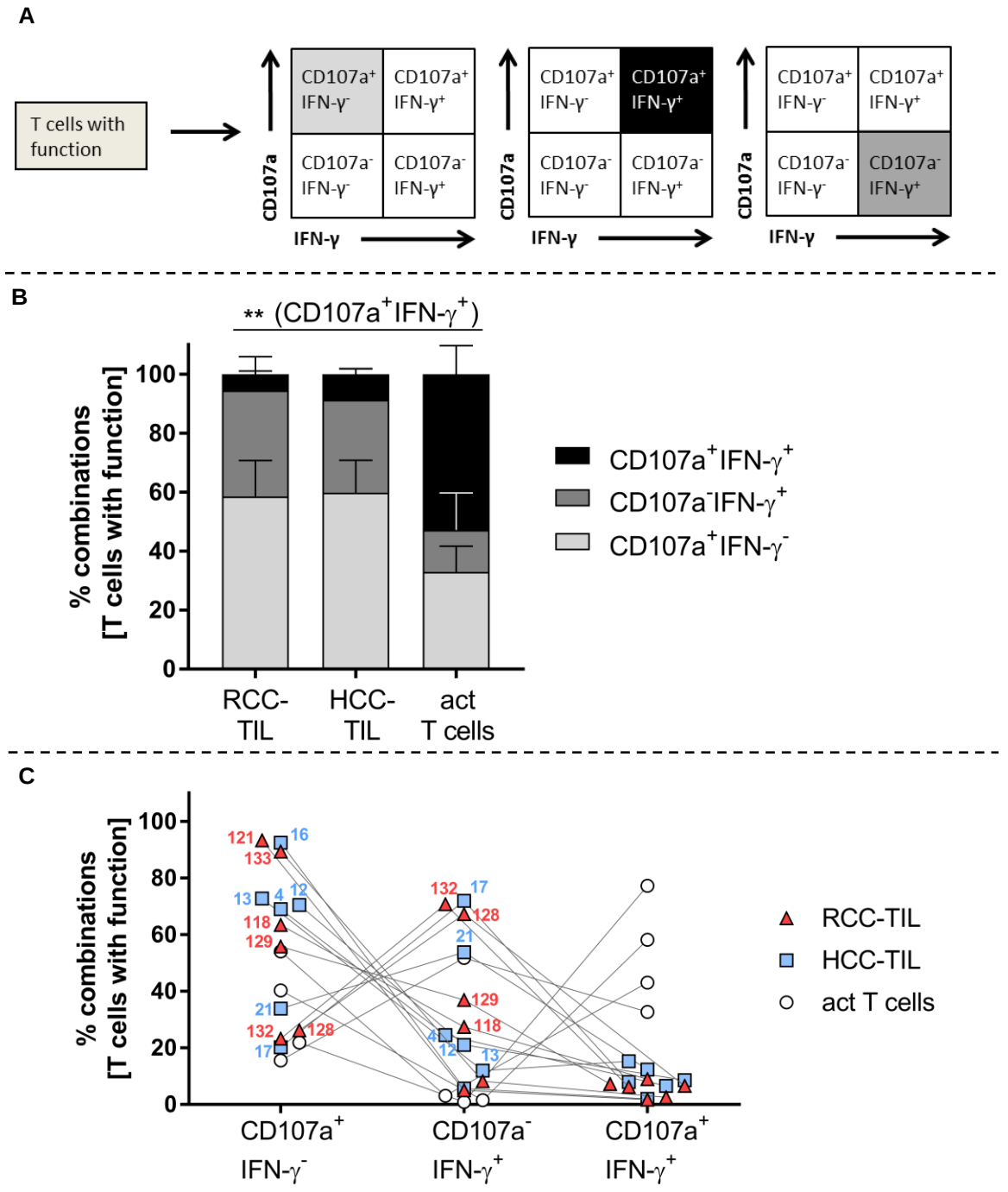

Figure 9: Functional profile of CD8$^+$ T cells from tumor tissues of kidney and liver and activated T cells upon anti-CD3 stimulation

Tissue suspensions and activated T cells were thawed, stimulated as described above (see p. 37) and stained for flow cytometry (table 16, see p. 61). After selection of CD3$^+$CD8$^+$ T cells, T cells with function were determined as positive for IFN-γ, CD107a or both. A: The functional profile of T cells responding to anti-CD3 stimulation was determined within gated CD8$^+$ T cells with function and defined as degranulation without IFN-γ production, (CD107a$^+$IFN-γ$^-$, light grey), poly-functional T cells (CD107a$^+$IFN-γ$^+$, black) and IFN-γ production without degranulation (CD107a$^-$IFN-γ$^+$, dark grey) B: Profile of CD8$^+$ T cells upon anti-CD3 stimulation in RCC-TIL, HCC-TIL and activated T cells. The height of the bars represents the mean of each group and error bars indicate the standard error of the mean. Significance was statistically determined by Kruskal-Wallis test and Dunn´s Post-hoc comparisons (*p<0.05; **p<0.01; ***p<0.001; ****p<0.0001). Only significant differences between samples are indicated. C: Profile of CD8$^+$ T cells with function upon anti-CD3 stimulation in RCC-TIL, HCC-TIL and activated T cells to visualize variances between patients. Each symbol represents one patient or sample of activated T cells and lines connect samples from the same individual. Small numbers indicate patient-IDs (red: RCC-TIL, blue: HCC-TIL).

Next, the question was asked if the functional profile of $CD8^+$ T cells changed upon different stimulation conditions of anti-CD3, anti-CD3/CD28 and PMA/I.

Percentages of degranulating T cells without IFN-γ production ($CD107a^+IFN\text{-}\gamma^-$) decreased gradually from anti-CD3 to anti-CD3/CD28 to PMA/I stimulus in RCC-TIL, HCC-TIL and activated T cells. Highest frequencies were found upon anti-CD3 stimulation and lowest percentages were detected upon PMA/I stimulation.

In contrast, percentages of IFN-γ producing T cells that did not degranulate ($CD107a^-IFN\text{-}\gamma^+$) increased in RCC-TIL, HCC-TIL and activated T cells upon anti-CD3/CD28 stimulation; however, PMA/I stimulation did not lead to higher percentages. Frequencies of poly-functional T cells were comparable in RCC-TIL and HCC-TIL after anti-CD3 and anti-CD3/CD28 stimulation and increased upon PMA/I treatment. This was also found in activated T cells, although percentages of poly-functional T cells were in general higher in activated T cells compared with TIL.

A

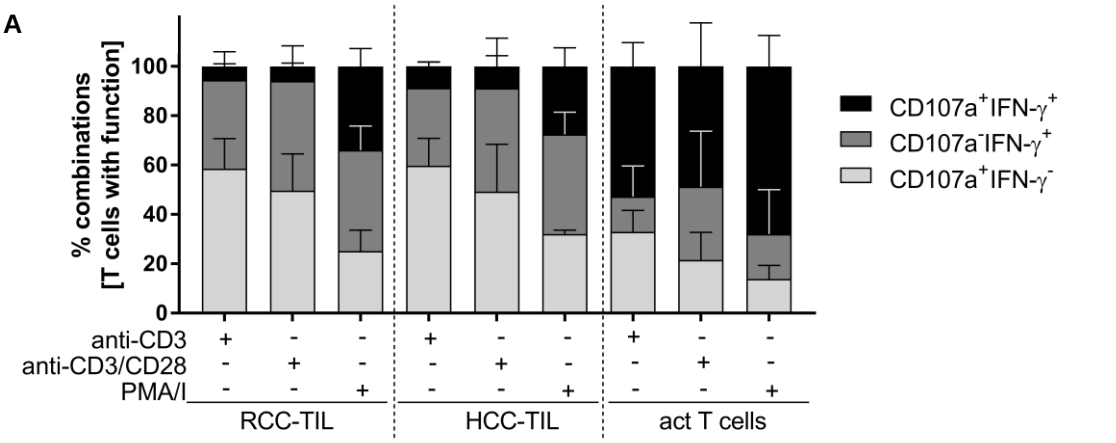

B

		mean and range (%)		
sample type	**stimulation**	**CD107a$^+$IFN-γ$^-$**	**CD107a$^-$IFN-γ$^+$**	**CD107a$^+$IFN-γ$^+$**
RCC-TIL	anti-CD3	58.5 (23.2 – 93.3)	35.9 (5.0 – 70.7)	5.6 (1.7 – 8.1)
	anti-CD3/CD28	49.6 (24.1 – 29.8)	44.4 (7.5 – 69.5)	6.0 (2.7 – 9.2)
	PMA/I	25.1 (8.8 – 47.8)	40.9 (24.5 - 68.0)	34.0 (32.2 – 55.5)
HCC-TIL	anti-CD3	59.8 (20.2 – 92.4)	31.4 (5.7 – 71.9)	8.8 (1.9 – 15.3)
	anti-CD3/CD28	49.3 (4.7 – 91.3)	41.8 (7.0 – 91.1)	8.9 (1.7 – 18 5)
	PMA/I	32.0 (28.3 – 35.7)	40.4 (21.6 – 59.3)	27.6 (12.3 – 44.9)
act T cells	anti-CD3	32.9 (15.5 – 54.0)	14.3 (1.0 – 51.7)	52.8 (32.7 – 77.2)
	anti-CD3/CD28	21.5 (0.6 – 52.1)	29.8 (2.8 – 96.0)	48.1 (3.3 – 88.4)
	PMA/I	13.9 (3.1 - 21.0)	18.2 (0.3 – 54)	67.9 (24.8 – 82.2)

Figure 10: Functional profile of CD8$^+$ T cells from tumor tissues of kidney and liver and activated T cells upon stimulation with anti-CD3, anti-CD3/CD28 and PMA/I
Tissue suspensions and activated T cells (act T cells) were thawed, stimulated with anti-CD3, anti-CD3/CD28 and PMA/Ionomycin (PMA/I) as described above (see p. 37) and stained for flow cytometry (table 16, see p. 61). T cells with function were determined as positive for IFN-γ, CD107a or both within preselected CD3$^+$CD8$^+$ T cells. The functional profile of CD8$^+$ T cells responding to stimulation was further addressed within gated T cells with function and defined as degranulation without IFN-γ production (CD107a$^+$IFN-γ$^-$, light grey), poly-functional T cells (CD107a$^+$IFN-γ$^+$, black) and IFN-γ production without degranulation (CD107a$^-$ IFN-γ$^+$, dark grey). A: Profile of CD8$^+$ T cells upon anti-CD3, anti-CD3/CD28 and PMA/I stimulation in RCC-TIL, HCC-TIL and activated T cells. The height of the bars represents the mean of each group and error bars indicate the standard error of the mean. Significance was statistically determined by Kruskal-Wallis test and Dunn´s Post-hoc comparisons (*p<0.05; **p<0.01; ***p<0.001; ****p<0.0001). Only significant differences between samples are indicated. B: Table summarizes median and ranges of combinations within pregated T cells with function in RCC-TIL, HCC-TIL and activated T cells upon stimulation with anti-CD3, anti-CD3/CD28 and PMA/I.

7.2.3 Can markers of proliferation (Ki-67), PD-1 or CD28 delineate T cell function of TIL?

The proliferation marker Ki-67, co-inhibitory receptor PD-1 and co-stimulatory receptor CD28 have been associated with CD8$^+$ effector function:

Ki-67 is expressed in proliferating cells and its level remains low during G_0/G_1 transition, raises during S phase and is highest during mitosis. Therefore, Ki-67 can be used as a biomarker to estimate proportions of dividing cells (71). Moreover, it has been reported that the number of CD8$^+$Ki-67$^+$ lymphocytes in RCC tissue was associated with longer patient survival (72). This raised the question if Ki-67 in RCC-TIL and HCC-TIL could be used as a marker for the quality of the TIL population in a tissue. Specifically, the

hypothesis was formulated if Ki67 expression could be used to distinguish TIL with functional profile from those without function as defined by positivity of CD107a and IFN-γ production in response to stimulation with anti-CD3, anti-CD3/CD28 or PMA/I.

Programmed cell death protein 1 (PD-1) has been described as a marker for exhausted $CD3^+CD8^+$ T cells (41). Furthermore, findings in chronic viral infections like hepatitis C virus (73) or HIV (74) indicate a correlation of PD-1 expression and impaired function of $CD8^+$ T cells: i.e. virus specific T cells with PD-1 expression were found to have reduced capacity to proliferate, to expand and to produce cytokines. Similarly, PD-1 expressing TIL of melanoma were impaired in the production of IFN-γ and IL-2 upon stimulation with PMA/I compared with PD-1 negative TIL (75). Thus, it was addressed if a similar association can also be found for RCC-TIL and HCC-TIL.

In healthy individuals, $CD8^+CD28^-$ T cells are described as terminally differentiated effector population (76,77) that contains elevated levels of perforin and IFN-γ compared with $CD8^+CD28^+$ T cells (77). Therefore it was addressed if $CD8^+CD28^-$ RCC-TIL and HCC-TIL show higher levels of T cells with function compared with the $CD8^+CD28^-$ subset.

To determine if Ki-67, PD-1 and CD28 might delineate $CD8^+$ T cells with effector function of activated T cells, RCC-TIL and HCC-TIL, the percentages of each markers in preselected $CD8^+$ T cells were analyzed in unstimulated controls and upon different stimulation conditions (figure 11).

Activated T cells had highest percentages of Ki-67 (median 48%; range: 22 - 63%) while $Ki\text{-}67^+$ cells were infrequent with median percentages of 4% (RCC-TIL, range: 3 – 10%) and 8% (HCC-TIL, range: 3 – 16%). With regard to co-inhibitory receptor PD-1, median percentages of RCC-TIL of 65% (range: 28 – 75%) were detected and HCC-TIL (median over all samples 41%) were separated into two groups with low (range: 16 – 41%) and high (range: 83 – 97%) frequencies. PD-1 was not detected in activated T cells. Percentages of CD28 in activated T cells differed to a high degree (31% and 68%). The high variance of CD28 percentages in activated T cells might be due to low numbers of experiments (n=2 for CD28 in activated T cells). Percentages of $CD28^+$ cells divided RCC-TIL and HCC-TIL into two groups and the main cohort had median frequencies of 35% (RCC-TIL) and 41% (HCC-TIL). The second group was defined by one patient of RCC (68%) and one patient of HCC (69%).

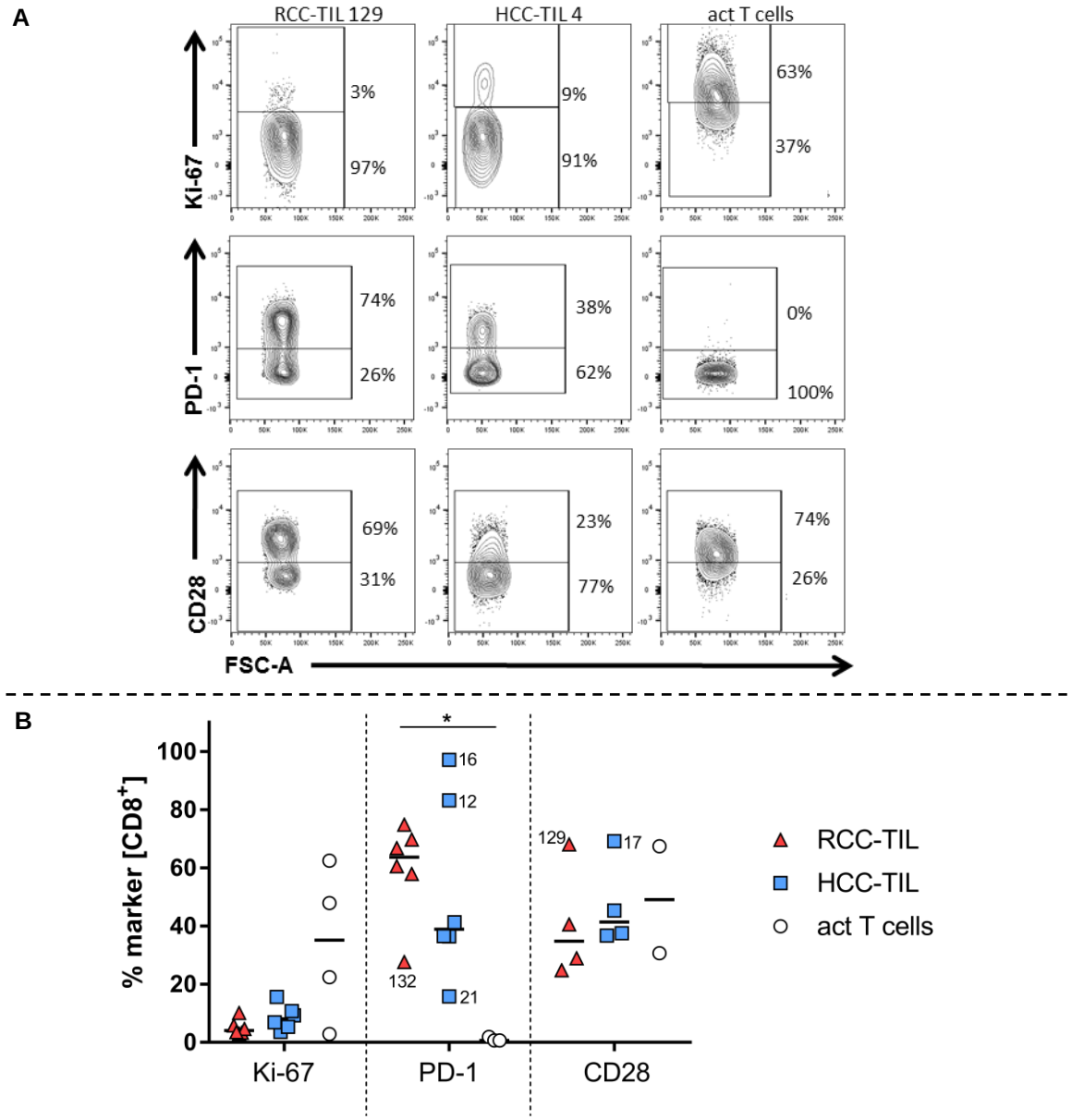

Figure 11: Percentages of Ki-67, PD-1 and CD28 in RCC-TIL, HCC-TIL and activated T cells
Tissue suspensions and activated T cells (act T cells) were thawed as described above (see p. 37) and stained for flow cytometry (table 16, see p. 61). Percentages of the markers Ki-67, PD-1 and CD28 were determined within pregated $CD8^+$ RCC-TIL, HCC-TIL and activated T cells. A: Exemplary dot plots. B: Summarizing graph of percentages of each marker in $CD8^+$ RCC-TIL, HCC-TIL and activated T cells. Significance was statistically determined by Kruskal-Wallis test and Dunn´s Post-hoc comparisons (*p<0.05; **p<0.01; ***p<0.001; ****p<0.0001). Only significant differences between samples are indicated. One symbol represents one TIL or sample of activated T cells, horizontal lines indicate the median of one group and vertical dotted lines separate different groups. Small numbers indicate patient-IDs.

To address if Ki-67, PD-1 or CD28 might delineate $CD8^+$ T cell function, $CD8^+$ T cells were divided into subsets positive or negative for Ki-67, PD-1 or CD28. Then T cells with function defined by positivity for either CD107a or IFN-γ or both were determined in these subsets after stimulation with anti-CD3, anti-CD3/CD28 or PMA/I. Figure 12 shows the gating strategy (A) and exemplary dot plots of PMA/I treated samples (B).

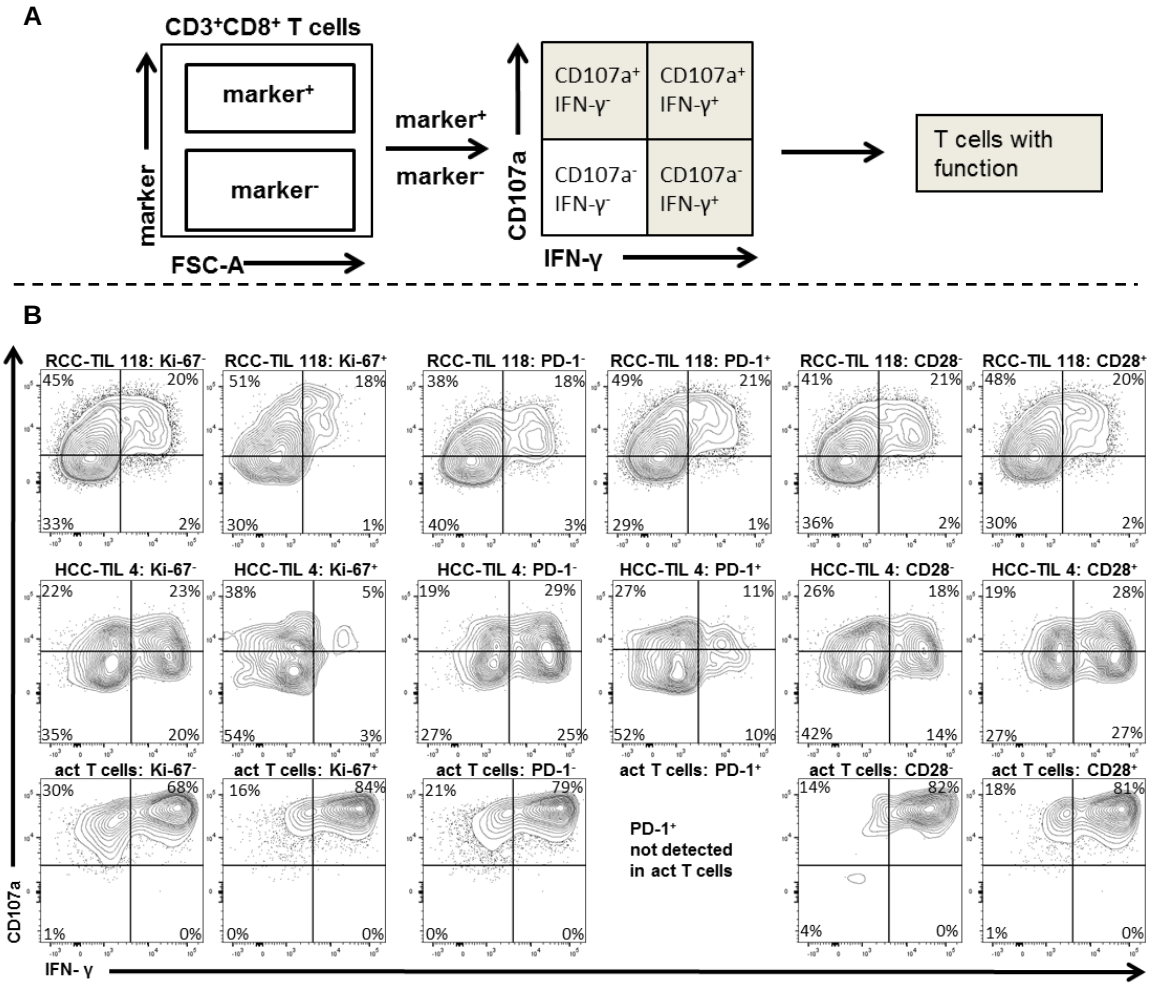

Figure 12: Gating strategy and exemplary dot plots to determine the function profile of CD8$^+$ TIL or activated T cells in subsets of Ki-67, PD-1 and CD28 T cells
Activated T cells, RCC-TIL and HCC-TIL were used unstimulated or stimulated with anti-CD3, anti-CD3/CD28 or PMA/Ionomycin (PMA/I) as described above (see p. 37) and stained for flow cytometry (table 16, see p. 61). A: Gating strategy determining T cells with function in subsets of Ki-67, PD-1 and CD28 within preselected CD3$^+$CD8$^+$ T cells. B: Exemplary dot plots of PMA/I stimulated RCC-TIL, HCC-TIL activated T cells (act T cells), gated on negative or positive subsets of Ki-67, PD-1 and CD28. Gates were set based on unstimulated controls. PD-1$^+$ subset was not detected in act T cells (figure 11, see p. 69).

T cells responsive to CD3 stimulation were enriched in Ki-67$^+$ compared with Ki-67$^-$ subset of CD8$^+$ RCC-TIL and HCC-TIL (figure 13 A). With PMA/I stimulation, this association was lost. Activated T cells had comparable percentages of T cells with function in Ki-67$^-$ and Ki-67$^+$ subsets.

Functional responsive CD8$^+$ T cells were similar distributed in PD-1$^-$ and PD-1$^+$ subsets of CD8$^+$ RCC-TIL and slightly less prevalent in the PD-1$^-$ subset in HCC-TIL (figure 13 B). Activated T cells were not PD-1$^+$, therefore a comparison was not possible.

No association was found between CD28 and RCC-TIL responding to stimulation, while the CD28$^+$ TIL subset showed an enriched functional response in CD8$^+$ HCC-TIL (figure 13 C).

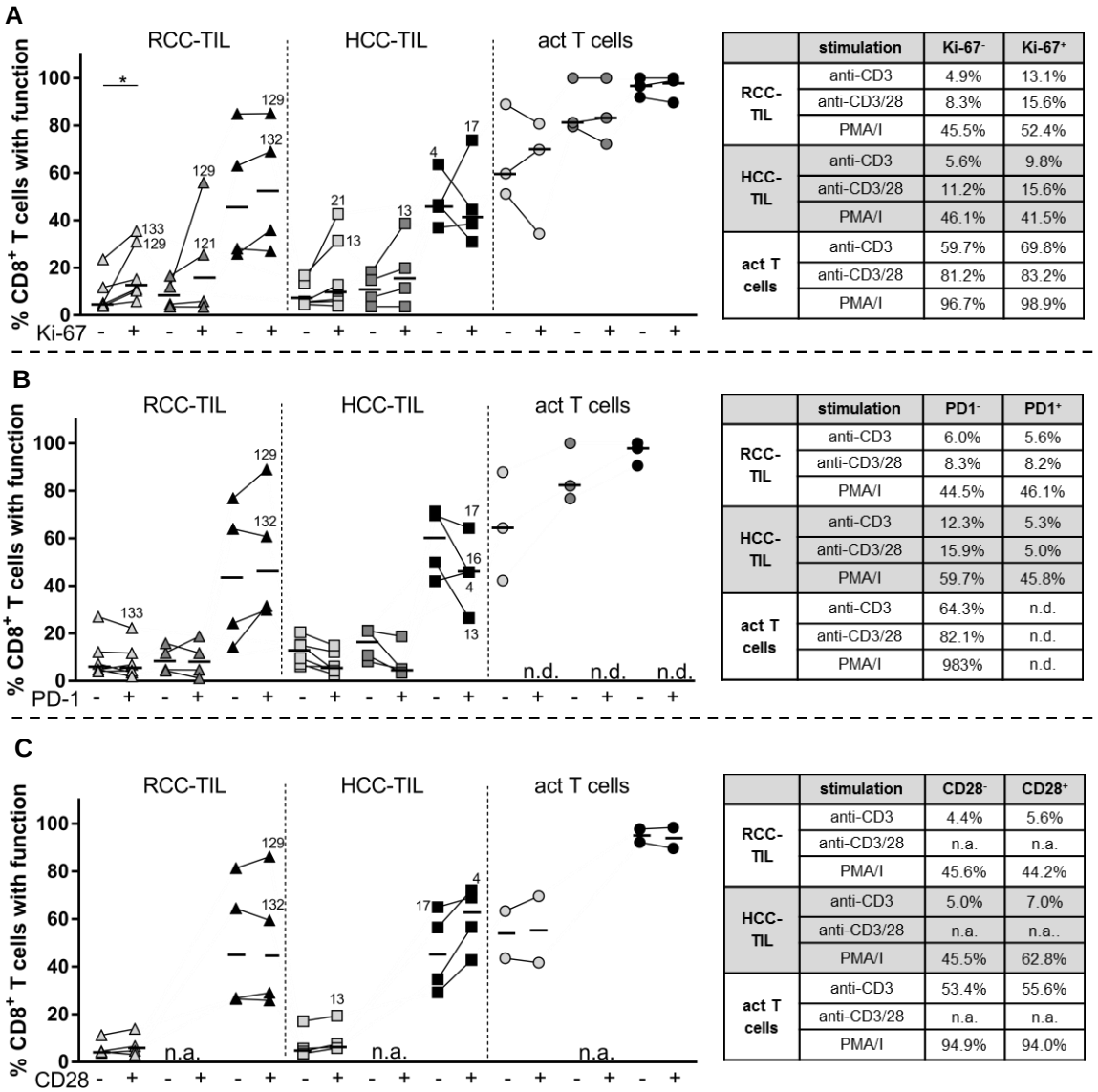

	stimulation	Ki-67⁻	Ki-67⁺
RCC-TIL	anti-CD3	4.9%	13.1%
	anti-CD3/28	8.3%	15.6%
	PMA/I	45.5%	52.4%
HCC-TIL	anti-CD3	5.6%	9.8%
	anti-CD3/28	11.2%	15.6%
	PMA/I	46.1%	41.5%
act T cells	anti-CD3	59.7%	69.8%
	anti-CD3/28	81.2%	83.2%
	PMA/I	96.7%	98.9%

	stimulation	PD1⁻	PD1⁺
RCC-TIL	anti-CD3	6.0%	5.6%
	anti-CD3/28	8.3%	8.2%
	PMA/I	44.5%	46.1%
HCC-TIL	anti-CD3	12.3%	5.3%
	anti-CD3/28	15.9%	5.0%
	PMA/I	59.7%	45.8%
act T cells	anti-CD3	64.3%	n.d.
	anti-CD3/28	82.1%	n.d.
	PMA/I	983%	n.d.

	stimulation	CD28⁻	CD28⁺
RCC-TIL	anti-CD3	4.4%	5.6%
	anti-CD3/28	n.a.	n.a.
	PMA/I	45.6%	44.2%
HCC-TIL	anti-CD3	5.0%	7.0%
	anti-CD3/28	n.a.	n.a..
	PMA/I	45.5%	62.8%
act T cells	anti-CD3	53.4%	55.6%
	anti-CD3/28	n.a.	n.a.
	PMA/I	94.9%	94.0%

Figure 13: CD8$^+$ T cells with function in Ki-67$^{-/+}$, PD-1$^{-/+}$ and CD28$^{-/+}$ subsets in RCC-TIL, HCC-TIL and activated T cells upon different stimulation conditions

Activated T cells, RCC-TIL and HCC-TIL were used unstimulated or stimulated with anti-CD3, anti-CD3/CD28 or PMA/Ionomycin (PMA/I) and stained for flow cytometry (table 16, see p. 61). CD8$^+$ T cells with function were determined in subsets of Ki-67$^{-/+}$, PD-1$^{-/+}$ and CD28$^{-/+}$ of preselected CD8$^+$ T cells as previously shown (see p. 70). Percentages of CD8$^+$ T cells with function are visualized in subsets of Ki-67 (A), Ki-67 (B) and PD-1 (C) of RCC-TIL, HCC-TIL and activated T cells (act T cells). Tables summarize median values of the groups, one symbol represents one TIL or sample of activated T cells, lines connect samples of the same individual in negative and positive subsets. Shades of grey of the symbols represent different stimulation conditions (light grey: anti-CD3, dark grey: anti-CD3/CD28, black: PMA/I). Horizontal lines indicate medians of one group and vertical dashed lines separate different groups. Significance was statistically determined by Wilcoxon matched pairs signed rank test between two corresponding subsets (*p<0.05; **p<0.01; ***p<0.001; ****p<0.000). Only significant differences between samples are indicated and small numbers indicate patient-IDs. n.a.: not assessable; n.d.: not detected.

7.3 Cell cycle state of TIL

CD8$^+$ RCC-TIL and CD8$^+$ HCC-TIL showed low frequencies of Ki-67 within CD8$^+$ T cells (figure 11, see p. 69). To elucidate possible causes for the poor proliferation, the cell cycle of RCC-TIL and HCC-TIL was analyzed.

Cell cycle progression is regulated by cyclin-dependent kinases (CDK) which are catalytic active or inactive through association with regulatory subunits (cyclins) and inhibitory proteins such as $p27^{kip1}$ (78,79).

The phases of the cell cycle can be approximated by levels of cyclin E and $p27^{kip1}$ which is visualized in figure 14 A (see p. 74): Low levels of cyclin E (light brown) and $p27^{kip1}$ (light green) are related to G_0 and G_1 phase, as well as G_2 and M phase. During late G_1 and early S phase levels of cyclin E are high (dark brown) but $p27^{kip1}$ is low. The S phase is characterized by high levels of cyclin E and $p27^{kip1}$ (dark green) whereas in late S phase cyclin E levels start to decline and $p27^{kip1}$ levels remain high. During G_2 and M phase, levels of cyclin E and $p27^{kip1}$ are low (26,27).

To determine the cell cycle state of RCC-TIL and HCC TIL, TIL and activated T cells were stained for cyclin E and $p27^{kip1}$ and analyzed by flow cytometry. The staining combination is shown in table 17.

Table 17: Staining combination to examine cell cycle state of TIL (staining combination 3). The markers pAKT(S473) and pERK(T202/Y201) are addressed later (see p. 75)

Target/epitope	Fluorochrome	Cell subset/function
Viability: LIVE/DEAD™ Fixable Blue Dead Cell Stain	Indo-1-violet	staining of dead cells
CD45	Pe-Cy7	leukocytes
CD3	PerCp-Cy™5.5	T cells
$p27^{kip1}$	PE	CDK- inhibitor
cyclin E	FITC	cell cycle protein
pAKT (S473)	V450	AKT phosphorylated at S473
p-p44/42 MAPK (pERK(T202/Y204))	unmarked, detected by secondary antibody (Alexa Fluor® 647)	MAPK (ERK) phosphorylated at T202 and Y204

In activated T cells, RCC-TIL and HCC-TIL, low and high frequencies of cyclin E within gated $CD3^+$ T cells could be distinguished; however, cyclin E negative cells did not exist (figure 14 B). Activated T cells were primarily cyclin E high whereas the main population of RCC-TIL and HCC-TIL was cyclin E low.

Based on the combination of cyclin E and $p27^{kip1}$ (figure 14 C), T cells were distinguished into four cell cycle subsets: $G_0/G_2/M$ (cyclin $E^{low}/p27^{kip1-}$), late G_1/early S (cyclin $E^{high}/p27^{kip1-}$), S (cyclin $E^{high}/p27^{kip1+}$) and late S (cyclin $E^{low}/p27^{kip1+}$). Comparing the frequencies of each subset in RCC-TIL, HCC-TIL and activated T cells, it was observed

that TIL were predominantly cyclin E^{low} and $p27^{kip1-}$, placing them into the G_0, G_2 or M phase of the cell cycle (figure 14 D). Activated T cells showed high levels of cyclin E and were $p27^{kip1-}$suggesting that they are in late G_1 or early S phase.

In HCC-TIL, five patients had higher frequencies (13% – 23%) of cyclin $E^{high}p27^{kip1-}$ T cells. while the other HCC-TIL had frequencies around 3% similar to all RCC-TIL. T cells in the S phase of the cell cycle (characterized by cyclin $E^{high}p27^{kip1+}$) were not found in RCC-TIL and HCC-TIL and were present at low frequency in activated T cells (median 4%; range: 2% – 9%). T cells in the late S phase (cyclin $E^{low}p27^{kip1+}$) were not detected in activated T cells and had low levels in RCC-TIL (median 1%; range: 0% – 6%) and HCC-TIL (median 1%; range: 0% – 4%).

Taken together, activated T cells were mainly proliferating and in late G_1 or early S phase of the cell whereas the main cohorts of $CD3^+$ RCC-TIL and HCC-TIL were in the G_0, G_2 or M phase of the cell cycle. The cell cycle phase of TIL can be more precisely located utilizing the knowledge of Ki-67, as Ki-67 is expressed in G_2 or M (71). Since less than 10% of $CD8^+$ TIL were Ki-67^+ (figure 11, see p. 69), RCC-TIL and HCC-TIL were mostly in the quiescent G_0 phase of the cell cycle.

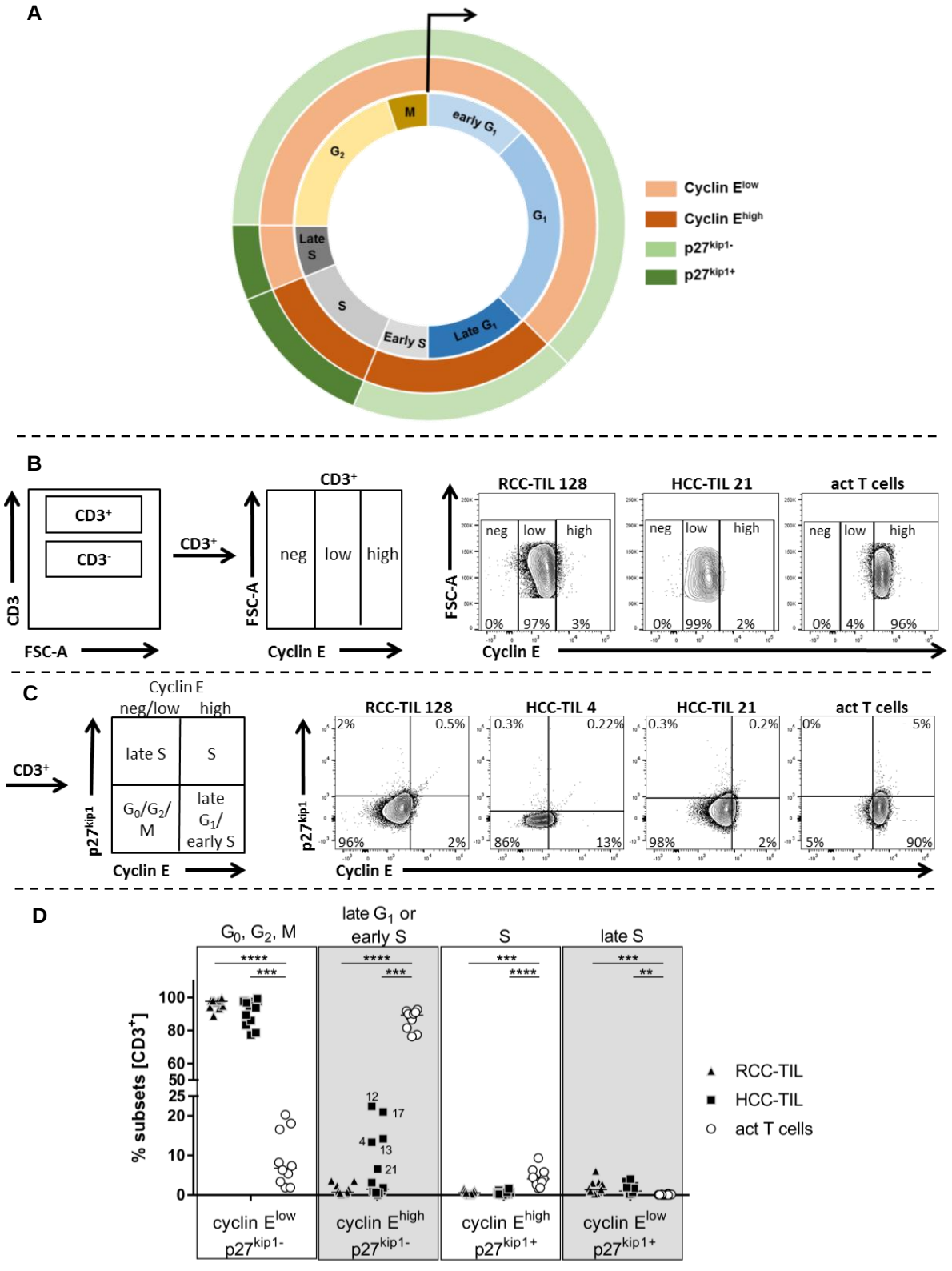

Figure 14: Cell cycle analysis of activated T cells, RCC-TIL and HCC-TIL
Cell suspensions of RCC and HCC tissues and activated T cells were thawed, stained for cyclin E and $p27^{kip1}$ (table 17, see p. 72) and analyzed by flow cytometry. A: The arrow indicates the starting point of the cell cycle and the inner rim denominates the different phases of the cell cycle. Cyclin E levels are indicated in the middle circles. Light brown color corresponds to low levels and dark brown color indicates high levels. The outer rim describes expression of $p27^{kip1}$, $p27^{kip1}$ negative phases are encoded by light green and $p27^{kip1}$ positivity is depicted by dark green. B: Gating strategy and exemplary dot plots to determine frequencies of cyclin E. After gating on $CD3^+$ T cells, cyclin E negative (neg), low and high intensities were distinguished in activated T cells (act T cells), RCC-TIL and HCC-TIL. Cyclin E negative T cells did not exist. Borders were set based on FMO

(fluorescence minus one) controls for cyclin E. C: Gating strategy and exemplary dot plots for RCC-TIL, HCC-TIL and activated T cells (act T cells). Because cyclin E negative cells did not exist, the gate divides cyclin E low and cyclin E high intensities. HCC 4 and HCC 21 are representative patients that have high (HCC 4) and low (HCC 21) frequencies of $p27^{kip1-}$cyclin E^{high} subsets. Borders may vary between samples due to experimental settings. Comparability between experiments was guaranteed by the use of FMO controls for $p27^{kip1}$ and cyclin E to set the borders. C: Graph summarizes the different phases of the cell cycle of RCC-TIL, HCC-TIL and activated T cells. Cell cycle phases are addressed by combinations of cyclin $E^{low/high}$ and $p27^{kip1}$ negative ($^-$) or positive ($^+$). The percentages of each marker combination within preselected $CD3^+$ T cells are presented. Each symbol corresponds to one TIL or sample of activated T cells, significance was determined by Kruskal-Wallis test and Dunn´s Post-hoc comparisons in one group (*p<0.05; **p<0.01; ***p<0.001; ****p<0.0001). Only significant differences between samples are indicated and small numbers indicate patient-IDs.

7.4 The AKT-pathway in TIL

Protein kinase B (PKB, aka AKT) is a serine and threonine kinase with multifunctional downstream signaling nodes like FoxO1 (forkhead box protein 1) and mTORC1 (mammalian target of rapamycin, complex 1). AKT also mediates cytokine production via NF-κB activation and initiates cell cycle progression by suppression of CDK inhibitor $p27^{kip1}$ (20,24,25). Furthermore, cross-talks of AKT- and MAPK-pathway exist by which phosphorylation of AKT can suppress phosphorylation of MAP kinase ERK (20) resulting in the inhibition of T cell degranulation of T cells and lower cytokine production. The impacts of AKT on cell cycle progression and cross-talk to MAPK pathway are visualized in figure 15.

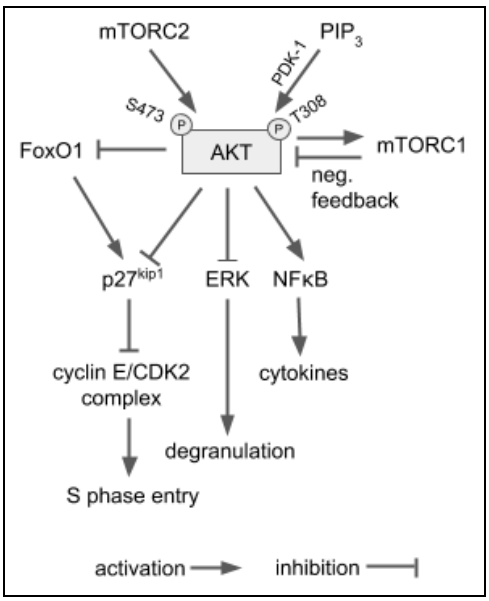

Figure 15: Impact of AKT on cell cycle progression and cross-talk to ERK signaling
AKT: protein kinase B, mTOR: mammalian target of rapamycin (C1: complex 1; C2: complex 2), PDK-1: phosphoinositide-dependent kinase-1, PIP_3: phosphatidylinositol-(3,4,5)-triphosphate, FoxO1: forkhead box protein 1, ERK: extracellular-signal regulated kinase. P: phosphate; S: serine, T: threonine

The AKT-pathway was analyzed in RCC-TIL and HCC-TIL and it was asked whether an impaired phosphorylation state of AKT might relate to the non-proliferative state of TIL. The staining combination was shown above (table 17, see p.72).

7.4.1 The AKT-pathway is poorly active in TIL

First, each of the four markers connected to the AKT-pathway was analyzed individually and frequencies of pAKT(S473), $p27^{kip1}$, cyclin E and pERK(T202/Y204) within gated $CD3^+$ T cells were determined for RCC-TIL, HCC-TIL and activated T cells. Exemplary dot plots are shown in figure 16.

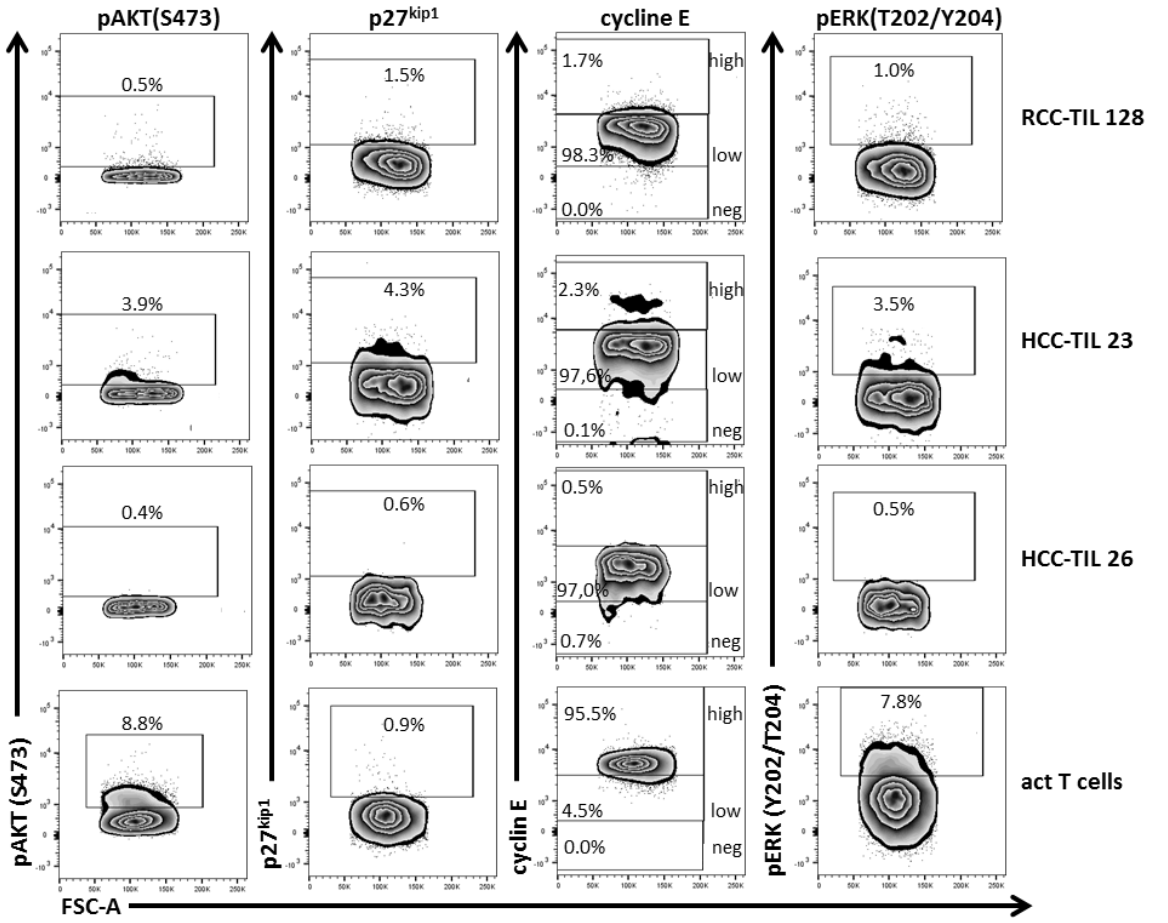

Figure 16: Exemplary dot plots to determine frequencies of proteins related to AKT-pathway in activated T cells and in $CD3^+$ RCC-TIL and HCC-TIL
Tissue suspensions and activated T cells (act T cells) were stained for proteins related to AKT-pathway (table 17, see p. 72) and analyzed by flow cytometry. Exemplary dot plots to determine frequencies of pAKT(S473), $p27^{kip1}$, cyclin E and pERK(Y202/T204) are shown. Borders were set based on FMO (fluorescence minus one) controls separately in each experiment.

It was observed (figure 17 A), that TIL had low frequency of $pAKT(S473)^+$ T cells (RCC-TIL: median 1%; range: 0.5% – 12%; HCC-TIL: median 4%; range: 1% – 9%) compared with activated T cells (median 8%; range: 5% – 13%). This difference was significant for RCC-TIL whereas HCC-TIL were split into two groups: TIL of five HCC patients had higher frequencies (highest value: 10%) of pAKT(S473) similar to activated T cells while the other nine patients had TIL with very low frequencies of $pAKT(S473)^+$ T cells (highest value: 4%) similar to RCC-TIL.

Frequencies of $p27^{kip1}$ were lower in $CD3^+$ RCC-TIL (median 1%; range: 1% – 8%) and HCC-TIL (median 2%; range: 0% – 4%) compared with activated T cells (median 7%; range: 3% – 12%) without reaching significance. As mentioned before (see p. 71), T cells could be distinguished based on cyclin E^{low} and cyclin E^{high} whereas cyclin E negative T cells did not exist. RCC-TIL and HCC-TIL were found to be mostly cyclin E^{low} (RCC-TIL: median 96%; range: 70% – 98%; HCC-TIL: median 88%; range: 77% – 97%), while activated T cells were cyclin E^{high} (median 94%; range: 82% – 98%). Again, HCC-TIL split into two groups: five TIL of HCC patients had T cells being cyclin E^{high} (highest value: 21 %) and nine TIL had comparable values of cyclin E^{high} as RCC-TIL (highest value: 3%). Frequencies of pERK(T202/Y204)$^+$ T cells were significantly lower in RCC-TIL (median 2%; range: 1% – 4%) and HCC-TIL (median 3%; range: 0% – 4%) than in activated T cells (median 7%; range: 3% – 14%).

The expression of the markers pAKT(S473), $p27^{kip1}$, cyclin E and pERK(T202/Y204) was analyzed by the mean fluorescence intensity (MFI) of each protein. Similar to observed lower frequencies of T cells, also MFI values of each protein were significantly lower in TIL compared with activated T cells (figure 17 B).

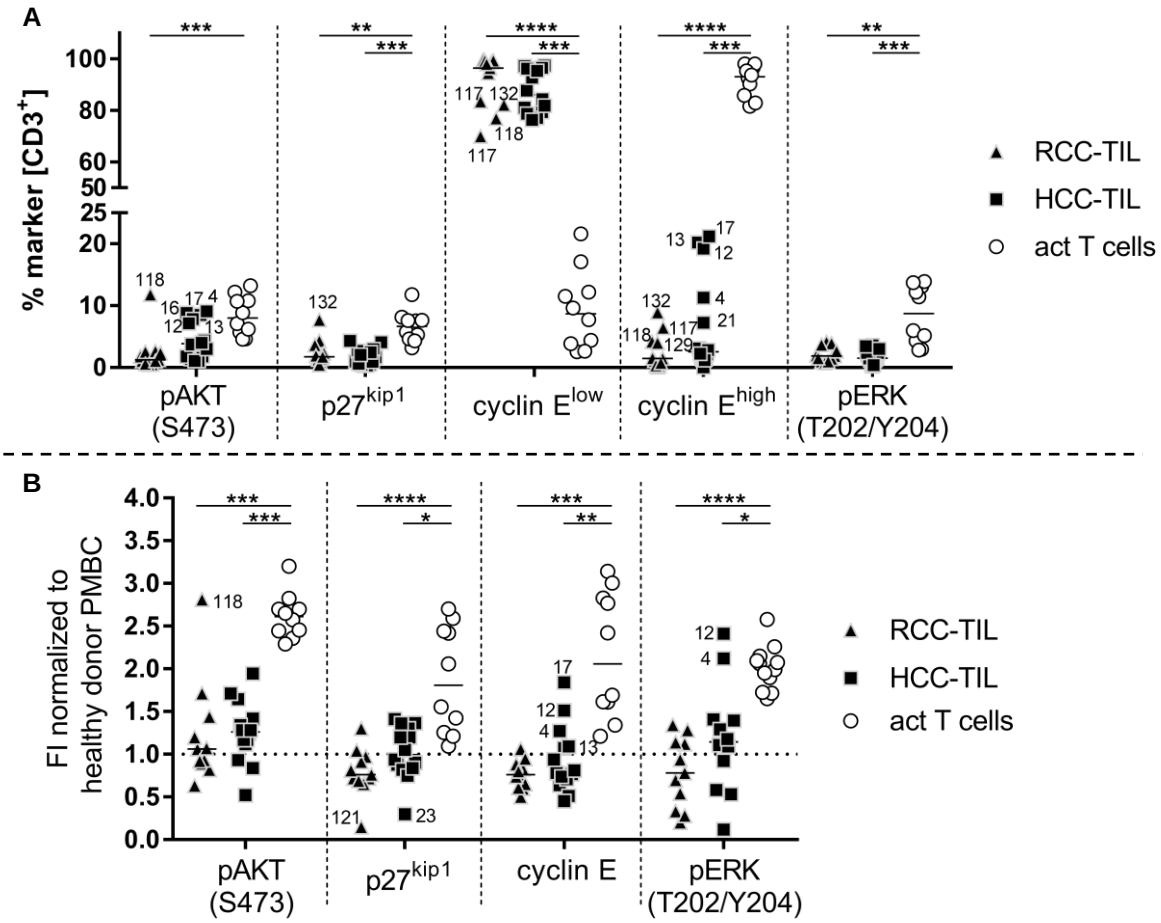

Figure 17: Cell frequencies and expression levels of proteins related to AKT-pathway in activated T cells and in gated CD3$^+$ RCC-TIL and HCC-TIL
Tissue suspensions of and activated T cells (act T cells) were stained for proteins related to AKT-pathway (table 17, see p. 72) and analyzed by flow cytometry. A: Frequencies of markers related to the AKT-pathway among gated CD3$^+$ T cells. C: Normalized fluorescence intensities (FI) of markers. Because mean fluorescence intensities (MFI) depended on the settings of the flow cytometer (LSR II, BD) and settings varied between experiments, the MFI values of each marker in different experiments were normalized to the MFI of one HD-PBMC that was included in each experiment as control. Dotted horizontal line indicates values of normalization control. Each symbol represents one sample and vertical dotted lines separate different markers. Significance was determined within one marker by Kruskal-Wallis test and Dunn´s Post-hoc comparisons (*p<0.05; **p<0.01; *** p<0.001; ****p<0.0001). Only significant differences are indicated. Small numbers indicate patient-IDs.

7.4.2 The influence of AKT on cell cycle progression in TIL

7.4.2.1 pAKT(S473) suppresses p27^{kip1} in TIL

RCC-TIL and HCC-TIL were found to exhibit low levels of pAKT(S473). Since the AKT-pathway is known to support the cell cycle by phosphorylation and inactivation of p27^{kip1} (24,25), it was of interest to determine if low phosphorylation levels of AKT might be connected to the non-proliferative state of TIL. To define a relationship between pAKT and the cell cycle inhibitory protein p27^{kip1} on a single cell level, dot plots were analyzed and frequencies of each combination of pAKT(S473) and p27^{kip1} were calculated as

percentages of $CD3^+$ T cells (figure 18). A clear association of pAKT(S473) and $p27^{kip1}$ was observed, since T cells double-positive for pAKT(S473) and $p27^{kip1}$ were not detected and all $pAKT(S473)^+$ T cells were found to be $p27^{kip1}$ negative, consistent with the knowledge that active (phosphorylated) AKT(S473) inhibits $p27^{kip1}$ (24,25). The frequencies of $pAKT(S473)^+p27^{kip1-}$ T cells were highest in activated T cells (median 7%; range: 3% - 14%) and significantly lower in HCC-TIL (median 3%; range: 0% – 7%) and in RCC-TIL (median 2%; range: 0% – 7%). Frequencies of $pAKT(S473)^-p27^{kip1+}$ T cells were also highest in activated T cells (median 4%, range: 2% – 7%) and low in RCC-TIL (median: 2%; range: 0% – 7%) and in HCC-TIL (median 2%; range: 2% - 6%). The main $CD3^+$ T cell population in RCC-TIL and HCC-TIL as well as in activated T cells was double negative for pAKT(S473) and $p27^{kip1}$ (activated T cells: median 85 %; range: 83% – 92%; RCC-TIL: median 97%; range: 95% – 98%, HCC-TIL: median 97%; range: 90% – 99%).

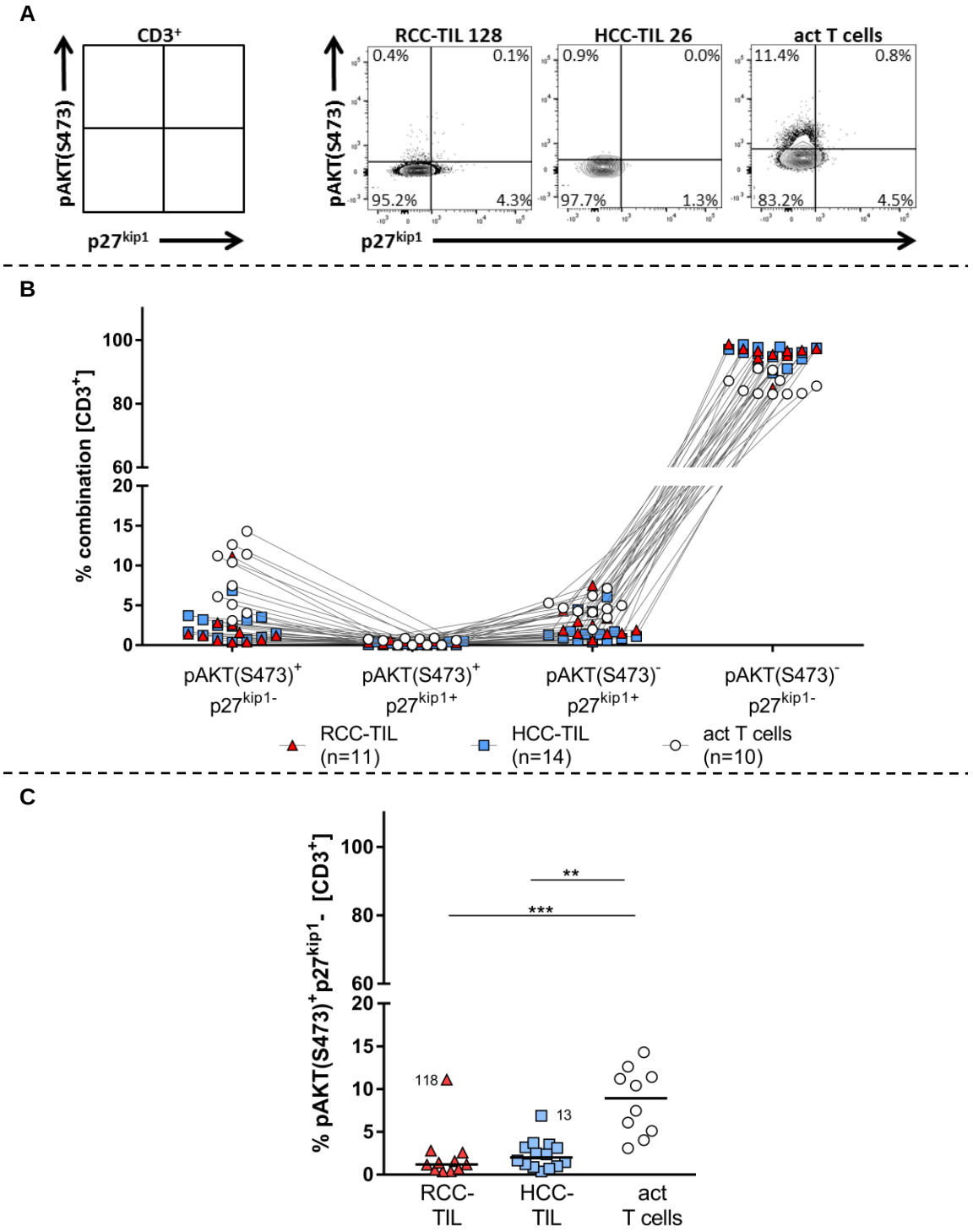

Figure 18: Combinations of pAKT(S473) and p27^{kip1} in activated T cells, CD3$^+$ RCC-TIL and HCC-TIL
Tissue suspensions and activated T cells were stained for flow cytometry (table 17, see p. 72). Combinations of pAKT(S473) and p27^{kip1} were analyzed within gated CD3$^+$ T cells. A: Gating strategy and exemplary dot plots of RCC-TIL and HCC-TIL and activated T cell (act T cells). B: Summary of calculated frequencies of cells with indicated marker combination within gated CD3$^+$ T cells of RCC-TIL, HCC-TIL and activated T cells. Each symbol represents one TIL or one sample of activated T cells, lines connect combinations of pAKT(S473) and p27^{kip1} of the same individual. C: The subset pAKT(S473)$^+$p27^{kip1-} is visualized separately to illustrate significant differences between activated T cells (act T cells) and RCC-TIL or HCC-TIL respectively. Each symbol represents one TIL or sample of activated T cells, horizontal lines indicate median of one group. Significance was determined within pAKT(S473)$^+$p27^{kip1-} by Kruskal-Wallis test and Dunn´s Post-hoc comparisons (*p<0.05; **p<0.01; ***p<0.001; ****p<0.0001). Only significance between samples is indicated. Numbers are patient-IDs.

7.4.2.2 High percentages of cyclin E are independent of AKT phosphorylation

Activation of the AKT-pathway is known to positively drive cell cycle progression, amongst other by inhibiting $p27^{kip1}$ leading to upregulation of cyclin E (24,25). To determine the interrelationship of pAKT(S473) and cyclin E on a single cell level, both markers were displayed in dot plots and percentages of cells expressing either one marker alone or a combination of both markers within gated $CD3^+$ T cells were calculated (figure 19 A and B).

It was observed, that the majority of activated T cells were cyclin E^{high} independent of pAKT(S473) expression, illustrating that there is no strict association between pAKT(S473) and high cyclin E. Different to activated T cells, the predominant population in $CD3^+$ RCC-TIL and HCC-TIL was negative for pAKT and was cyclin E^{low}, suggesting that in TIL the AKT pathway is poorly activated and consequently most T cells are cyclin E^{low}. Interestingly, higher frequencies of $pAKT(S473)^+$cyclin E^{low} T cells were found in TIL compared with activated T cells (figure 19 C), indicating that the phosphorylation the AKT-pathway in TIL was not communicated to cyclin E (figure 19 C). Four HCC-TIL that were previously described to have higher frequencies of cyclin E high compared with the main cohort (see p. 76) also had T cells that were $pAKT(S473)^-$cyclin E^{high} resembling activated T cells. These $CD3^+$ HCC-TIL might have experienced activation of the AKT-pathway. However, this population was very rare (below 5%) in all RCC-TIL, demonstrating that RCC-TIL were excluded from AKT activation.

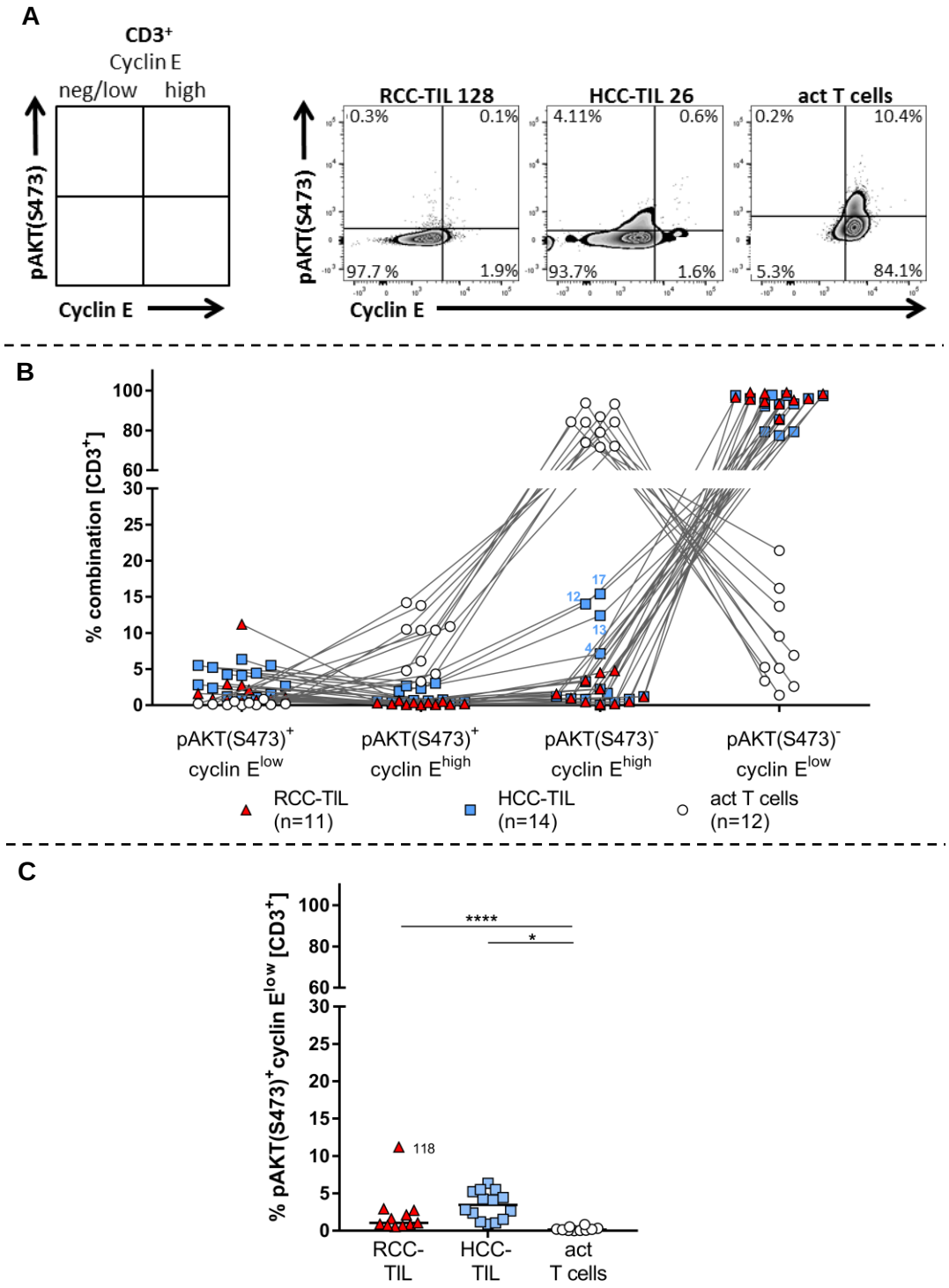

Figure 19: Association between pAKT(S473) and cyclin E in activated T cells, RCC-TIL and HCC-TIL
Tissue suspensions and activated T cells were stained for flow cytometry (table 17, see p. 72). Combinations of pAKT(S473) and cyclin E were analyzed within gated $CD3^+$ T cells. A: Gating strategy with exemplary dot plots of RCC-TIL, HCC-TIL and activated T cell (act T cells). Cyclin E negative (neg) subsets did not exist and borders separate between cyclin E^{low} and cyclin E^{high} subsets. B: Summary of calculated frequencies of cells with indicated marker combination in pregated $CD3^+$ T cells of RCC-TIL, HCC-TIL and activated T cells. Each symbol represents one TIL or one sample of activated T cells, lines connect combinations of pAKT(S473) and cyclin E of the same individual. C: The subset pAKT(S473)$^+$cyclin E^{low} is visualized separately to illustrate significant differences between activated T cells and TIL. Each symbol represents one TIL or sample of activated T cells, horizontal lines indicate median of one group. Significance was determined in the pAKT(S473)$^+$cyclin E^{low} subset by Kruskal-Wallis test and Dunn´s Post-hoc comparisons (*p<0.05; **p<0.01; ***p<0.001; ****p<0.0001). Only significance between samples is indicated. Small numbers indicate patient-IDs.

7.4.3 Cross-talk of AKT- and MAPK-pathway

The literature indicates cross-talks of AKT- and MAPK-pathway (20) where pAKT inhibits pERK by phosphorylation of c-RAF. Additionally, pERK can directly inhibit pAKT, thereby inhibiting the other pathway´s ability to signal (31).

7.4.3.1 Positivity of pAKT excludes positivity of pERK in TIL

To elucidate the interrelationship between AKT and ERK pathway, the phosphorylation state of the two markers was displayed in dot plots and the marker combinations were calculated in activated T cells, RCC-TIL and HCC-TIL (figure 20 A and B).

In HCC-TIL (figure 20 C), some T cells with pAKT(S473) but without pERK(Y202/T204) were detected ($pAKT(S473)^{+}pERK(Y202/T204)^{-}$, median 4%; range: 2% – 8%) similar to activated T cells (median 3%; range: 2% – 7%). These cells were fewer in RCC-TIL (median 1%; range: 0% – 4%; except of RCC-TIL 118; 11%). A small fraction (median 4%; range: 0% – 8%) of activated T cells was positive for both pAKT(S473) and pERK(Y202/T204). On the contrary, those T cells were not observed in RCC-TIL and HCC-TIL. Taken together, $CD3^{+}$ RCC-TIL were strongly depressed in both pAKT(S473) and pERK(Y202/T204), while HCC-TIL have retained some level of AKT-pathway activation.

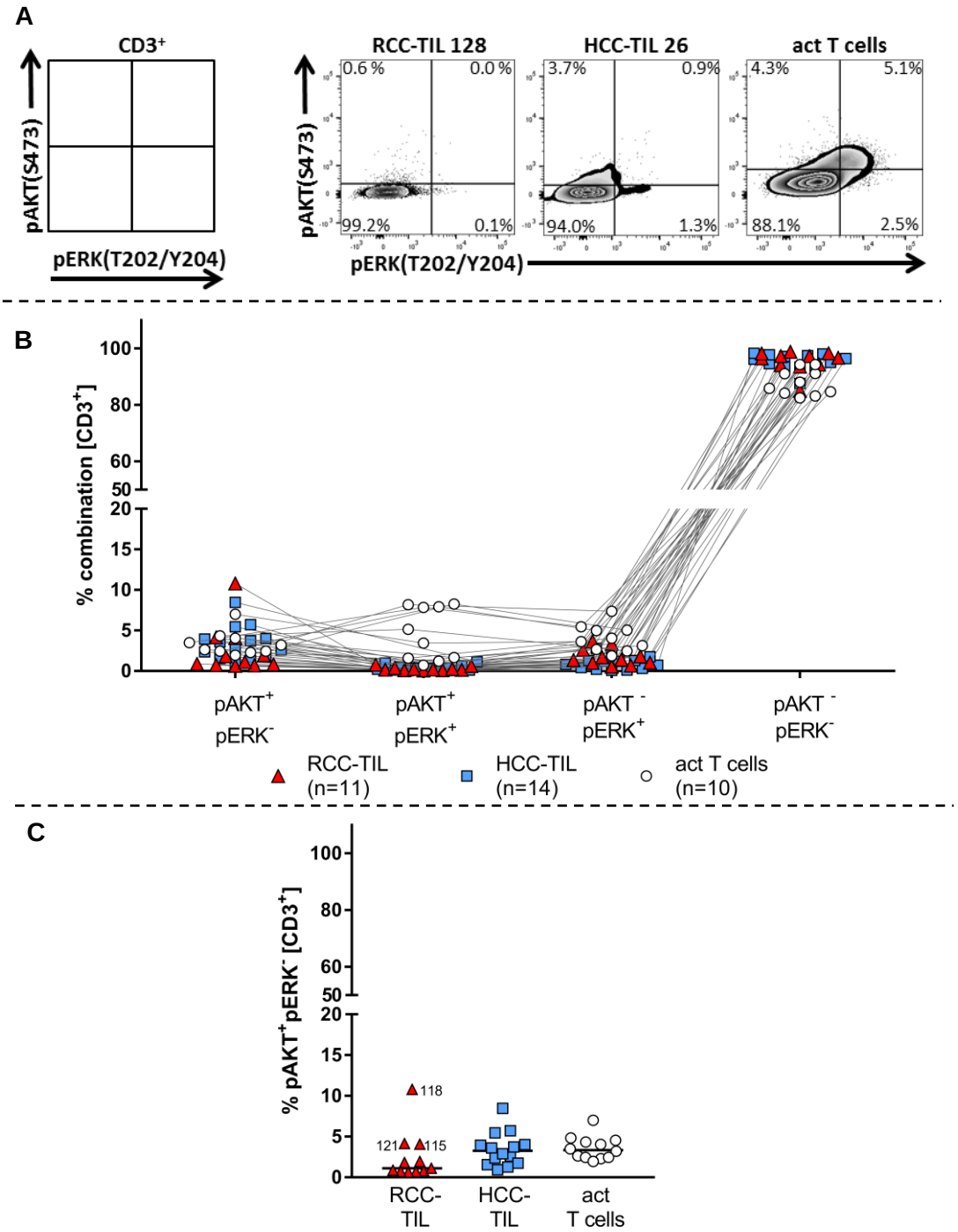

Figure 20: Association between pAKT(S473) and pERK(T202/Y204) in activated T cells, RCC-TIL and HCC-TIL

Tissue suspensions and activated T cells were stained for flow cytometry (table 17, see p. 72). Combinations of pAKT(S473) and pERK(T202/Y204) were analyzed within gated $CD3^+$ T cells. A: Gating strategy with exemplary dot plots of RCC-TIL, HCC-TIL and activated T cell (act T cells). B: Summary of calculated frequencies of cells with indicated marker combination within gated $CD3^+$ T cells of RCC-TIL, HCC-TIL and activated T cells. Each symbol represents one TIL or one sample of activated T cells and lines connect combinations of pAKT(S473) and pERK(T202/Y204) of the same individual. C: The subset $pAKT(S473)^+pERK(T202/Y204)^-$ is visualized separately to address differences between activated T cells and TIL. Kruskal-Wallis test did not detect significant differences between act T cells and TIL. Each symbol represents one TIL or sample of activated T cells, horizontal lines indicate median of one group. Numbers are patient-IDs.

7.4.3.2 Positivity of pERK predicts cell cycle state of TIL

AKT and ERK are activated through different upstream signals: the AKT-pathway and subsequent cell cycle progression is activated by co-stimulation (17), while ERK and downstream degranulation of T cells is induced by TCR triggering through pMHC binding (10). Analyzing combinations of pERK(T202/Y204), pAKT(S473) and $p27^{kip1}$ at a single cell level, it was observed that pERK(Y202/T204)$^+$ T cells of TIL were found in different pAKT/p27kip1 T cell subsets (figure 21). In activated T cells, the pERK(Y202/T204)$^+$ T cells were mainly detected in the pAKT(S473)$^+$p27kip1$^-$ subset in activated T cells (median 43%; range: 12% – 73%), indicating that pERK(T202/Y204) positivity is related to cell cycle progression in activated T cells. On the contrary, pERK(T202/Y204)$^+$ T cells of RCC-TIL and HCC-TIL were mainly present in pAKT(S473)$^-$p27kip1$^+$ subset (RCC-TIL median 13%; range: 1% – 48%; HCC-TIL median 12%; range: 0% – 62%), indicating that in TIL pERK(T202/Y204) positivity is related to cell cycle arrest (positivity of cell cycle inhibitor $p27^{kip1}$).

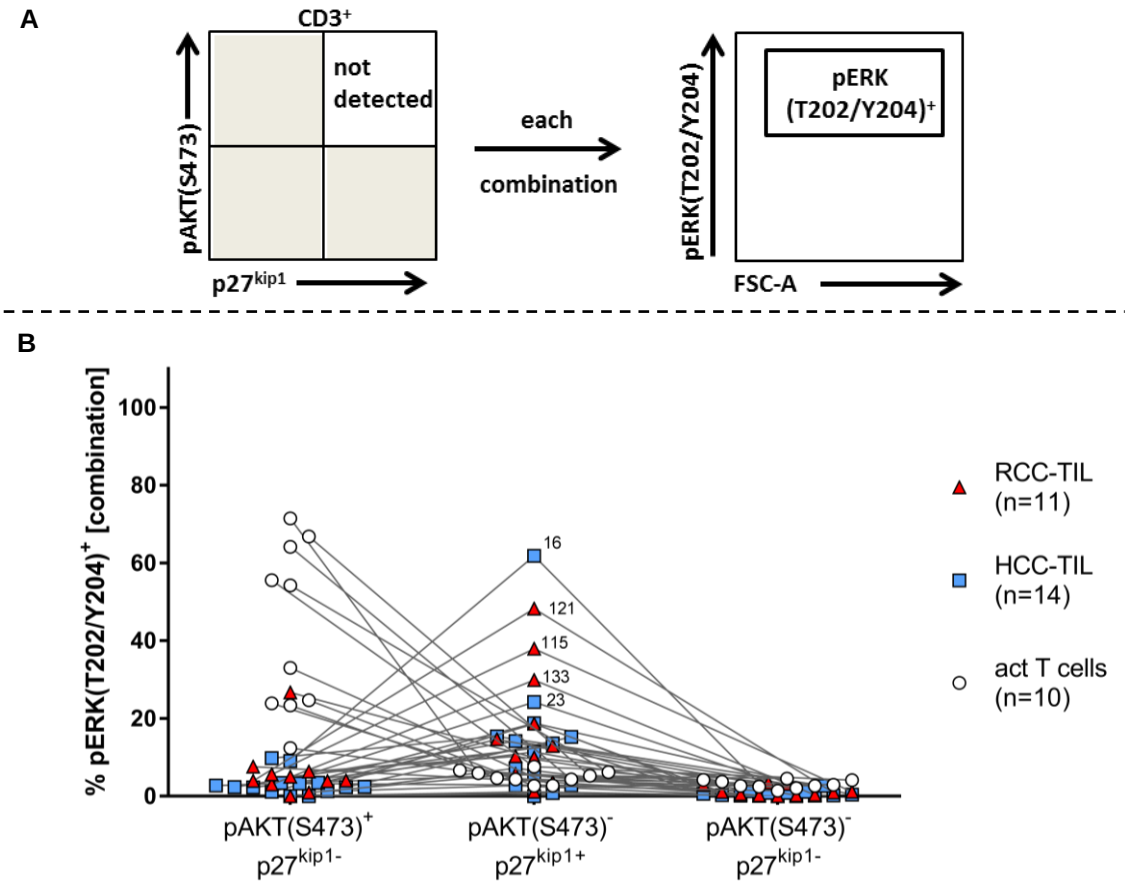

Figure 21: Relationship of pERK, pAKT and $p27^{kip1}$ in activated T cells, RCC-TIL and HCC-TIL
Tissue suspensions and activated T cells were stained for flow cytometry (table 17, see p. 72). Interrelations of pERK(T202/Y204), pAKT(S473) and $p27^{kip1}$ were analyzed within gated $CD3^+$ T cells. A: Gating strategy to determine $pERK^+$ T cells within combinations of pAKT (S473) and $p27^{kip1}$. B: Summary of calculated frequencies $pERK^+$ T cells within indicated marker combinations in gated $CD3^+$ T cells of RCC-TIL, HCC-TIL and activated T cells (act T cells). Each symbol represents one TIL or one sample of activated T cells and lines connect percentages of pERK in different combinations of pAKT(S473) and $p27^{kip1}$ of the same individual. Numbers are patient-IDs.

To further elucidate the relation between pERK(T202/Y204) positivity and cell cycle state of TIL, the phases of the cell cycle were determined at a single cell level by combinations of $p27^{kip1}$ and cyclin E (see p. 71) in preselected $pERK(T202/Y204)^-$ or $pERK(T202/Y204)^+$ subgroups of $CD3^+$ RCC-TIL, HCC-TIL and activated T cells (figure 22). Activated T cells were mainly in the late G1/early S subgroup (figure 22 C) and this was independent of pERK(T202/Y204).

In TIL, there was a difference between T cells with or without pERK(T202/Y204): $pERK(T202/Y204)^+$ TIL had reduced frequencies in the G0/G1/M group (figure 22 D) and significantly higher percentages of T cells in the late G1/early S (figure 22 C), S (figure 22 E) or late S (figure 22 F) phase compared with $pERK(T202/Y204)^-$ T cells.

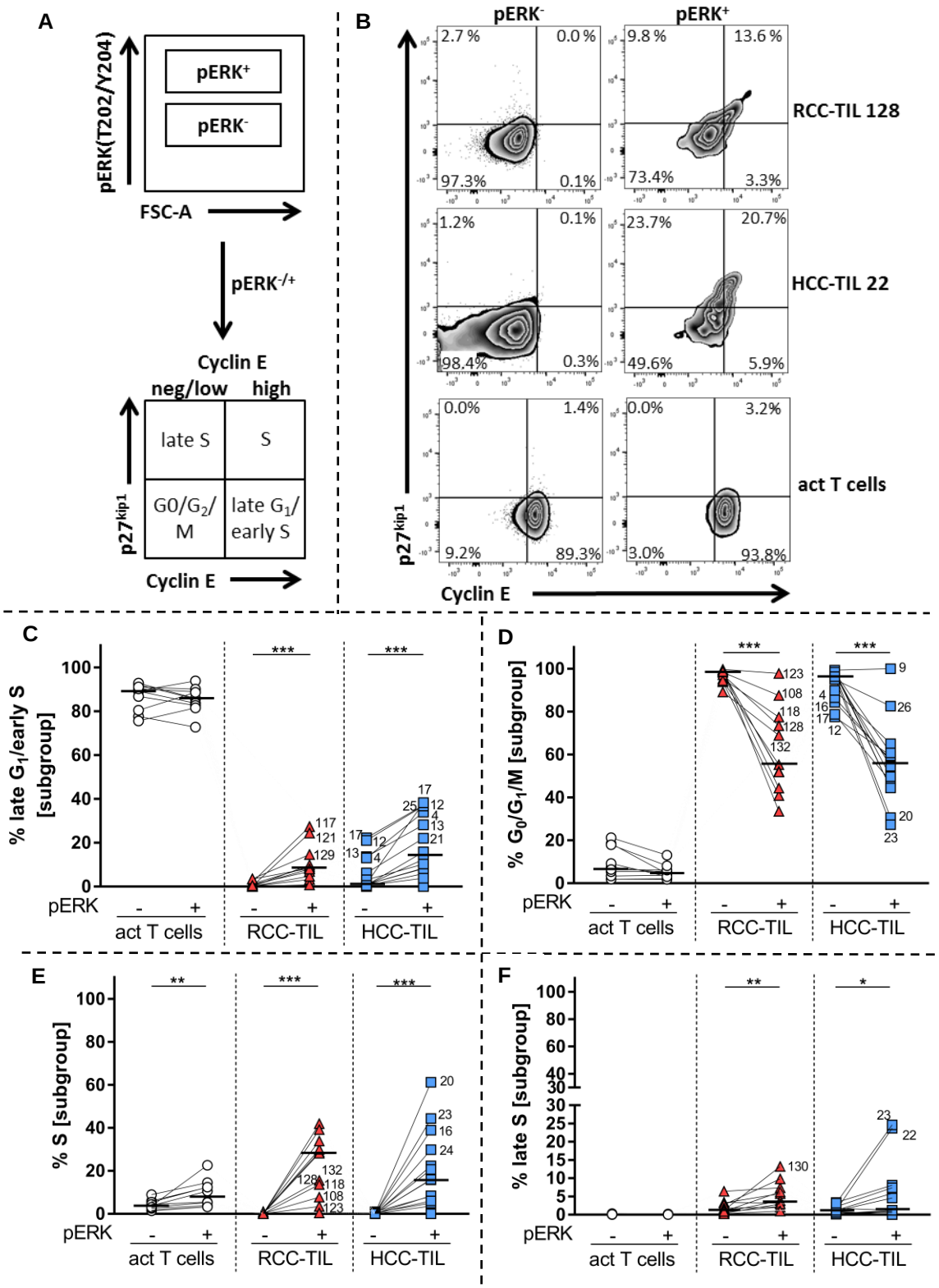

Figure 22: Relation between pERK and cell cycle of activated T cells, RCC-TIL and HCC-TIL
Tissue suspensions and activated T cells (act T cells) were stained for flow cytometry. Interrelations of pERK(T202/Y204), $p27^{kip1}$ and cyclin E were addressed. A: Gating strategy: Combinations of $p27^{kip1}$ and cyclin E were determined within $pERK^+$ and $pERK^-$ subgroups of preselected $CD3^+$ T cells. Phases of the cell cycle were related to $p27^{kip1}$ and cyclin E combinations. B: Exemplary dot plots of RCC-TIL, HCC-TIL and activated T cells for combinations of $p27^{kip1}$ and cyclin E (different cell cycle states) in $pERK^{-/+}$ subsets. C-F: Summary figures of calculated percentages of T cells at different cell cycle states in $pERK^{-/+}$ subsets. Each symbol represents one sample, numbers are patient-IDs and horizontal lines indicate the median of one group. Significance was determined between $pERK^-$ and $pERK^+$ subsets by Wilcoxon matched pairs signed-rank test (*p<0.05; **p<0.01; ***p<0.001; ****p<0.0001). Only significance between groups is indicated.

7.5 The mTOR-pathway in TIL

Mammalian target of rapamycin (mTOR) is a central regulator of cell metabolism, growth and proliferation (29,30,80). There are two protein complexes of mTOR with different functions: mTORC2 phosphorylates AKT at S473 and mTORC1 can be activated by AKT (20) and ERK (31). Its catalytic subunit raptor (regulatory-associated protein of mTOR) allows phosphorylation of p70 ribosomal protein kinase S6 (p70S6) which leads to phosphorylation of ribosomal protein S6 (rpS6) that subsequently induces gene translation (29).

mTORC1 regulates $CD8^+$ T cell memory generation and high mTORC1 activity is associated with poor effector to memory transition (80). Furthermore, mTORC1 promotes effector differentiation of $CD8^+$ T cells by gene regulation of cytotoxic effector molecules perforin, granzyme B or IFN-γ (30). A brief summary of mTOR activation and its downstream effects in $CD8^+$ T cells are summarized in figure 23.

In $CD8^+$ RCC-TIL, levels of perforin have been reported to be low compared with r-NIL (40). In this thesis it was further elucidated if low perforin levels also exist in HCC-TIL and might be traced back to impaired mTOR-pathway.

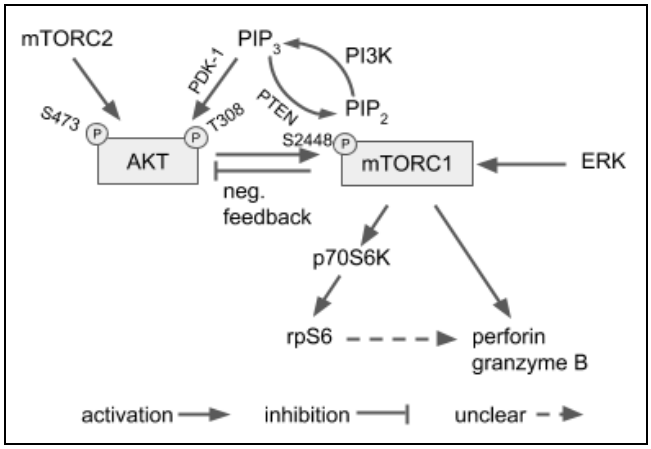

Figure 23: mTOR-pathway in $CD8^+$ T cells
mTOR: mammalian target of rapamycin (C1: complex 1; C2: complex 2), PDK-1: phosphoinositide-dependent kinase-1, PIP_3: phosphatidylinositol-(3,4,5)-triphosphate, PIP_2: phosphatidylinositol-(4,5)-bisphosphate, PI3K: phosphoinositide-3 kinase; PTEN: phosphatase and tensin homolog, AKT: protein kinase B, ERK: extracellular-signal regulated kinase, p70S6K: p70 ribosomal protein kinase, rpS6: ribosomal protein S6, Arrows indicate activation and dashes visualize inhibition. P: phosphate; S: serin, T: threonine

The staining combination for addressing the mTOR-pathway is shown in table 18.

Table 18: Staining combination to address the mTOR-pathway (staining combination 3)

Target/epitope	Fluorochrome	Cell subset/function
Viability: LIVE/DEAD™ Fixable Blue Dead Cell Stain	Indo-1-violet	staining of dead cells
CD45	Pe-Cy7	leukocytes
CD3	PerCp-Cy™5.5	T cells
pmTOR(S2448)	APC	mTOR phosphorylated at S2448
prpS6 (S244)	PE	ribosomal protein S6 phosphorylated at S244 (downstream target of pmTOR)
perforin	FITC	cytolytic molecule

7.5.1 The mTOR-pathway is impaired in TIL

First, each of the markers was analyzed individually and frequencies of pmTOR(S2448), prpS6(S244) and perforin within gated $CD3^+$ T cells were determined for RCC-TIL, HCC-TIL and activated T cells (figure 24 A and B, see p. 90). In addition, the expression level (addressed by mean fluorescence intensity) of each protein in the gated $CD3^+$ population was determined (figure 24 C).

All activated T cells were pmTOR(S2448)$^+$ (median frequency 100%), while frequencies of pmTOR(S2448) were lower in RCC-TIL (median 83%; range: 63% – 96%), though not significantly. Two cohorts were found for $CD3^+$ HCC-TIL, one with high (range: 84% - 100%, eight patients) the other with low (range: 26% – 75%, five patients) frequencies of pmTOR(S2448). In contrast, all TIL had significantly lower frequencies of prpS6(S244)$^+$ T cells (RCC-TIL: range 0% - 80%; HCC-TIL: 0% - 90%), while act T cells were nearly all positive for prpS6(S244) suggesting that the activation of mTORC1 downstream target rpS6 is interrupted in most TIL. Frequencies of perforin$^+$ T cells were very low in RCC-TIL, somewhat higher in $CD3^+$ HCC-TIL and highest in act T cells.

Analysis of the mean fluorescence intensities (MFI) revealed that pmTOR(S2448), prpS6(S244) and perforin were significantly lower expressed in $CD3^+$ RCC-TIL and HCC-TIL compared with activated T cells.

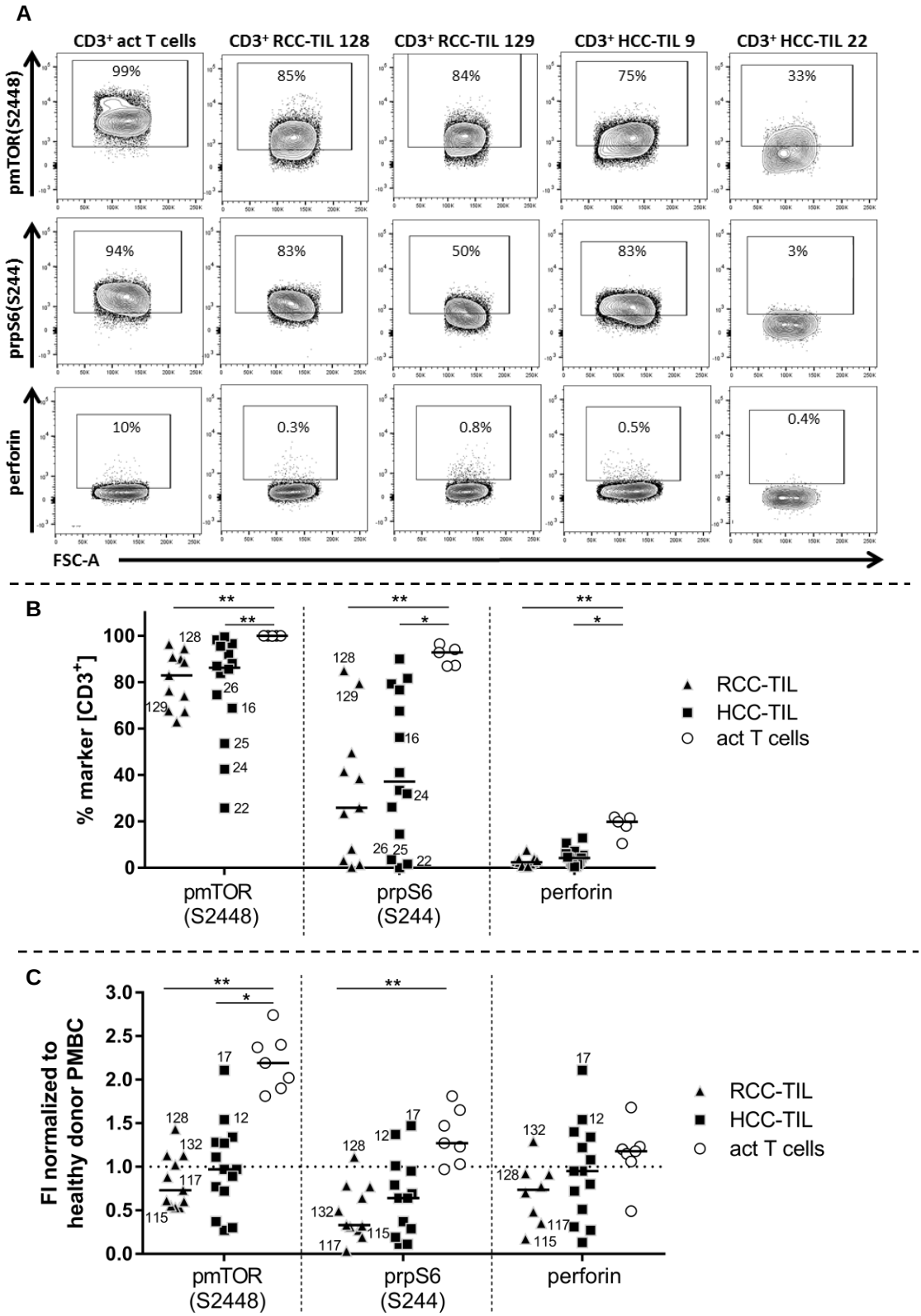

Figure 24: Cell frequencies and expression levels of proteins related to mTOR-pathway in activated T cells, CD3$^+$ RCC-TIL and HCC-TIL

Tissue suspensions and activated T cells stained for flow cytometry. A: Exemplary dot plots to determine frequencies of pmTOR(S2448), prpS6(S244) and perforin. Borders were set based on FMO (fluorescence minus one) controls separately in each experiment. B: Frequencies of markers related to the mTOR-pathway among gated CD3$^+$ T cells. C: Normalized mean fluorescence intensities (FI) of markers. Horizontal dotted line indicates values of normalization control. Each symbol represents one sample, vertical dotted lines separate different markers. Significance was determined within one marker by Kruskal-Wallis test and Dunn´s Post-hoc comparisons (*p<0.05; **p<0.01; *** p<0.001; ****p<0.0001). Only significant differences are indicated.

7.5.2 pmTOR$^+$prpS6$^+$ divides TIL into two groups

Activation of mTORC1 leads to downstream phosphorylation of rpS6(S244) which then induces translational gene regulation (29). To examine if the mTOR-signaling in TIL is activated, co-expression of pmTOR(S4428) and prpS6(S244) was addressed on a single cell level. Within gated CD3$^+$ T cells (figure 25), activated T cells were mainly double positive for pmTOR(S2448) and prpS6(S244) (median 93%; range: 87% – 97%). In CD3$^+$ RCC-TIL and HCC-TIL, two groups of patients were identified. Five patients in RCC-TIL and seven HCC-TIL had high frequencies of pmTOR(S2448)$^+$prpS6(S244)$^+$ T cells (RCC-TIL: 39% - 83% and HCC-TIL: 54% – 91%). These TIL had low frequencies of pmTOR(S2448)$^+$prpS6(S244)$^-$ T cells (RCC-TIL: 20% – 43% and HCC-TIL: 8% – 32%). The second group of patients showed low frequencies of T cells being pmTOR(S2448)$^+$prpS6(S244)$^+$ T cells (RCC-TIL: 1% - 21% and HCC-TIL: 1% – 22%) and high levels of pmTOR(S2448)$^+$prpS6(S244)$^-$ (RCC-TIL: 55% – 96%; HCC-TIL: 60% - 80%). The difference between the two groups of TIL with low and high frequencies of pmTOR(S2448)$^+$prpS6(S244)$^+$ was significant ($p<0.001$). In general, the frequencies of pmTOR(S2448)$^+$prpS6(S244)$^-$ were higher in RCC-TIL and HCC-TIL compared with activated T cells indicating an incomplete activation of the mTOR-pathway.

Percentages of T cells double negative for pmTOR(S2448) and prpS6(S244) were also higher in RCC-TIL and HCC-TIL than in activated T cells suggesting that in some TIL the mTOR-pathway was not activated at all. T cells being pmTOR(S2448)$^-$prpS6(S244)$^+$ were largely absent in TIL and in activated T cells as expected since phosphorylation of rpS6 requires mTOR phosphorylation (29).

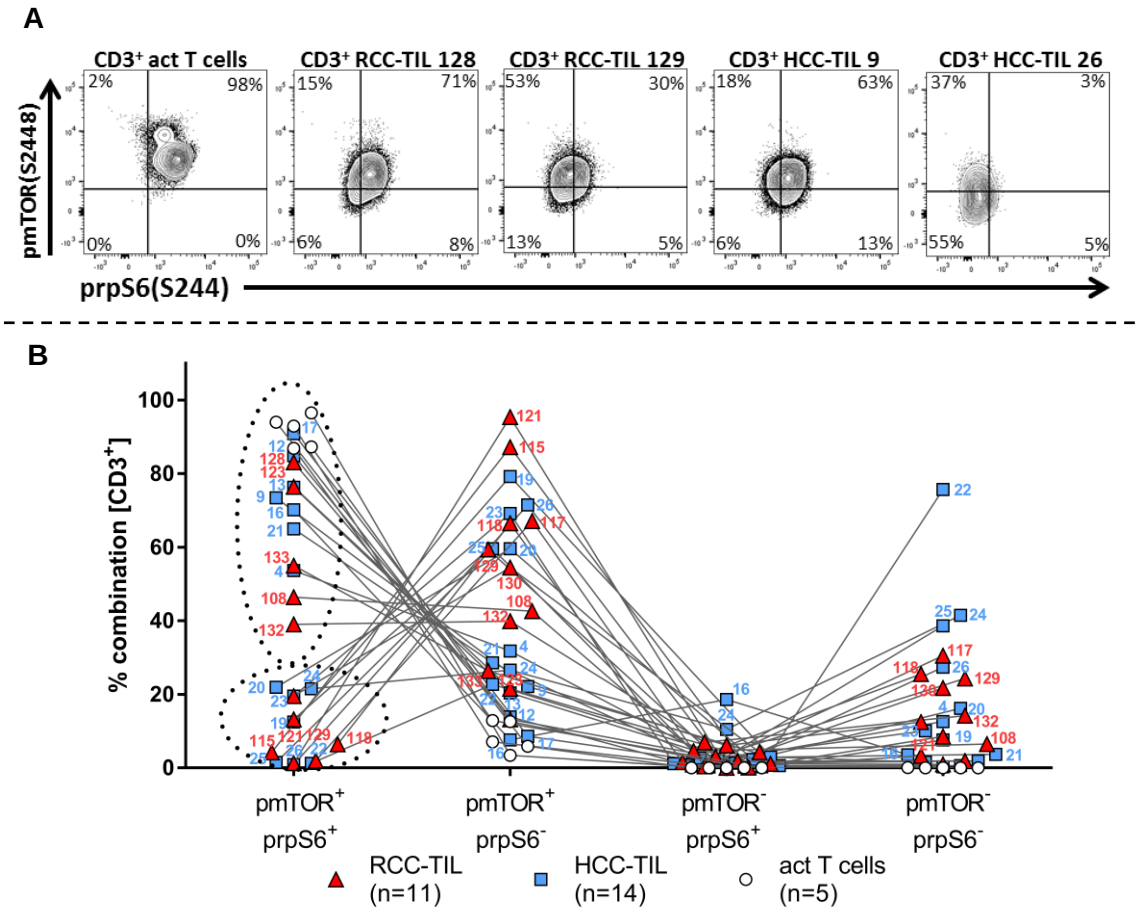

Figure 25: Combinations of pmTOR(S2448), rpS6(S244) in activated T cells, CD3$^+$ RCC-TIL and HCC-TIL

Tissue suspensions and activated T cells were stained for flow cytometry (table 18, see p.89). Combinations of pmTOR(S2448), prpS6(S244) and perforin were analyzed within gated CD3$^+$ T cells. A: Exemplary dot plots of RCC-TIL, HCC-TIL and activated T cell (act T cells). B: Summary of calculated frequencies of cells with indicated marker combination within gated CD3$^+$ T cells of RCC-TIL, HCC-TIL and activated T cells. Dotted circles mark groups of TIL with high and low percentages of pmTOR(S2448)$^+$prpS6(S244)$^+$ T cells. Each symbol represents one TIL or one sample of activated T cells, lines connect combinations of pmTOR(S2448) and prpS6(S244) of the same individual and number indicate patient-IDs (red: RCC-TIL, blue: HCC-TIL).

7.5.3 Phosphorylated mTOR and rpS6 determine perforin positivity in TIL

It has been described that the expression of cytotoxic effector molecules perforin and granzyme B is controlled by mTORC1 signaling (29,30), however, it has remained unclear if phosphorylation of rpS6 is also involved in perforin upregulation. Therefore the relation between pmTOR(S2448), prpS6(S244) and perforin in TIL was evaluated. Exemplary dot plots and corresponding graphs are shown in figure 26.

Examining the dot plots, it was evident that perforin was only seen in pmTOR(S2448)$^+$ or prpS6(S244)$^+$ cells in all samples of TIL or activated T cells indicating a strict dependency of perforin on phosphorylated mTOR or phosphorylated rpS6.

Activated T cells were all pmTOR(S2448)$^{+}$perforin^{-} and CD3^{+} RCC-TIL and HCC-TIL had high percentages of pmTOR(S2448)$^{+}$perforin^{-} T cells (median RCC-TIL 74%, median HCC-TIL 79%). One RCC-TIL (53%) and three HCC-TIL (range: 18% – 52%) had lower percentages compared with the main cohort. Frequencies of pmTOR(S2448)$^{+}$perforin^{+} T cells were comparable low in RCC-TIL (median 1%) and HCC-TIL (median 3%) whereas percentages of pmTOR^{-}perforin^{-} cells were higher in RCC-TIL (median 21%) compared with median frequencies in HCC-TIL of 11%. Interestingly, pmTOR(S2448)$^{-}$ perforin^{+} subsets did neither exist in RCC-TIL nor HCC-TIL nor activated T cells, emphasizing that perforin positivity depends on phosphorylated mTOR.

With regard to combinations of prpS6(S244) and perforin, activated T cells were all prpS6(S244)$^{+}$perforin^{-}, and CD3^{+} RCC-TIL and HCC-TIL covered a wide range of prpS6(S244)$^{+}$perforin^{-} cells. (range RCC-TIL: 0% – 85%, range HCC-TIL: 0% - 87%). Those TIL with high frequency of prpS6(S244)$^{+}$perforin^{-} had correspondingly low frequency of double negative cells for rpS6(S244) and perforin (range RCC-TIL: 15% - 98%, range HCC-TIL: 9% - 99%). Interestingly, prpS6(S244)$^{-}$perforin^{+} cells did neither exist in RCC-TIL nor in HCC-TIL, emphasizing that perforin positivity depends not only on pmTOR(S244) but also on phosphorylated rpS6.

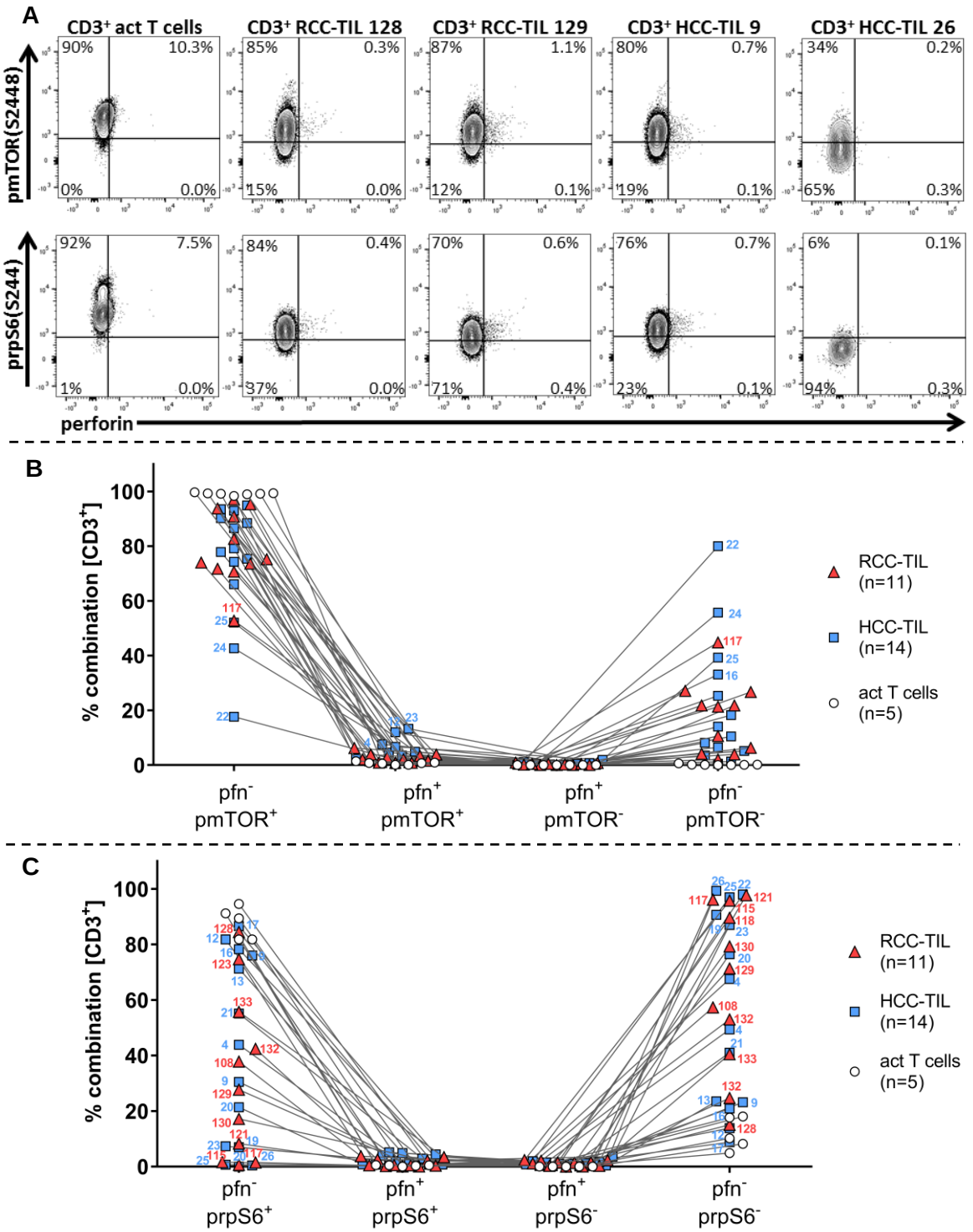

Figure 26: Relation of pmTOR(S2448), prpS6(S244) and perforin in activated T cells, RCC-TIL and HCC-TIL

Tissue suspensions and activated T cells were stained for flow cytometry (table 18, see p.89). Combinations of pmTOR(S2448) and perforin or prpS6(S244) and perforin were analyzed within gated $CD3^+$ T cells. A: Exemplary dot plots of RCC-TIL, HCC-TIL and activated T cell (act T cells). B and C: Summary of calculated frequencies of cells with combinations of pmTOR(S2448) and perforin (pfn) (B) or combinations of rpS6(S244) and perforin (C) within gated $CD3^+$ T cells of RCC-TIL, HCC-TIL and activated T cells. Each symbol represents one TIL or one sample of activated T cells, lines connect different combinations of the same individual. Numbers indicate patient-IDs (red: RCC-TIL, blue: HCC-TIL).

To address if perforin positivity requires activity of both mTOR and rpS6, the pmTOR(S2448)$^+$perforin$^+$ subset was gated and questioned for positivity of prpS6(S244).

It was found that pmTOR(S2448)$^+$perforin$^+$ cells were also positive for prpS6(S244), indicating that the downstream activation of prpS6 through mTOR leads to perforin positivity. Exemplary dot plots are shown in figure 27.

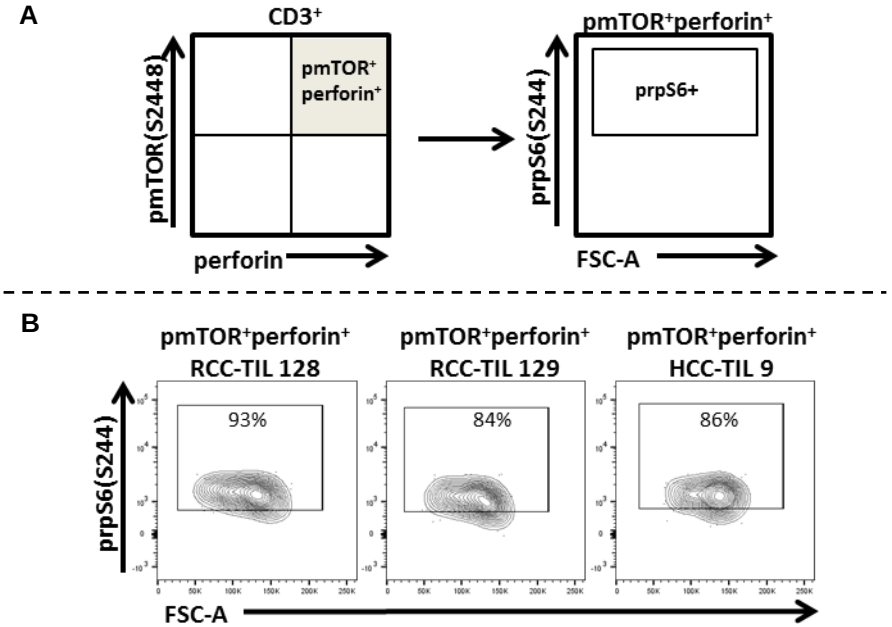

Figure 27: Relation of prpS6(S244) and pmTOR(S2448)$^+$perforin$^+$ cells in activated T cells, RCC-TIL and HCC-TIL
Tissue suspensions and activated T cells were stained for flow cytometry (table 18, see p.89). A: Within preselected CD3$^+$ T cells, pmTOR(S2448) was plotted against perforin and T cells being pmTOR(S2448)$^+$perforin$^+$ were selected to determine positivity of prpS6. B: Exemplary dot plots of RCC-TIL and HCC-TIL.

7.6 T cell anergy in CD8$^+$ TIL

T cell anergy arises from incomplete T cell activation, which occurs when T cell receptors are triggered by peptide-MHC ligands without co-stimulation and was initially described for CD4$^+$ T cells (35). A hallmark for anergic CD4 T cells is upregulated diacylglycerol kinase α (DGK-α) which degrades diacylglycerol (DAG). Reduction in DAG is followed by inhibition of ERK, suppression of PI3K, downstream inhibition of AKT and mTOR (18,35). The phenomenon of upregulated DGK-α and reduced levels of phosphorylated ERK and AKT was found in CD8$^+$ RCC-TIL (40). It is further known, that the transcription factor FoxO1 (forkhead box protein O1) regulates transcription of DGK-α (18) and also promotes PD-1 expression in exhausted CD8$^+$ T cells of chronic infection (21). A brief overview of FoxO1, DGK-α and PD-1 and their relation within the signaling cascade of the TCR in CD8$^+$ T cells are exemplified in figure 28.

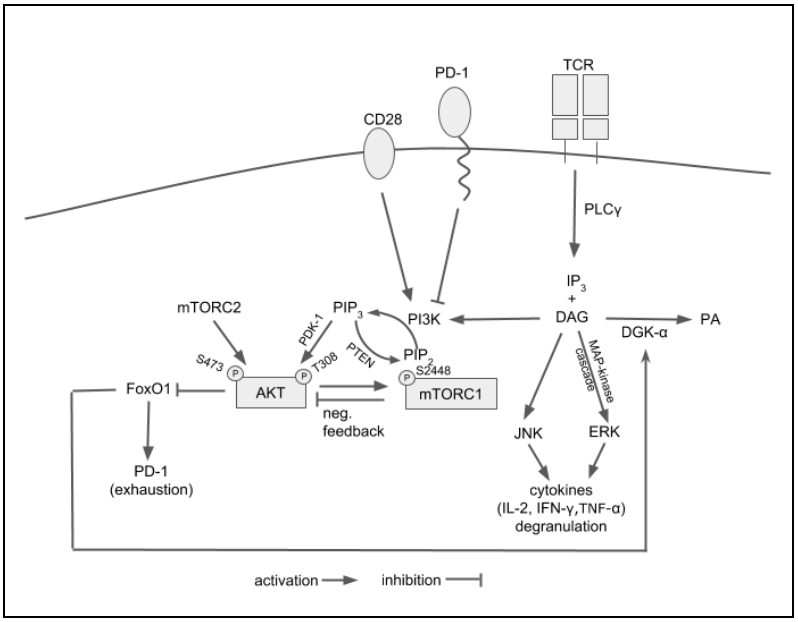

Figure 28: Signaling of the TCR in CD8$^+$ T cells with focus on T cell anergy and exhaustion
CD28: co-stimulatory molecule, PD-1: programmed cell death protein 1 (co-inhibitory receptor), TCR: T cell receptor, PLCγ: protein lipase γ, FoxO1: forkhead box protein 1, AKT: protein kinase B, mTORC1/C2: mammalian targets of rapamycin complex 1 (C1) or 2 (C2), PI3K: phosphoinositide-3-kinase, PIP3: phosphatidylinositol-(3,4,5)-trisphosphate, PIP_2: phosphatidylinositol-(4,5)-bisphosphate, PI3K: phosphoinositide-3 kinase; PTEN: phosphatase and tensin homolog, IP_3: inositoltrisphosphate, DAG: diacylglycerol, DGK-α: diacyglycerol kinase α, PA: phosphatic acid, JNK: c-Jun N-terminal kinase, ERK: extracellular regulated kinase.

While the hyporesponsive state of RCC-TIL and HCC-TIL is clearly documented, the underlying cause of this unresponsiveness is not yet delineated and might be multifactorial (anergy, tolerance, exhaustion or inhibition). This knowledge, however, is required in order to select the most effective intervention strategies. Thus, the interplay between FoxO1, DGK-α and PD-1 was assessed in CD8$^+$ RCC-TIL and HCC-TIL by staining tissues suspensions with respective antibodies and performing flow cytometry (table 19).

Table 19: Staining to address T cell anergy and exhaustion (staining combination 4)

Target/epitope	Fluorochrome	Cell subset/function
Viability: LIVE/DEAD™ Fixable Blue Dead Cell Stain	Indo-1-violet	staining of dead cells
CD45	Pe-Cy7	leukocytes
CD3	PerCp-Cy™5.5	T cells
CD8	V500	$CD8^+$ T cells
CD4	APC-eFluor 780	$CD4^+$ T cells
CD19/CD20	Alexa Fluor® A700	B cells
CD56	V450	NK cells
PD-1	PE	exhaustion marker
DGK-α	unmarked, detected by secondary antibody (Alexa Fluor® 647)	marker for T cell anergy (diacylglycerol kinase α)
FoxO1	unmarked, detected by secondary antibody (Alexa Fluor® 488)	transcription factor of PD-1 and DGK-α (forkhead box protein O1)

7.6.1 DGK-α expression divides RCC-TIL and HCC-TIL into two groups

DGK-α expression levels were addressed by measuring DGK-α mean fluorescence intensities in preselected $CD8^+$ T cells of cell suspensions of non-tumor and tumor tissues of kidney and liver (figure 29). Two groups of patients were identified: five RCC and five HCC patients were marked by higher expression levels of DGK-α in TIL compared with NIL. The second group of six RCC and three HCC patients had lower DGK-α expression in TIL than in NIL, which was significant for r-NIL and RCC-TIL.

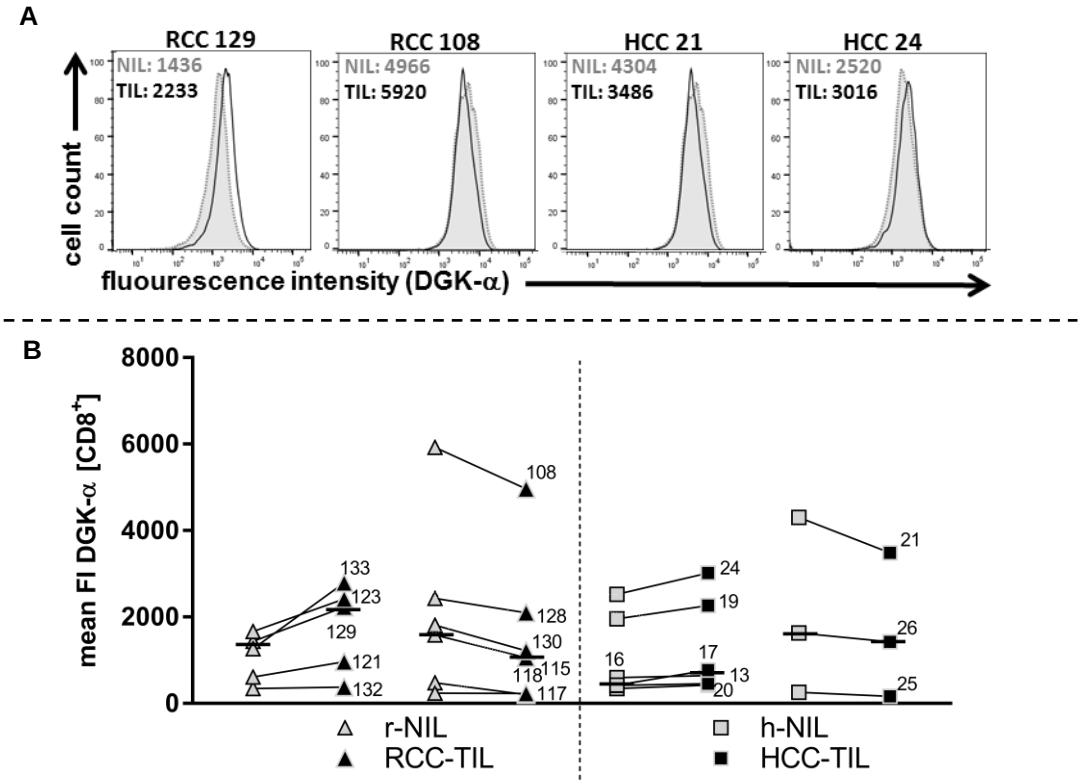

Figure 29: DGK-α expression levels in NIL and TIL of kidney and liver
Tissue suspensions were stained to address T cell anergy (table 19, see p. 97) and analyzed by flow cytometry. A: Exemplary histograms of DGK-α expression addressed by the fluorescence intensity of DGK-α in preselected $CD8^+$ NIL (grey) and TIL (black). Numbers indicate mean fluorescence intensities. B: Summarizing figure of mean fluorescence intensities (FI) of r-NIL, RCC-TIL, h-NIL and HCC-TIL. Vertical dashed line separate cells suspensions from kidney and liver. Numbers indicate patient-IDs, lines connect tissues from the same individual and horizontal lines indicate the median of one group. Significance between NIL and TIL in one group was statistically addressed by Mann-Whitney U test but did not reveal significance.

7.6.2 DGK-α correlates with expression of FoxO1 in $CD8^+$ TIL

Exemplary dot plots (figure 30 A) indicate a correlation of high FoxO1 with high DGK-α in $CD8^+$ RCC-TIL and HCC-TIL on a single cell level, showing that high FoxO1 is associated with high DGK-α ($FoxO1^{high}$/DGK-$α^{high}$) and vice versa ($FoxO1^{low}$/DGK-$α^{low}$). The relation between FoxO1 and DGK-α was further addressed by Spearman´s correlation analysis of expression levels of both markers in $CD8^+$ RCC-TIL and HCC-TIL (figure 30 B and C) and revealed nearly linear correlations (r^2(RCC-TIL)=0.63; r^2(HCC-TIL=0.86)).

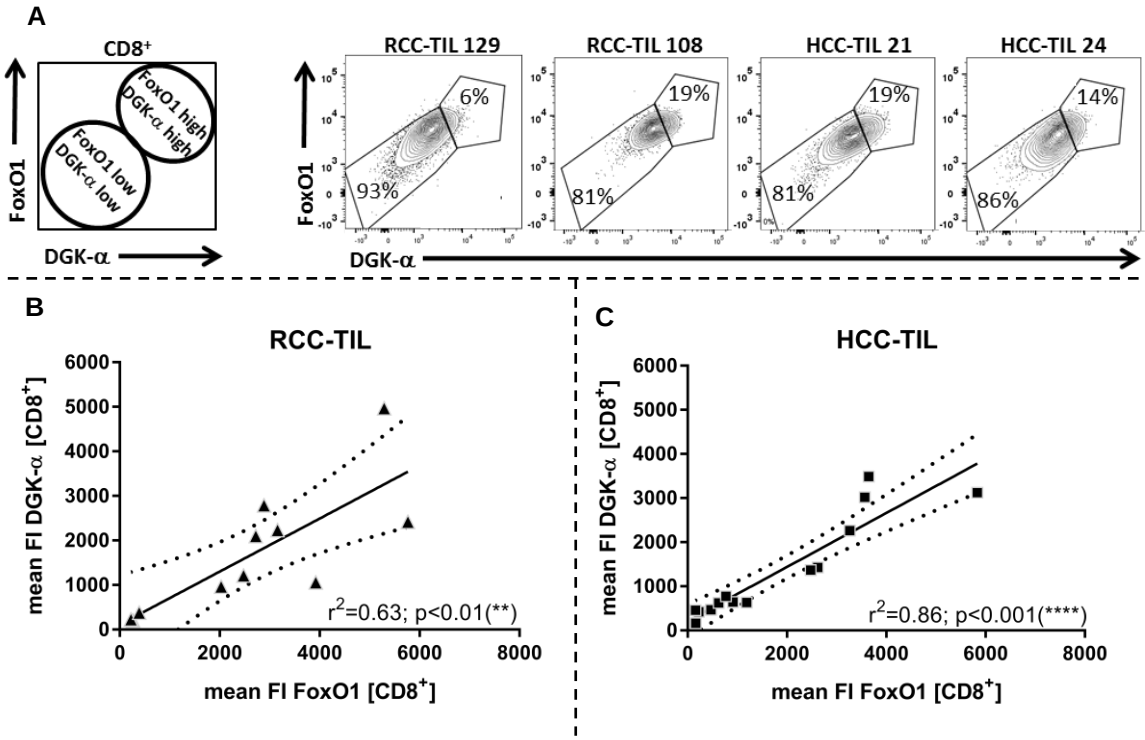

Figure 30: Correlation of DGK-α and FoxO1 in CD8$^+$ RCC-TIL and HCC-TIL
Tissue suspensions were stained to address T cell anergy (table 19, see p. 97) and analyzed by flow cytometry. A: Schematic gating strategy and exemplary dot plots of DGK-α and FoxO1 in preselected CD3$^+$CD8$^+$ RCC-TIL and HCC-TIL. B and C: Spearman´s rank correlation analysis of expression levels of DGK-α and FoxO1 (addressed by mean fluorescence intensities (FI) in CD3$^+$CD8$^+$ RCC-TIL (B) and HCC-TIL (C). One symbol represents one patient. Correlation coefficient r^2 was determined by Spearman´s correlation test, lines indicate the best-fit line of the correlation and dotted curves are 95%-confidence bands of the best-fit line. *p<0.05; **p<0.01; *** p<0.001; ****p<0.0001.

7.7 Exhaustion in CD8$^+$ TIL

T cell exhaustion was described as a state of dysfunction in chronic infection and cancer that develops due to antigen persistence (42).

7.7.1 PD-1 is enriched in CD8$^+$ TIL

FoxO1 was not only shown to drive T cell anergy by inducing transcription of DGK-α (18), but is also related to exhausted T cells promoting PD-1 expression (21). Figure 31 A shows exemplary dot plots for two RCC-TIL and HCC-TIL with low and high frequencies of PD-1. The dot plots display FoxO1 and PD-1 overlaid by DGK-α fluorescence intensities. PD-1$^+$ cells were found among FoxO1$^-$ and FoxO1$^+$ cells, indicating that PD-1 expression was not exclusively related to FoxO1 expression. Nevertheless, cell frequency analysis of PD-1$^+$ cells among preselected FoxO1$^-$ or FoxO1$^+$ subsets showed that PD-1$^+$ cells were significantly more prevalent in the FoxO1$^+$ subsets of CD8$^+$ RCC-TIL (median 64%; range: 47% – 91%) and HCC-TIL (median 41%; range: 30% - 97%;

outlier HCC 20: 0%) compared with the FoxO1$^-$ subsets, although that subset also harbored many PD-1$^+$ cells (RCC-TIL: range: 24% – 84%; HCC-TIL: range: 5% - 97%).

Moreover, high expression levels of DGK-α (red color) were distributed over PD-1$^+$ and PD-1$^-$ cells, indicating that PD-1 is not linked to DGK-α expression. However, as revealed bevor (see p.99), high expression levels of DGK-α were only found in FoxO1$^+$ cells.

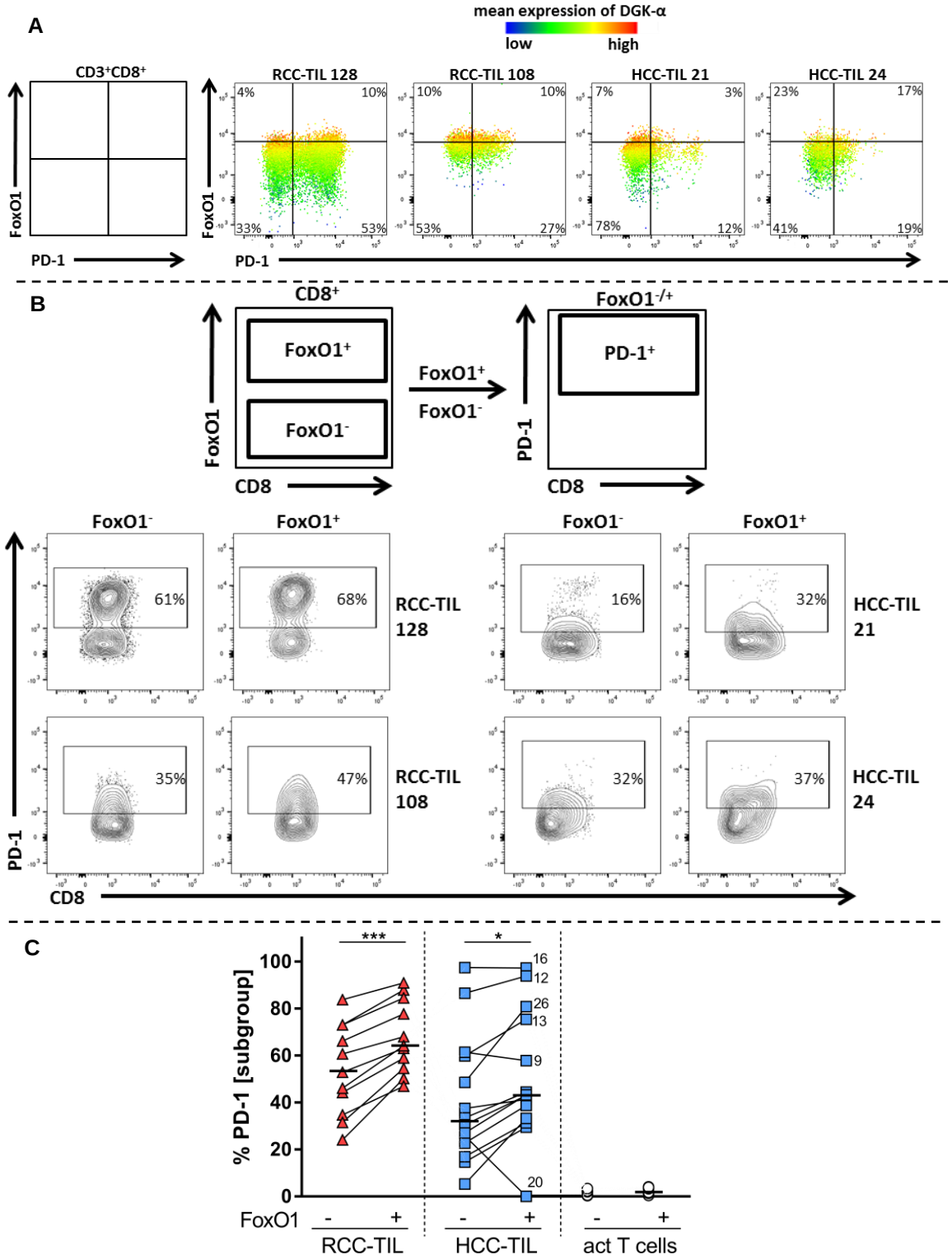

Figure 31: Relation between FoxO1, DGK-α and PD-1 in CD8$^+$ RCC-TIL and HCC-TIL
Tissue suspensions were stained to address T cell anergy and exhaustion and analyzed by flow cytometry. A: Schematic gating strategy and exemplary dot plots of FoxO1, DGK-α and PD-1 overlaid with mean expression of DGK-α in preselected CD8$^+$ RCC-TIL and HCC-TIL. Expression levels of DGK-α are visualized by a color gradient (blue: low expression; red: high expression). B: Gating strategy and exemplary dot plots to determine relation of FoxO1 and PD-1. Percentages of PD-1 were addressed within preselected FoxO1$^{-/+}$ populations. C: Summarizing figure displaying percentages of PD-1 in FoxO1 negative (-) and FoxO1 positive (+) subgroups of CD8$^+$ RCC-TIL and HCC-TIL. One symbol represents one sample, horizontal lines indicate the median within one group and vertical dotted lines separate different groups. Significance was addressed by Wilcoxon matched pairs signed rank test between two corresponding subsets (*p<0.05; **p<0.01; ***p<0.001; ****p<0.0001). If not indicated differently, differences between samples were not significant.

7.7.2 RCC-TIL and HCC-TIL have low frequencies of T cells co-expressing PD-1 and LAG-3

Co-inhibitory receptor PD-1 has been assigned to T cell exhaustion, but is also expressed upon T cell activation (41,81). PD-1$^+$ exhausted T cells are distinguished from PD-1$^+$ activated T cells by prolonged and high expression of PD-1 with additional expression of other inhibitory receptors like lymphocyte activation gene 3 (LAG-3) or T cell immunoglobulin and mucin-domain containing (TIM-3) (41). In the following, the staining combination of PD-1 and LAG-3 together with the proliferation marker Ki-67 was applied (table 20). It was hypothesized, that exhausted T cells should be represented by PD-1$^+$LAG-3$^+$ cells, whereas PD-1$^+$Ki-67$^+$ T cells should indicate activated T cells.

Table 20: staining combination to address T cell exhaustion (staining combination 1)

Target/epitope	Fluorochrome	Cell subset/function
Viability: LIVE/DEAD™ Fixable Blue Dead Cell Stain	Indo-1-violet	staining of dead cells
CD45	Pe-Cy7	leukocytes
CD3	PerCp-Cy™5.5	T cells
CD8	V500	CD8$^+$ cells
CD4	APC-eFluor 780	CD4$^+$ cell
CD19/CD20	Alexa Fluor® A700	B cells
CD56	V450	NK cells
CD14	PB	monocytes/macrophages
PD-1	PE	activation/exhaustion marker
Ki-67	Alexa Fluor® A488	proliferation marker
LAG-3	ATTO 647N	activation/exhaustion marker

It was observed (figure 32) that the frequency of PD-1$^+$ cells of TIL was significantly higher compared with corresponding NIL for both kidney and liver tissues (median r-NIL 11%; range: 4% - 26%; median h-NIL 12%; range: 1% - 60%). HCC-TIL were more heterogeneous (range: 8% - 96%) compared with RCC-TIL (range: 24% - 78%).

LAG-3$^+$ cells were of very low frequency but significantly more frequent in RCC-TIL (median 5%; range: 0% - 13%) or HCC-TIL (median 9%; range: 1% - 17%) compared with the corresponding NIL (median r-NIL 2%; range: 0% - 12%; median h-NIL 1%;

range: 0% - 2%). Activated T cells had low frequencies of both PD-1 (median 2%) and LAG-3$^+$ (median 3%).

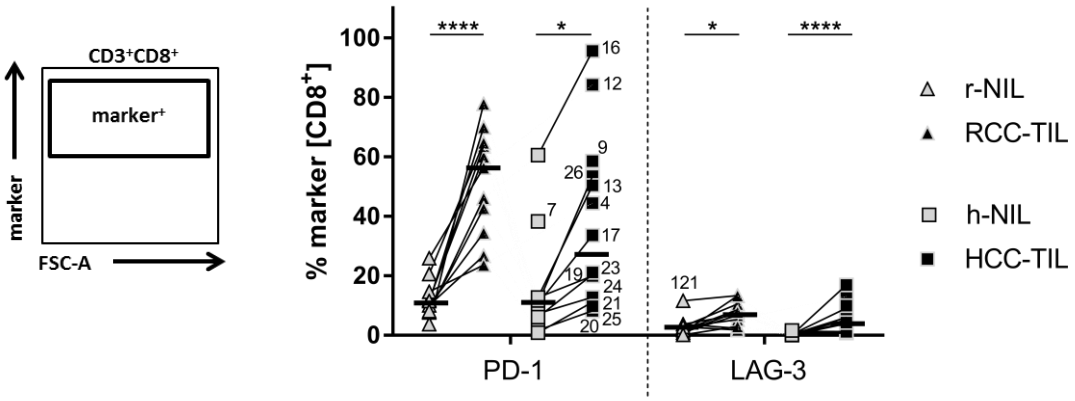

Figure 32: Analysis of co-inhibitory receptors PD-1 and LAG-3 in RCC-TIL and HCC-TIL
Tissue suspensions were stained to address exhaustion (table 20, see p. 102) and analyzed by flow cytometry. Figure depicts schematic gating strategy and summarizing graph of single marker analysis. Each symbol represents one individual and lines connect samples of one individual. Significance between NIL and TIL in one group was statistically determined by Mann-Whitney U test (*p<0.05; **p<0.01; ***p<0.001; ****p<0.0001). Only significant differences between samples are indicated. Small numbers indicate patient-IDs.

Since co-expression of multiple co-inhibitory receptors is described as a hallmark of CD8$^+$ T cell exhaustion (41,42), co-expression of PD-1 and LAG-3 was determined for pregated CD8$^+$ TIL (figure 33).

PD-1$^+$LAG-3$^-$ cells ranged from 23% – 65% in CD8$^+$ RCC-TIL but frequencies of PD-1$^+$LAG-3$^-$ cells varied strongly in CD8$^+$ HCC-TIL, dividing patients into those with high frequencies (range 34% – 91%) and low frequencies (range 7% – 17%), identifying the same patients as in the single marker analysis. PD-1 and LAG-3 double positive T cells were infrequent in RCC-TIL and HCC-TIL (median of both 7%) and LAG-3$^+$ TIL without PD-1 were neither detected in CD8$^+$ RCC-TIL or HCC-TIL.

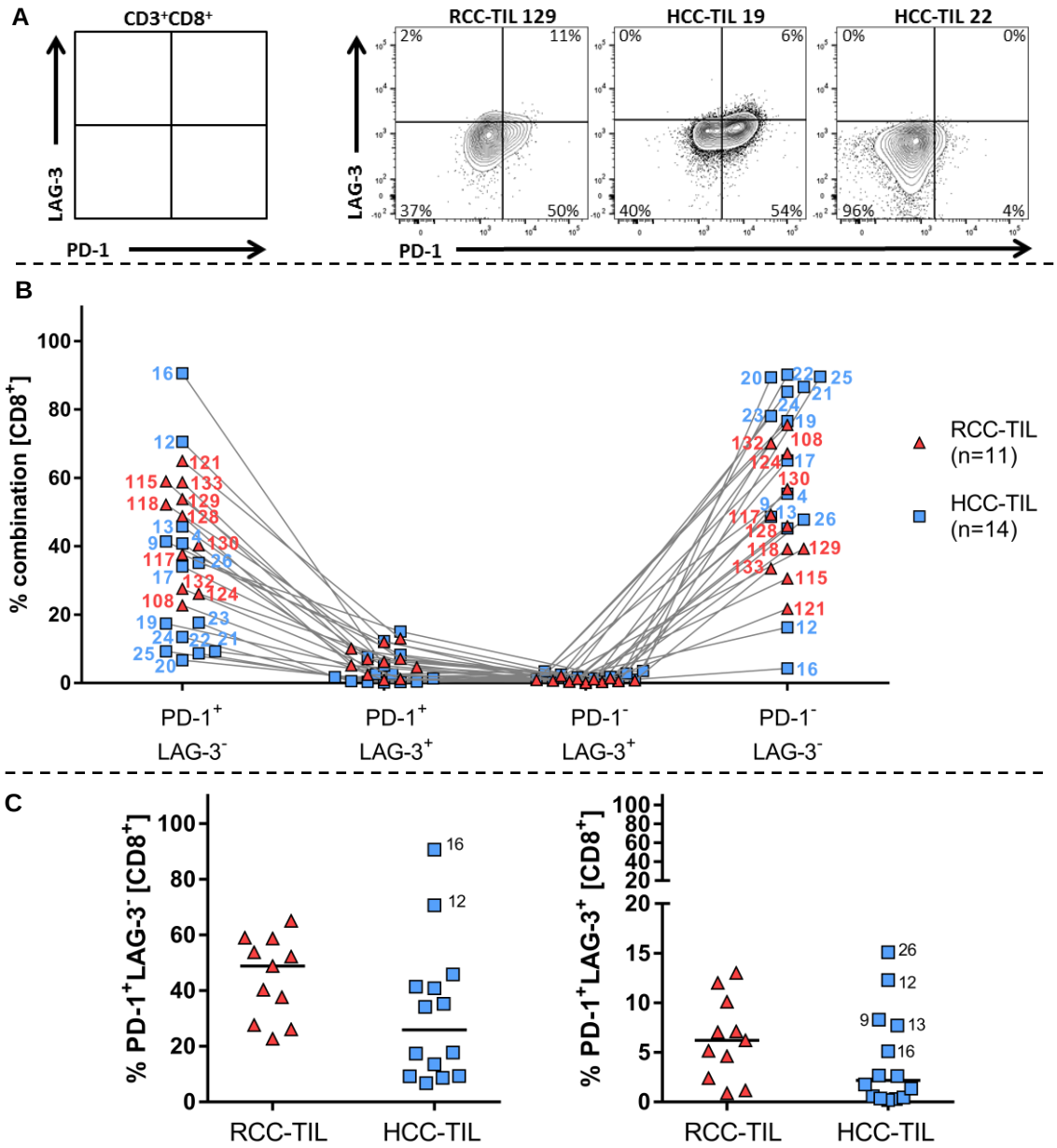

Figure 33: Relationship of co-inhibitory receptors PD-1 and LAG-3 in RCC-TIL and HCC-TIL
Tissue suspensions were stained to address exhaustion (table 20, see p. 102) and analyzed by flow cytometry. A: Exemplary dot plots addressing combinations of PD-1 and LAG-3. B: Summarizing graph of combinations of PD-1 and LAG-3. Each symbol represents one tissue and lines connect samples from the same individual. C: The combinations PD-1$^+$LAG-3$^-$ and PD-1$^+$LAG-3$^+$ are visualized separately. Significance was addressed by Mann Whitney U test, but did not reveal significance. Each symbol represents one tissue and small numbers indicate patient-IDs.

7.7.2.1 Ki-67 is expressed in PD-1$^+$LAG-3$^+$ CD8$^+$ TIL

Ki-67 expression was analyzed to facilitate a distinction between exhaustion and activation (figure 34). Single marker analysis of Ki-67 (figure 34 A, see p. 106) revealed very low frequencies of Ki-67$^+$ cells in NIL (median r-NIL 3%; range: 1% - 9%; median h-NIL 1%; range: 1% - 4%) and low, but significantly higher values in corresponding TIL (median RCC-TIL 4%; range: 1% - 7%; median HCC-TIL 5%; range: 2% - 14%).

PD-1^{+}Ki-67^{+} T cells, considered as activated and not exhausted, were detected at comparable low frequencies in RCC-TIL (median 3%, range: 1% - 7%) and in HCC-TIL (median 3%, range: 1% - 13%). Four HCC-TIL had higher percentages (range: 6% - 13%) of PD-1^{+}Ki-67^{+} T cells compared with the main cohort (figure 34 B).

In the combined analysis with PD-1 and LAG-3 (figure 34 C and D), Ki-67^{+} cells were mainly detected in the PD-1 and LAG-3 double positive subset of CD8^{+} RCC-TIL (median 23%; range: 7% - 44%) and HCC-TIL (median 31%; range: 0% - 46%). The frequency of Ki-67 was significantly lower in the PD-1^{+}LAG-3^{-} (median RCC-TIL 4%; range: 0% - 10%; median HCC-TIL 4%; range: 0% - 16%) subset and also significantly lower in the PD-1^{-}LAG-3^{-} (median RCC-TIL 2%; range: 0% - 3%; median HCC-TIL 3%; range: 0% - 13%) subset. Single positive subsets of LAG-3 were not detected and this subgroup is therefore not displayed in the figure.

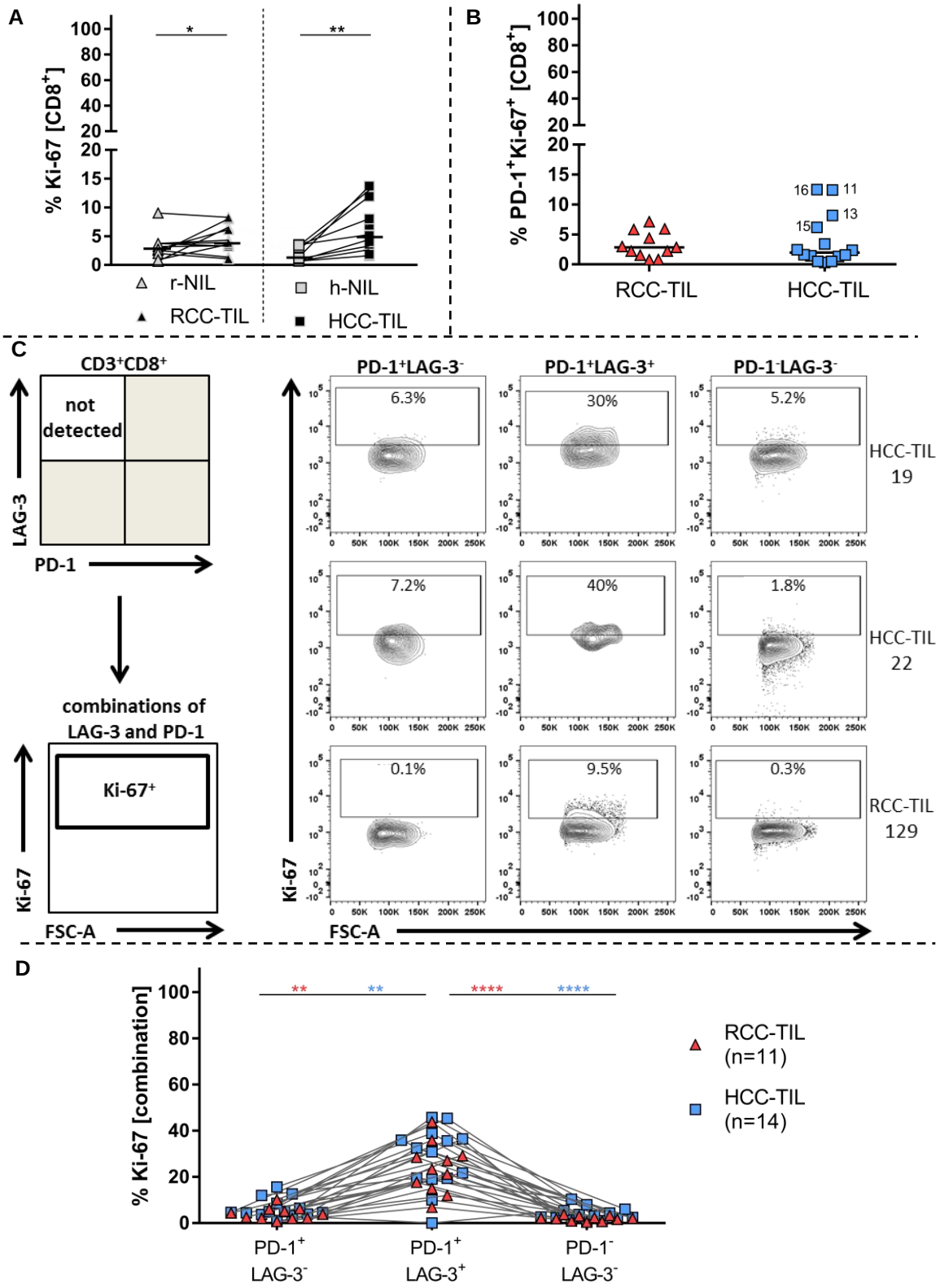

Figure 34: Percentages of Ki-67 in combinations with PD-1 and LAG-3
Tissue suspensions were stained for flow cytometry. A: Ki-67 analysis in pregated $CD3^+CD8^+$ T cells. B: Frequencies of $PD\text{-}1^+Ki\text{-}67^+$ cells in $CD8^+$ TIL. B: Schematic gating strategy and exemplary dot plots to address positivity of Ki-67 in combinations of PD-1 and LAG-3 in $CD8^+$ TIL. C: Summarizing graph of $Ki\text{-}67^+$ cells in combinations of PD-1 and LAG-3. Each symbol represents one tissue, lines connect samples from the same individual. Horizontal lines indicate the median within one group, vertical dotted lines separate different groups. Significance was determined by Mann-Whitney U test (*p<0.05; **p<0.01; ***p<0.001; ****p<0.0001). Only significant differences are indicated. Small numbers indicate patient-IDs.

7.7.3 Transcription factors T-bet and Eomes, and PD-1 in CD8$^+$ TIL

Exhausted CD8$^+$ T cells are not only described by high expression of multiple inhibitory receptors (41), but can also be addressed by T-box transcription factor T-bet and transcription factor Eomesodermin (Eomes): T-bet^{high}/Eomes^{low}/PD-1^{low} subset is considered to still have potential for further division, can moderately produce IFN-γ and TNF-α and is more responsive to anti-PD-L1/anti-PD-1 reinvigoration (42,82). On the contrary, exhausted CD8$^+$ T cells defined by T-bet^{low}/Eomes^{high}/PD-1^{high} show low potential for further division, but have maintained cytolytic activity and high levels of granzyme B. They are thought to be less responsive to anti-PD-L1/anti-PD-1 therapy (42,82,83).

The staining combination (table 21) to analyze RCC-TIL and HCC-TIL by flow cytometry included T-bet and Eomes in combination with PD-1, perforin and granzyme B.

Table 21: Staining combination to determine T cell subsets by transcription factors, PD-1 and cytotoxic proteins (staining combination 5)

Target/epitope	Fluorochrome	Cell subset/function
Viability: LIVE/DEAD™ Fixable Blue Dead Cell Stain	Indo-1-violet	staining of dead cells
CD45	Pe-Cy7	leukocytes
CD3	Alexa Fluor® A700	T cells
CD8	V500	CD8$^+$ T cells
CD4	APC-eFluor 780	CD4$^+$ T cells
CD56	V450	NK cells
PD-1	PerCp-Cy™5.5	activation/exhaustion marker
T-bet	eFluor™660	transcription factor to discriminate T cell subsets, high in T effector cells, low in T memory
Eomes	PE	transcription factor to discriminate T cell subsets, associated with T effector cells and memory development
perforin	FITC	cytolytic molecule
granzyme B	PE-TexasRed®	serine protease

7.7.3.1 Tbet^{low}/Eomes^{+}/PD-1^{+} expression in CD8^{+} HCC-TIL identifies two groups of HCC patients

Expression patterns of T-bet and Eomes can be used to identify CD8^{+} T cell subsets: naïve CD8^{+} T cells are defined by low levels of T-bet and Eomes whereas cytotoxic effector CD8^{+} T cells are marked by high levels of T-bet and Eomes. Memory-like CD8^{+} T cells show low expression of T-bet but high expression of Eomes (11–15).

The gating scheme and exemplary dot plots are visualized in figure 35 A, discriminating three CD8^{+} T cell subsets defined as T-bet^{low}/Eomes^{-} (T naïve, Tn), T-bet^{low}/Eomes^{+} (memory-like, Tm-like) and T-bet^{high}/Eomes$^{\pm}$ (cytotoxic T cells, CTL).

In CD8^{+} RCC-TIL, all three T cell subsets were found in all patients (n=11), while a majority of HCC-patients lacked the T-bet^{low}/Eomes^{+} T cells (n=10 of 14 patients, designated Tm^{-}HCC-TIL). The smaller cohort of HCC-patients were TIL having all three T-bet/Eomes subsets (n=4; of 14 patients, designated Tm^{+}HCC-TIL). T-bet^{low}/Eomes^{+} cells were also absent in activated T cells (figure 35 B).

Figure 35 C-F summarizes the prevalence of each T cell subset (T-bet^{low}/Eomes^{-}, T-bet^{low}/Eomes^{+} and T-bet^{high}/Eomes$^{\pm}$) within gated CD8^{+} T cells of RCC-TIL (C), Tm^{+}HCC-TIL (D), Tm^{-}HCC-TIL (E) and activated T cells (F).

In all TIL independent of tissues source, the Tn subset was the most frequent one (median RCC-TIL 72%, median Tm^{+}HCC-TIL 70%, median Tm^{-}HCC-TIL 79%). The subset of T-bet^{low}/Eomes^{+} was detected in ranges of 7% - 35% in RCC-TIL and 7% - 22% in Tm^{+}HCC-TIL. CTL were represented in ranges of 7% - 45% in RCC-TIL, 8% - 37% in Tm^{-}HCC-TIL and 5% - 35% in Tm^{+}HCC-TIL. Activated T cells were mainly CTL (median 98%), the Tm-like subset was not detected and percentages of Tn were low (median 2%).

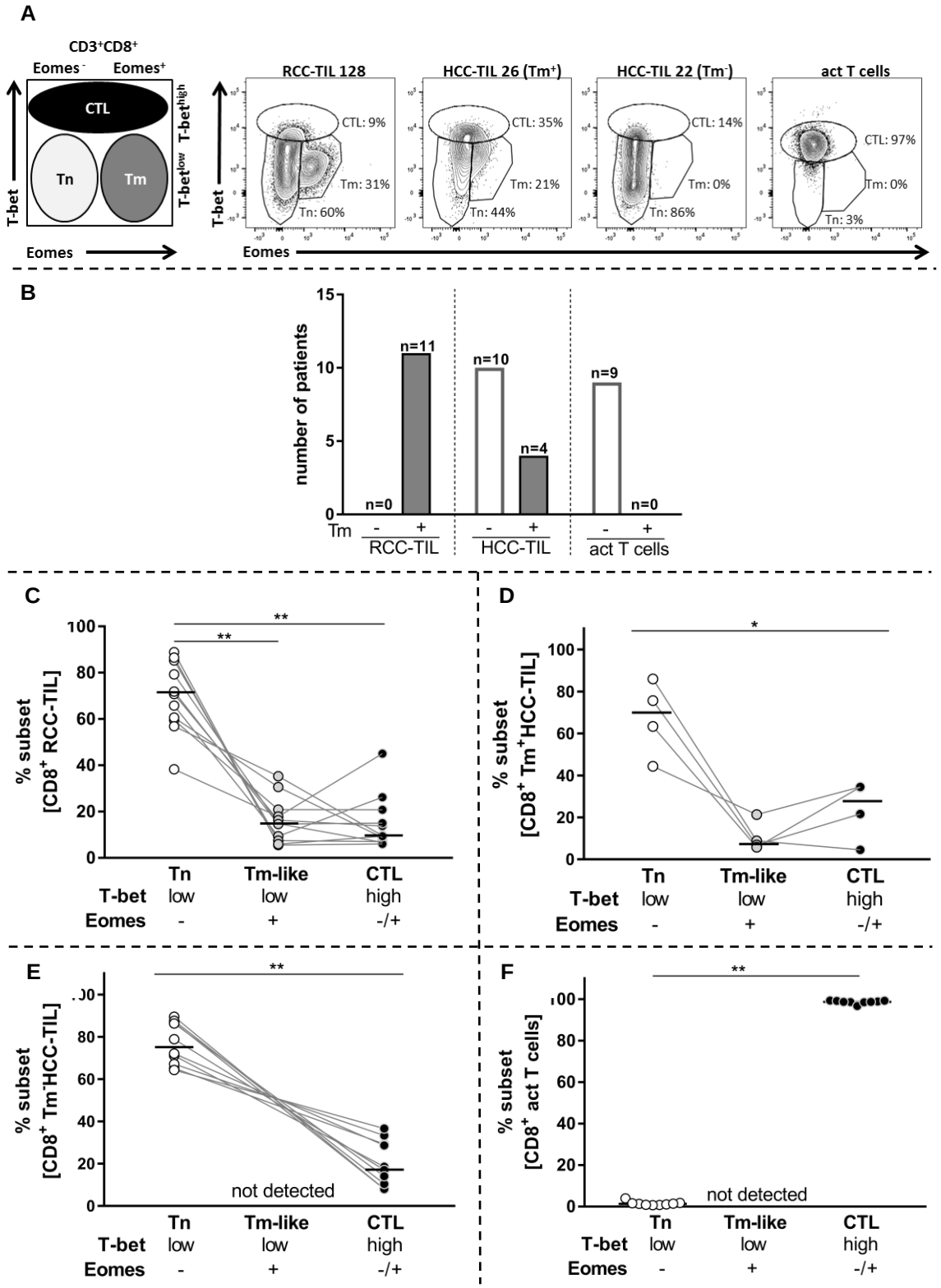

Figure 35: T cell subsets defined by T-bet and Eomes in CD8$^+$ RCC-TIL, HCC-TIL and activated T cells
A: Gating strategy and exemplary dot plots delineating Tn (T naïve; T-bet$^{-/low}$/Eomes$^-$), Tm (memory-like, T-bet^{low}/Eomes$^+$) and CTL (cytotoxic T cells, T-bet^{high}/Eomes$^{\pm}$) subsets in pregated CD3$^+$CD8$^+$ T cells of RCC-TIL, Tm$^+$HCC-TIL, Tm$^-$HCC-TIL and activated T cells (act T cells). B: Bars represent numbers of patients or healthy donors that did not have (-) or had (+) the T-bet^{low}/Eomes$^+$ subset in CD8$^+$ T cells. Grey: patients with (+) and white bars: patients without (-) T-bet^{low}/Eomes$^+$subset. C-F: Summarizing graphs of T cell subsets defined by T-bet and Eomes in RCC-TIL (C), Tm$^+$HCC-TIL (D), Tm$^-$HCC-TIL (E) and activated T cells (F). One symbol represents one patient or healthy donor. Significance was determined by Friedmann test and Dunn´s Post-Hoc comparisons in C-D and by Wilcoxon matched pairs signed rank test in E-F (*p<0.05; **p<0.01; ***p<0.001; ****p<0.0001). Only statistical significant differences are indicated.

The T-bet/Eomes $CD8^+$ T cell subsets identified in TIL were further characterized with regard to expression of PD-1. In a first step, the mean fluorescence intensity of PD-1 in $CD8^+$ T cell subsets was visualized by a color-gradient (blue to red) and overlaid onto the T-bet/Eomes dot plots (examples are shown in figure 36).

High levels of PD-1 staining were mainly localized in the T-bet^{low}/$Eomes^+$ Tm-like cells and to some extent in the naïve T-bet^{low}/$Eomes^-$ T cell subset. In a second step, the frequencies of the PD-1^+ cells within the different T-bet/Eomes $CD8^+$ T cell subsets were calculated.

Considering each patient's TIL individually, a consistent distribution of PD-1 among the T-bet^{low}/$Eomes^+$ $CD8^+$ T cell subsets was observed. All TIL had the highest PD-1 frequency in the T-bet^{low}/$Eomes^+$ Tm-like population (median RCC-TIL 80%, range: 55% – 95%, median Tm^+HCC-TIL 90%; range: 81% - 98%), followed by lower frequencies of PD-1 in the T-bet^{low}/$Eomes^-$ Tn-like subset (median RCC-TIL 59%; range: 34% - 80%, median Tm^+HCC-TIL 70%; range: 55% – 97%). Lowest prevalence of PD-1 was found in the CTL T-bet^{high}/$Eomes^{\pm}$ $CD8^+$ T cells. RCC-TIL showed median frequencies of 23% (range: 10% - 50%) and in Tm^+HCC-TIL, two patients had low (20% and 35%) and two patients had high frequencies of PD-1 (91% and 95%) within their CTL population. Tm^-HCC-TIL had in general less PD-1^+ and the percentages of PD-1^+ cells were similar in Tn and CTL (median Tn 28%; range: 8% – 56%; median CTL 21%; range: 8% – 51%).

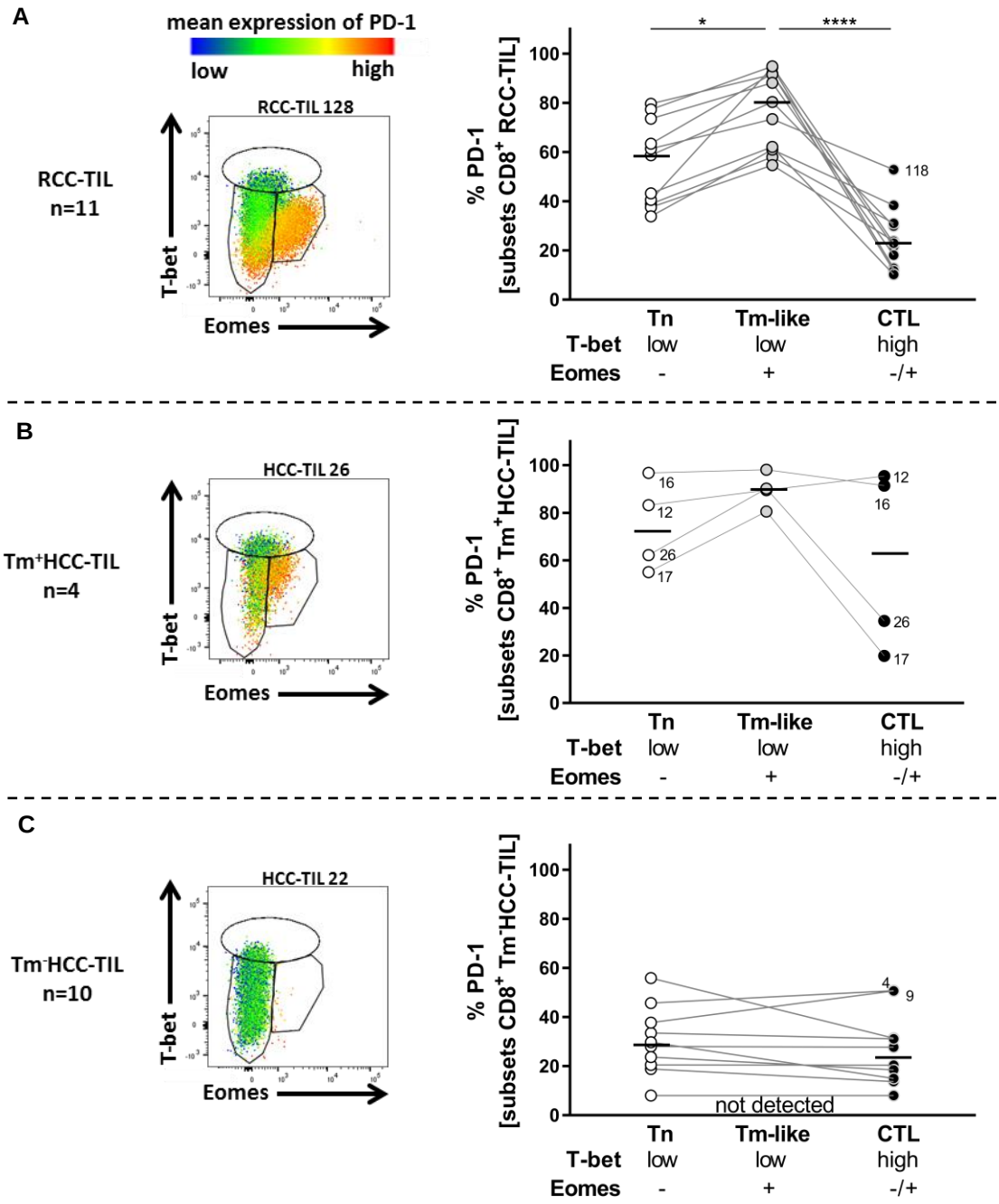

Figure 36: PD-1 in T-bet/Eomes subsets of CD8$^+$ RCC-TIL and HCC-TIL
Samples were stained for flow cytometry (table 21, see p. 107) and T-bet and Eomes are presented as dot plots of gated CD8$^+$ T cells. Mean fluorescence intensities (MFIs) of PD-1 are displayed by color gradient (blue to red), overlaid onto the T-bet and Eomes dot plots. Graphs summarize the percentages of gated PD-1$^+$ cells in T-bet/Eomes CD8$^+$ T cell subsets. One symbol represents one patient or healthy donor, horizontal lines indicate median of one subset. Significance was statistically determined by Friedmann test and Dunn´s Post-Hoc comparisons in A-B and by Wilcoxon matched pairs signed rank test in C (*p<0.05; **p<0.01 ***p<0.001;****p<0.0001). If not indicated differently, differences between samples were not significant. A: RCC-TIL. B: Tm$^+$ HCC-TIL. C: Tm$^-$HCC-TIL.

7.7.3.2 T-bet^{low}/Eomes^{+} TIL express granzyme B but not perforin

Two questions resulted from the previous findings: First, a T-bet^{high}/Eomes$^{\pm}$ subset was identified in CD8^{+} TIL that had overall low levels of PD-1. As T-bet^{high}/Eomes$^{\pm}$ T cells are designated as cytotoxic T cells (11–15), it was of interest if these T cells in TIL were positive for perforin and granzyme B. Second, the T-bet^{low}/Eomes^{+} subset, designated as Tm-like (11–15), showed high PD-1 expression and does therefore not necessarily fit the memory cell description but might correspond to the features of terminally exhausted T cells described in literature (42,83). Perforin and granzyme B were part of the staining combination (table 21) allowing co-analysis with T-bet/Eomes.

Perforin and granzyme B expression levels were displayed by a color-gradient and overlaid on the T-bet/Eomes dot plots (figure 37 A) exemplary dot plots of RCC-TIL, Tm^{+}HCC-TIL and Tm^{-}HCC-TIL). This visualized that perforin as well as granzyme B staining intensities were highest in the CTL subset of all TIL.

Next, the percentages of perforin^{+} and granzyme B^{+} cells within the different T-bet/Eomes subsets were calculated (figure 37 B-E). Frequencies of perforin were consistently low across all TIL samples in the Tn T-bet^{low}/Eomes^{-} and Tm-like T-bet^{low}/Eomes^{+} CD8^{+} subset. Concerning the CTL subset, the frequencies of perforin varied from very high (around 80%) to very low (0%). Thus, this analysis identified some RCC-TIL and HCC-TIL with CTL being very low in perforin.

In general, granzyme B had a higher prevalence as perforin in all TIL and was detected in all T-bet/Eomes CD8^{+} T cell subsets with varying frequency. Highest percentages were consistently observed in CTL (median RCC-TIL 89%; median Tm^{+}HCC-TIL 70%; median Tm^{-}HCC-TIL 80%) compared with the Tn and Tm-like subsets.

To conclude, granzyme B was detected at high frequencies in the Tbet^{low}/Eomes^{+} Tm-like cells, although this subset was almost devoid of perforin. Together with the observation of high PD-1 expression in this subset, it is likely that these Tbet^{low}/Eomes^{+} T cells correspond to exhausted T cells as described in literature (42,44,83).

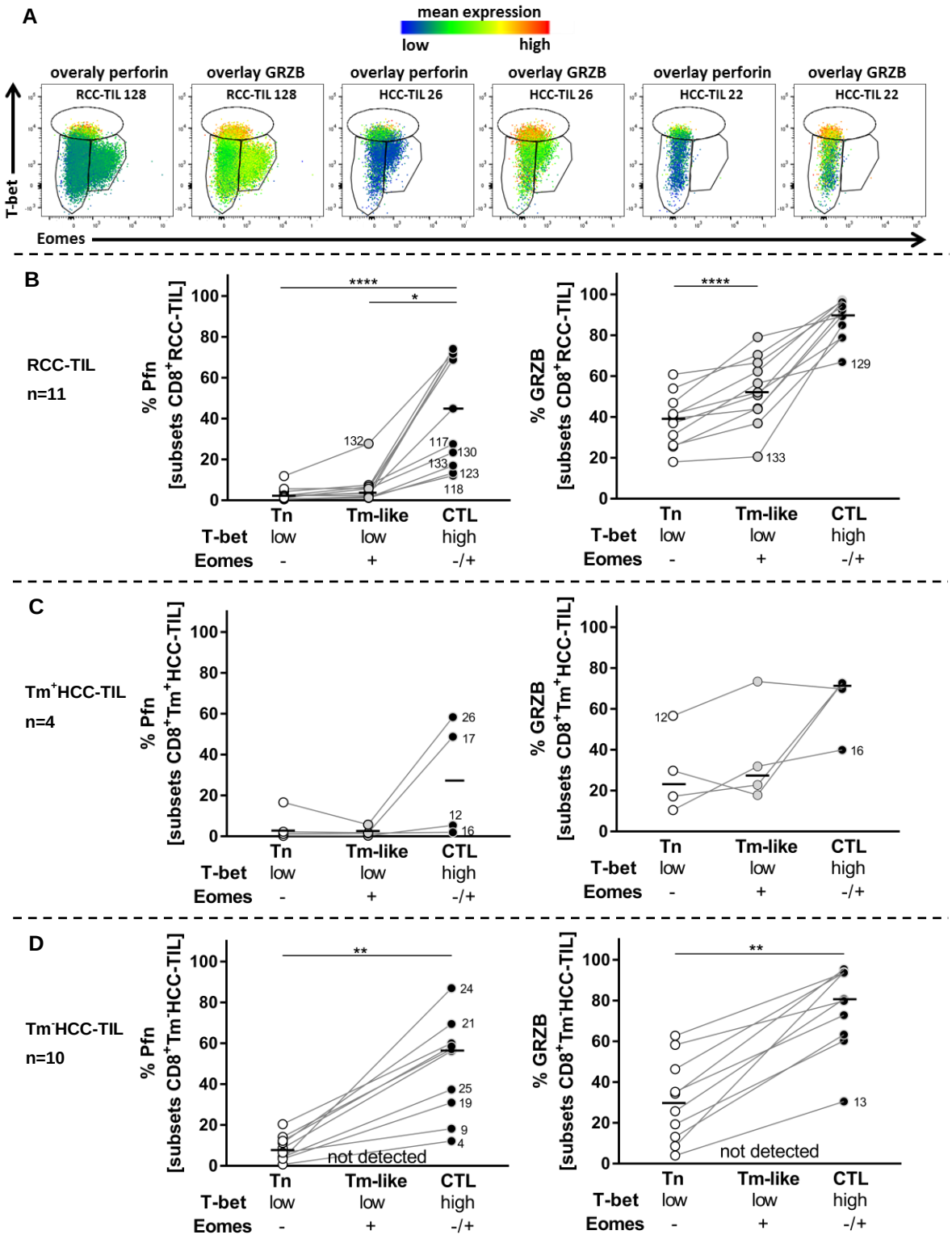

Figure 37: Frequencies of perforin and granzyme B in CD8$^+$ T cell subsets defined by T-bet/Eomes in CD8$^+$ RCC-TIL and HCC-TIL

Samples were stained for flow cytometry (table 21, see p. 107). A: Exemplary dot plots show CD8$^+$ T cell subsets defined by T-bet and Eomes presented as dot plots. Mean expression of perforin (Pfn) and granzyme B (GRZB) are overlaid by color gradient (blue representing lowest expression and red highest expression). Graphs summarize the percentages of gated Pfn$^+$ (left) and GRZB$^+$ (right) cells in gated T bet/Eomes CD8$^+$ T cell subsets of RCC-TIL (B), Tm$^+$HCC-TIL (C) and Tm-HCC-TIL (D). One symbol represents one patient or healthy donor and horizontal lines indicate median of one subset. Significance was determined by Friedmann test and Dunn´s Post-Hoc comparisons in A-B and by Wilcoxon matched pairs signed rank test in C (*p<0.05; **p<0.01 ***p<0.001;****p<0.0001). Only significance between samples is indicated. Numbers indicate patient-IDs.

7.7.3.3 Cytotoxic state of CTL in TIL is defined by perforin expression

In addition to analyzing the individual expression of perforin and granzyme B, the co-expression within CTL (T-bet^{high}/Eomes$^{\pm}$) CD8^{+} T cell subset was assessed on single cell level (figure 38). Examining the dot-plots (figure 38 A), it was observed that in all TIL perforin^{+} cells without granzyme B did not exist; perforin was always co-expressed with granzyme B, while granzyme B was also found in cells that did not express perforin. Next, the frequency distribution of double negative, double positive and single granzyme B^{+} cells among gated CTL (CD8^{+}T-bet^{high}/Eomes$^{\pm}$) was calculated (figure 38 B). With regard to the perforin^{+}granzyme B^{+} double positive cells, two groups were identified with high and low frequency. The frequency of perforin^{+}granzyme B^{+} CTL was defined by the perforin expression, as illustrated by identical values obtained from gating on the perforin^{+}granzyme B^{+} double positive or perforin^{+} single positive (calculated percentages without considering the granzyme B co-staining) CTL. Two groups of patients were also identified based on the perforin^{-}granzyme B^{+} subset, whereby the frequencies of these T cells mostly inversely correlated with the frequency of the double positive perforin^{+}granzyme B^{+} cells. Double negative cells were low (beyond 40%) in all TIL.

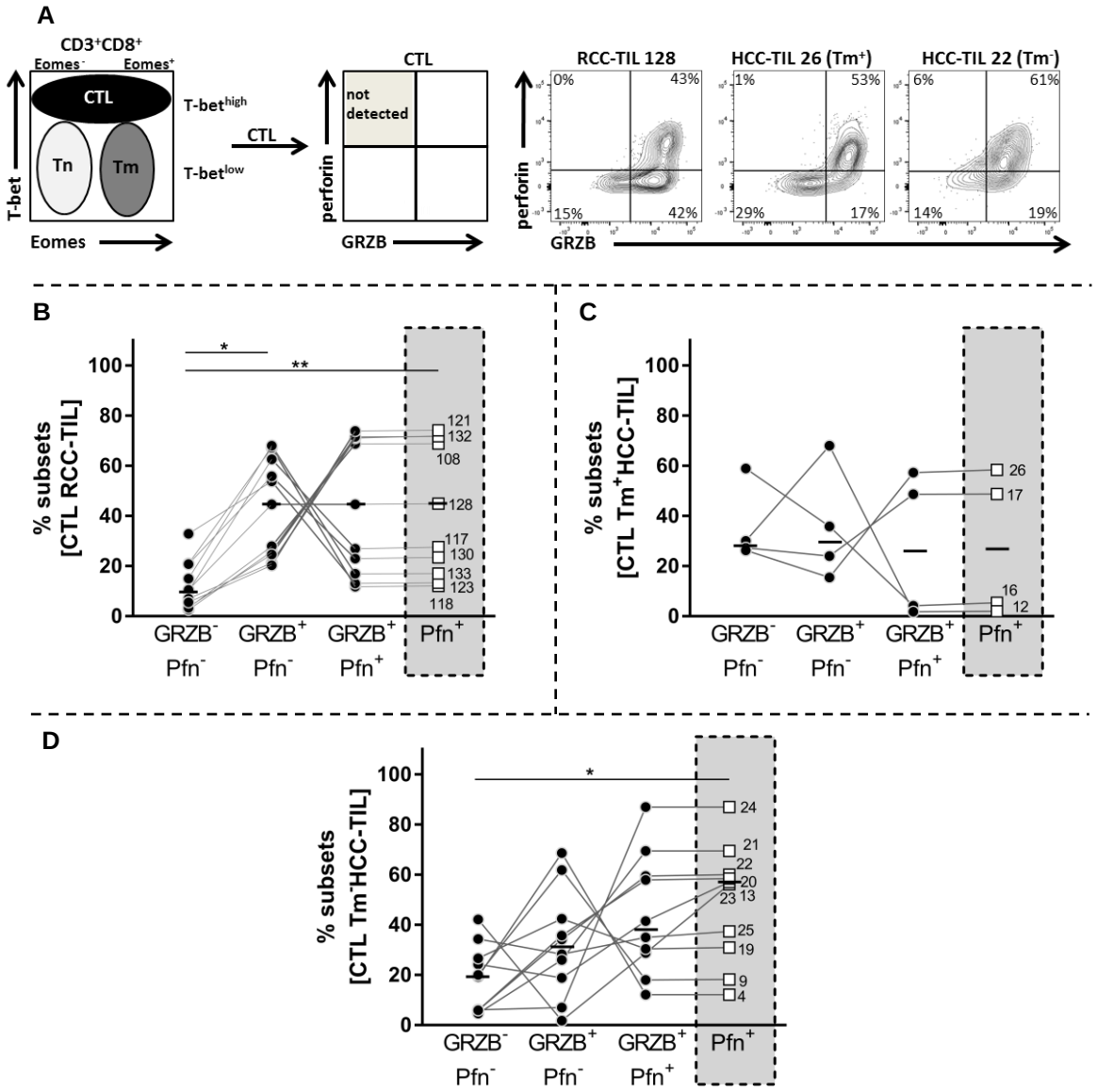

Figure 38: Co-expression of perforin and granzyme B in CTL of RCC-TIL and Tm^+/Tm^-HCC-TIL
Samples were stained for flow cytometry (table 21, see p. 107).A: Gating strategy and exemplary dot plots to determine combinations of perforin (Pfn) and granzyme B (GRZB) in CTL of RCC-TIL, Tm^+ and Tm^-HCC-TIL. B-D: Graphs summarize calculated percentages of Pfn and GRZB in CTL of RCC-TIL (C), Tm^+HCC-TIL (D) and Tm^-HCC-TIL (E). Highlighted by a grey box are the calculated percentages of Pfn^+ CTL without considering the GRZB co-staining. One symbol represents one patient, lines connect combinations from the same individual. Significance was statistically determined by Friedmann test and Dunn´s Post-Hoc comparisons (*p<0.05; **p<0.01; ***p<0.001; ****p<0.0001). If not indicated differently, differences between samples were not significant. Numbers indicate patient-IDs.

It was previously observed (figure 36, see p. 111), that CTL had low, but varied expression levels of PD-1. Now, a possible connection between expression of perforin or granzyme B and PD-1 in pregated T-bet^{high}/$Eomes^{\pm}$ $CD8^+$ (CTL) was addressed. An overlay of the mean fluorescence intensity of PD-1 on pregated perforin and granzyme B dot plots of T-bet^{high}/$Eomes^{\pm}$ $CD8^+$ (CTL) TIL visualized that highest PD-1 intensities were found in the $perforin^-granzyme\ B^-$ subset (figure 39). Calculated percentages of $PD\text{-}1^+$ were lowest in $perforin^+granzyme\ B^+$ cells compared with $perforin^-granzyme\ B^-$ or $perforin^-$

granzyme B^{+} subsets. For comparison, the total percentages of PD-1 of T-bet^{high}/Eomes$^{\pm}$ CTL without consideration of perforin and granzyme B subsets are shown in the grey box. These values are those shown in figure 37 (see p.113).

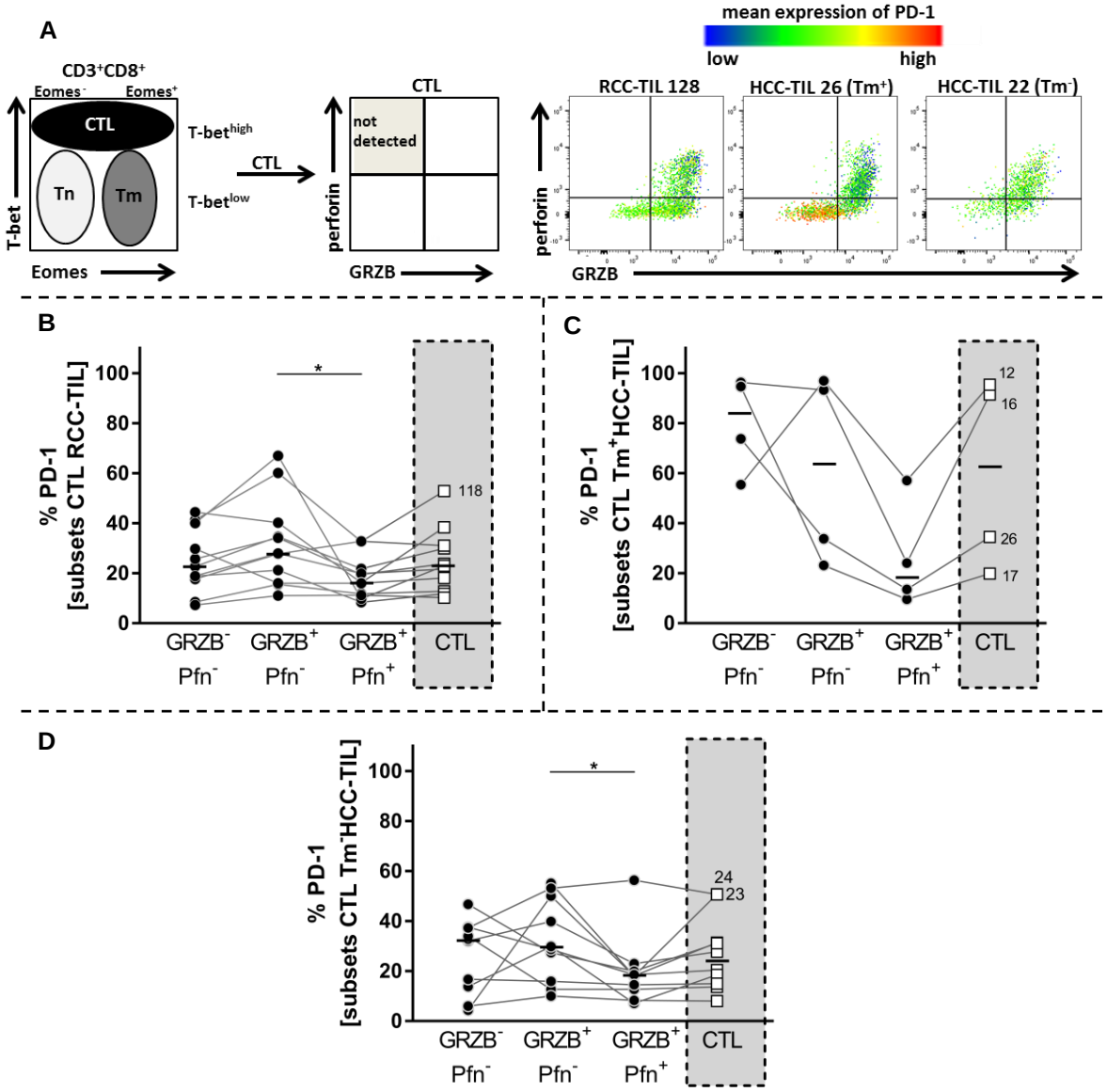

Figure 39: Percentages of PD-1 in perforin and granzyme B combinations of CTL in RCC-TIL and Tm^{-}/Tm^{+}HCC-TIL

Samples were stained for flow cytometry (table 21, see p. 107). A: Gating strategy and exemplary dot plots to determine combinations of perforin (Pfn) and granzyme B (GRZB) in pregated CTL (T-bet^{high}/Eomes$^{\pm}$) of RCC-TIL and Tm^{+}/Tm^{-}HCC-TIL. Mean expression of PD-1 is overlaid by color gradient: blue and green represent low expression whereas high expression is indicated by orange and red. B-D: Graphs summarize calculated percentages of PD-1 in combinations of Pfn and GRZB in CTL of RCC-TIL (B), Tm^{+}HCC-TIL (C) and Tm^{-}HCC-TIL (D). Highlighted by a grey box are percentages of total PD-1 in CTL without considering combinations of Pfn and GRZB. One symbol represents one patient or healthy donor, lines connect samples from the same individual, horizontal lines indicate median of one subset and significance was statistically determined by Friedmann test and Dunn´s Post-Hoc comparisons (*p<0.05; **p<0.01; ***p<0.001; ****p<0.0001). If not indicated differently, differences between samples were not significant. Numbers are patient-IDs.

7.7.3.4 Frequency analysis of perforin and granzyme B co-expression in $CD8^+$ TIL

The previous analysis indicated that TIL harbor $CD8^+$ TIL that co-express perforin and granzyme B (perforin$^+$granzyme B^+) which might represent CTL with tumor killing capacity. $CD8^+$ T cells being perforin$^-$ but granzyme B^+ were also observed and might correspond to a senescent (84,85) subtype.

The subset frequencies of perforin$^+$granzyme B^+ and perforin$^-$granzyme B^+ cell were determined for $CD8^+$ TIL of each patient and RCC-TIL and HCC-TIL were compared (figure 40).

RCC-TIL harbored more perforin$^-$granzyme B^+ as perforin$^+$granyzyme B^+ TIL, while HCC-TIL showed comparable frequencies of both, with no difference between Tm^-HCC-TIL and Tm^+HCC-TIL (figure 40). The comparison between RCC-TIL and HCC-TIL revealed similar low frequencies of perforin$^+$granyzyme B^+ $CD8^+$ T cells in both TIL, but significantly higher perforin$^-$granzyme B^+ $CD8^+$ T cells in RCC-TIL compared with HCC-TIL. This indicates a stronger cytotoxic capacity for HCC-TIL, consistent with previous finding that the frequency of perforin is higher in HCC-TIL than in RCC-TIL (figure 24, see p 90).

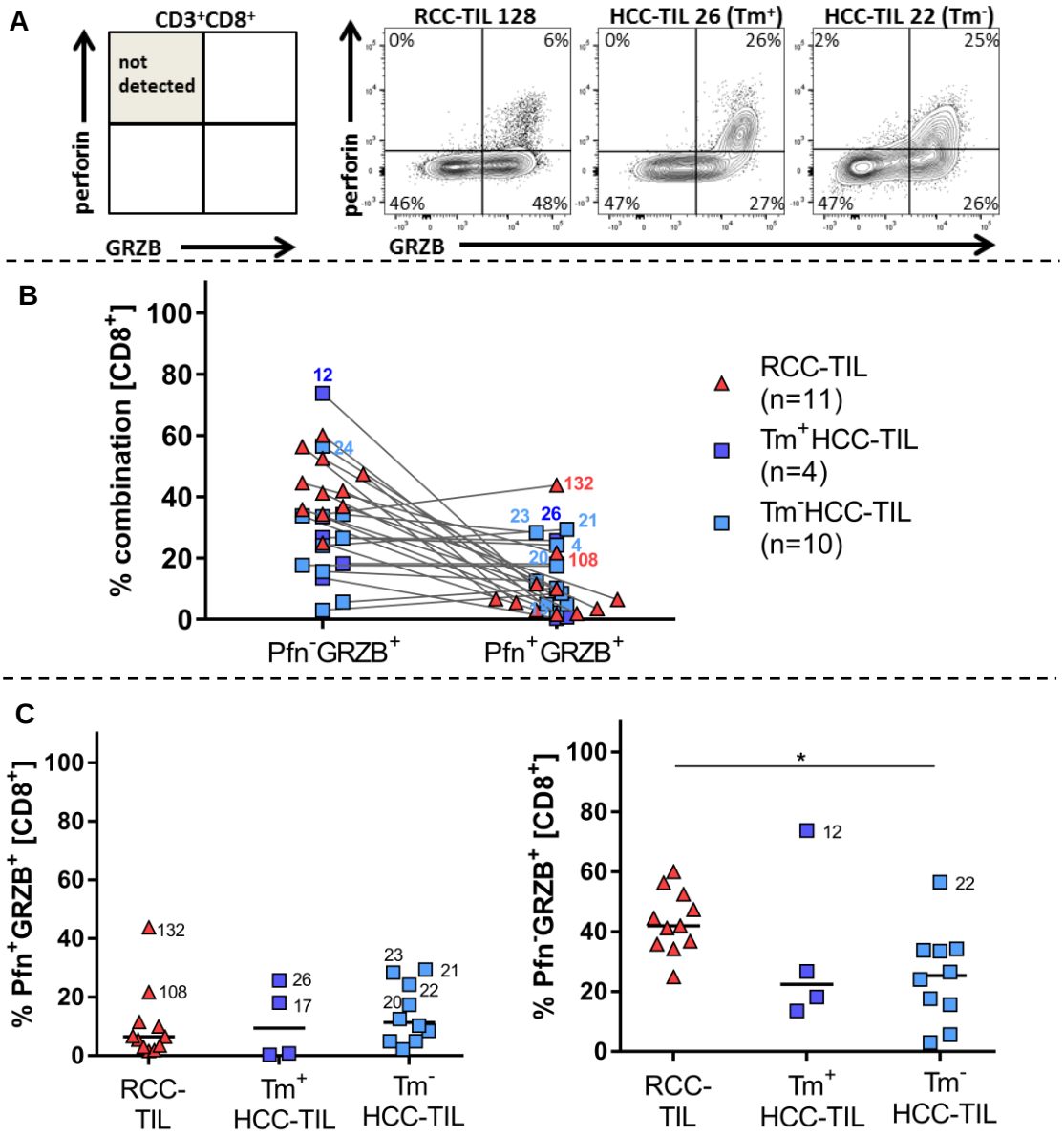

Figure 40: Perforin and granzyme B co-expression in CD8$^+$ TIL
Samples were stained for flow cytometry (table 21, see p. 107). A: Gating strategy and exemplary dot plots to determine combinations of perforin (Pfn) and granzyme B (GRZB) in pregated CD3$^+$CD8$^+$ T cells of RCC-TIL, Tm$^+$HCC-TIL, Tm$^-$HCC-TIL. B: Calculated percentages of Pfn$^-$GRZB$^+$ and Pfn$^+$GRZB$^+$ in CD8$^+$ RCC-TIL, Tm$^+$HCC-TIL and Tm$^-$HCC-TIL. One symbol represents one patient, lines connect subsets of one individual. C: Pfn$^-$GRZB$^+$ and Pfn$^+$GRZB$^+$ combinations are visualized separately to address significance between RCC-TIL, Tm$^+$HCC-TIL and Tm$^-$HCC-TIL by Kruskal-Wallis test and Dunn´s Post-hoc comparisons (*p<0.05; **p<0.01; ***p<0.001; ****p<0.0001). Only significance between samples is indicated. Numbers are patient-IDs.

7.8 Individual profiles of $CD8^+$ TIL based on anergic characteristics, PD-1, cytotoxic molecules and Ki-67

The above described analyses included markers that relate to T cell qualities. Subgroups designated as anergic ($FoxO1^+DGK\text{-}\alpha^{high}$), senescent ($PD\text{-}1^-perforin^-granzyme\ B^+$) (84,85), $PD\text{-}1^+$ non-lytic ($PD\text{-}1^+perforin^-granzyme\ B^-$ or $PD\text{-}1^+perforin^-granzyme\ B^+$), lytic state ($perforin^+granzyme\ B^+$ with or without PD-1) or proliferating state ($Ki\text{-}67^+$ with or without PD-1) were calculated as percentages of $CD8^+$ TIL of each individual patient and combined to form a "profile" of T cell quality (figure 41)

Group one (four RCC-TIL and two HCC-TIL) was dominated by high frequencies of $PD\text{-}1^+$ non-lytic T cells (range: 52% – 80%). The second group (five RCC-TIL and five HCC-TIL) was marked by medium percentages of $PD\text{-}1^+$ non-lytic T cells (range: 27% – 57%) and high frequencies of anergic T cells (range: 18% - 47%) with little lytic or proliferating subsets. The third group consisted of four HCC-TIL, characterized by high representation of $PD\text{-}1^+$ non lytic cells (range: 38% - 54%) and low representation of anergic $CD8^+$ cell subsets (range 1% - 11%) similar to group one. However, differently to group one, this group harbored a high fraction of lytic cells (range: 39% - 53%) and some proliferating subsets (range: 2% - 15%). The fourth group, consisting of one RCC-TIL and three HCC-TIL, was dominated by high proportions of lytic (range: 34% - 47%) and senescent (range: 18% - 39%) T cells subsets but had low fractions of the non-lytic $PD\text{-}1^+$ T cell subset.

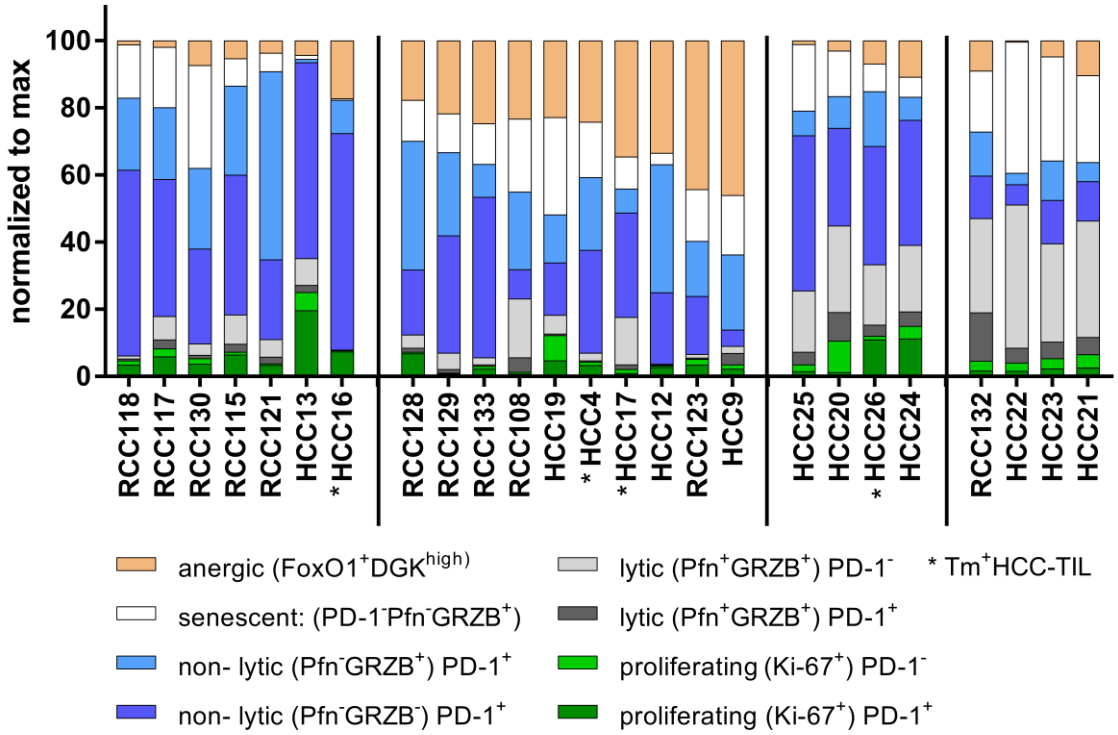

Figure 41: CD8$^+$ TIL profiles based on T cell anergy, PD-1, lytic state and proliferation
Tissue suspensions were stained and analyzed by flow cytometry. Percentages of different T cell subsets were calculated within CD8$^+$ T cells and defined as anergic (FoxO1$^+$DGK-α^{high}), senescent (PD-1$^-$perforin$^-$granzyme B$^+$), PD-1$^+$ non-lytic (PD-1$^+$perforin$^-$granzyme B$^-$ or PD-1$^+$perforin$^-$granzyme B$^+$), lytic (perforin$^+$granzyme B$^+$ with or without PD-1) or proliferating (Ki-67$^+$ with or without PD-1). Composition of the CD8$^+$ TIL of each patient is visualized by stacked bars, each subset is represented by a different color and the height of the bars represents percentages of one subset in gated CD8$^+$ TIL. Patients with similar percentages of T cell subsets were grouped together. GRZB: granzyme B. Pfn: perforin

8 Discussion

Immunotherapy is currently one of the highlights in cancer therapy (86) and tumor control can be achieved even in patients with metastatic progression who have failed other available therapeutic options (87). The currently most successful immunotherapy is directed against immune checkpoints like CTLA-4 or PD-1, which are co-inhibitory receptors expressed on the cell surface of T cells. In the tumor microenvironment, ligands of CTLA-4 or PD-1 are increased (50). They impair anti-tumor T cell function and blocking the interaction between immune checkpoints and their ligands leads to re-invigoration of T cells which were made unresponsive in the tumor microenvironment (32). Despite the success of checkpoint blockade, it remains unclear why only a subgroup of patients responds to this immunotherapy, demonstrating that other mechanisms beyond CTLA-4 or PD-1 checkpoints must exist.

This thesis aimed to further investigate modifications of TIL in the tumor microenvironment, focusing on TIL of clear cell renal cell carcinoma (ccRCC, RCC-TIL) and TIL of non-viral HCC (HCC-TIL). RCC and HCC form in the context of very different immunologic background: An inflammatory background of RCC development is not indicated though RCC is considered to be an immune responsive tumor as some patients responded to high-dose IL-2 or IFN-α (1–3) and TIL isolated from RCC tissues showed anti-tumor activity after cultivation *in-vitro* (4–6). On the contrary, HCC emerges most exclusively on an inflammatory background such as chronic viral infection, steatosis, non-alcoholic steato-hepatitis (NASH) or inflammatory conditions of alcoholic liver disease which develop in the context of an immune-tolerant milieu of the liver required to prevent overt reactivity to toxic agents and gut-delivered pathogens (63). These conditions ease tumor development and simultaneously hamper anti-tumor activity of HCC-TIL (7,60,61). Based on these different immunologic backgrounds of RCC-TIL and HCC-TIL, it was of interest to derive comparative data for TIL from these tumor entities. The knowledge of mechanisms of tumor immune escape is required to understand therapy responses and to rationalize strategies to improve outcome of immunotherapy.

8.1 Hypo-responsiveness of $CD8^+$ RCC-TIL and HCC-TIL

It was observed on a global perspective that the infiltrate in HCC and RCC was dominated by T cells. Interestingly, in HCC and less prominent in RCC, there were some patients with low frequencies of T cells correlating with high percentages of monocytes/macrophages. An accumulation of tumor-associated macrophages (TAMs)

has been associated with poor prognosis (88) and M2 polarized macrophages were described to sustain tumor progression (89). Depletion of TAMs in a mouse model led to increased cytotoxic T cell response of TIL (89). It would be of interest or future analysis to define the characteristics of the monocytes/macrophages in HCC and RCC such as their polarization and their impact on the infiltrated T cells. Among the infiltrating immune cells, $CD8^+$ TIL are of special interest because they can be highly specific against their antigen and can trigger apoptosis in targeted tumor cells by releasing cytotoxic proteins like perforin and granzyme B (10). Both RCC-TIL and HCC-TIL harbored $CD8^+$ TIL and the ratio to $CD4^+$ TIL was balanced except for one RCC-TIL (RCC-TIL 123) and four HCC-TIL (HCC-TIL 13, HCC-TIL 17, HCC-TIL 19, HCC-TIL 21) which had a higher CD4:CD8 ratio. A potential association with prognosis cannot be deduced from this analysis since no follow-up reports are available for the analyzed patient cohorts.

The presence of $CD8^+$ in the absence of tumor growth control indicates functional impairment of the $CD8^+$ TIL. Indeed, functional unresponsiveness of $CD8^+$ RCC-TIL to anti-CD3 stimulation with suppressed IFN-γ production and lytic granule exocytosis has been reported for $CD8^+$ TIL in numerous studies including HCC-TIL (90,91) and RCC-TIL (4,40,69). However, the underlying mechanisms that lead to functional unresponsiveness of $CD8^+$ TIL have been neither fully understood in RCC-TIL nor in HCC-TIL. In this thesis, dysfunction in degranulation and IFN-γ production was shown for $CD8^+$ RCC-TIL and HCC-TIL which responded equally poor to anti-CD3 stimulation. Providing additional co-stimulation through CD28 did not improve the situation. Stimulation with PMA/I increased the percentages of T cells with function in RCC-TIL and HCC-TIL, but the values remained lower compared with activated T cells, indicating that RCC-TIL and HCC-TIL were in a non-responsive state that cannot be completely overcome by PMA/I stimulation (see discussion below). The responsive profile of $CD8^+$ RCC-TIL and HCC-TIL upon anti-CD3 stimulation was dominated by degranulating T cells followed by T cells that secreted IFN-γ and very few poly-functional ($CD107a^+IFN\text{-}\gamma^+$) T cells. Anti-CD3/CD28 stimulation did not change the profile while PMA/I stimulation did not only lead to more responsive T cells but also changed the profile with an increased stimulation of IFN-γ secretion, resulting in more poly-functional T cells in both TIL. PMA is a direct activator of PKC (70), leading to increased levels of active NFκB and subsequent cytokine (IFN-γ) production (10). Ionomycin (Iono) is a DAG analogon (70). They activate Ca^{2+} influx, NFAT associated transcription and the ERK-pathway leading to degranulation (10). The targets of PMA/I are downstream of the proximal TCR signaling and therefore PMA/I should overcome deficits in the proximal signaling cascade, e.g. impaired signal transduction of Lck or PLC-γ (92). A blockade in the signaling cascade downstream of PMA/I activation is

evident in $CD8^+$ RCC-TIL and HCC-TIL because they responded to PMA/I treatment with increased $CD8^+$ T cells with function but their frequencies were beyond those of activated T cells. These obstructions might relate to deficits in the PI3K signaling, as previous findings have reported impaired degranulation upon stimulation with PMA/I in PI3Kδ knockout $CD8^+$ T cells (91). Impaired function of PI3K in TIL might be caused by PD-1 signaling (34) or low levels of DAG which might occur in a situation of DGK-α overexpression as described in RCC-TIL (40) and also found in some RCC-TIL and HCC-TIL in this study. Since TIL showed evidence that they cannot fully respond with degranulation and IFN-γ production to PMA/I stimulation, defects in the downstream signaling pathways were expected. Downstream targets and pathways, schematically delineating in figure 42, include the PKCθ and the AKT-pathway, both leading to NFkB, and communication to the mTOR- and ERK-pathways.

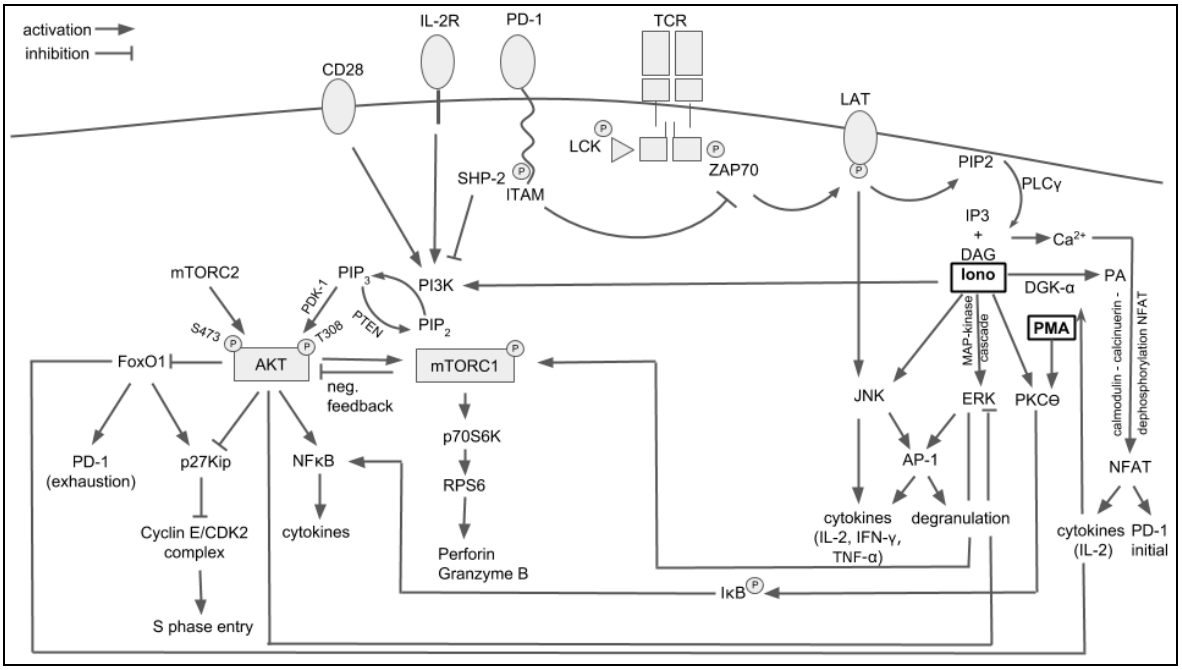

Figure 42: TCR signaling, its cross-talk to AKT and mTOR pathways and impacts of PMA/I
CD28: co-stimulatory receptor. IL-2R: receptor of IL-2. PD-1: co-inhibitory receptor. TCR: T cell receptor. LCK, Fyn: kinases of the Src family. ITAMs: immunoreceptor tyrosine-based activation motif. ZAP70: tyrosinase-protein kinase ZAP70. LAT: linker of activated T cells. PIP_2: phosphatidyl-inositol-4,5-bisphosphat. IP_3: inositol-1,4,5-trisphosphat. PLC-γ: phosphor lipase C- γ. DAG: diacylglycerol. DGK-α: diacylglycerolkinase-α. PA: phosphatidic acid. NFAT: nuclear factor of activated T cells. ERK: extracellular signal-related kinase. AP-1: activating protein 1. JNK: c-Jun N-terminale kinase. PI3K: phosphoinositide-3-kinase, PIP_3:phosphatidyl-inositol-3,4,5-trisphosphat. PTEN: phosphatase and Tensin homolog. PDK-1: phosphoinositide dependent kinase-1. AKT: protein kinase B. mTORC1/C2: mammalian target of rapamycin complex 1/2. FoxO1: forkhead box protein 1. $p27^{kip1}$: CDK inhibitor. CDK2: cylin dependent kinase 2. NFκB: nuclear factor "kappa light chain" of activated B cells. p70S6K: p70 ribosomal protein kinase S6. rpS6: ribosomal protein S6. IκB: inhibitor of NFκB. PMA: phorbol-12-myristate-13-acetate. Iono: ionomycin

Indeed, it was observed that the AKT-pathway was poorly in T cells of TIL demonstrated by low percentages of pAKT(S473), whereby RCC-TIL seemed most strongly suppressed while some $CD3^+$ HCC-TIL (HCC-TIL 4, HCC-TIL 12, HCC-TIL 13, HCC-TIL 16, HCC-TIL 17) showed evidence that the AKT-pathway was activated to some extent. TIL

with AKT phosphorylation might be regarded as T cells with functional PI3K signaling, allowing stronger response to PMA/I stimulation. Actually, two HCC-TIL (HCC-TIL 4, HCC-TIL 17) with higher percentages of pAKT(S473) had also higher frequencies of T cells with function upon PMA/I stimulation. Unfortunately, this study is restricted because simulation assays were only performed for few TIL and these studies have to be extended to include more TIL, providing further evidence for a possible association between functional T cell response and the AKT-pathway.

Markers that allow prediction of functional responsiveness of T cells would be attractive tools as they would allow to judge the quality of TIL and the immune state of patients without the need of functional assays. Proliferating TIL have been associated with good prognosis (72), and here it was observed that T cells responding to anti-CD3 stimulation were enriched among Ki-67$^+$ CD8$^+$ T cells in RCC-TIL and in some HCC-TIL. Moreover, it has been proposed that CD28 expression on T cells might predict the response to checkpoint therapy (93). Human T cells lose the ability to receive co-stimulation during differentiation to effector T cells (76,77) and concurrently cannot receive co-stimulation for prolonged effector activity. Thus, it is conceivable that T cells in TIL that maintained CD28 expression might be of better quality. However, in this thesis no enrichment of T cells with function in the CD28$^+$ versus the CD28$^-$ CD8$^+$ T cell population was observed. This might be due to low sample numbers. Next to markers that might be positively associated with T cell quality, there are also markers such as PD-1 which are related to impaired T cell function (73–75). Although there was a slight reduction of T cells with function among the PD-1$^+$CD8$^+$ population in TIL, the difference to PD-1$^-$CD8$^+$ subset was not significant. The reason for the lack of association can be due to the fact, that PD-1 is not exclusively expressed on T cells with impaired function (73–75), but is also expressed on activated T cells (81). The combination of PD-1 and other co-inhibitory receptors is required to identify the true dysfunctional T cells (42) of which only few were detected in CD8$^+$ RCC-TIL and HCC-TIL.

Based on the observation that Ki-67 and the AKT-pathway allow some prediction of T cell quality, the cell cycle was further considered being closely connected to Ki-67 and AKT (24–27), as shown in figure 42 (see p. 123). A connection between the AKT-pathway and the cell cycle was evident in TIL since pAKT(S473); in the case when pAKT(S2473) was detected, it was not found in combination with cell cycle inhibitor p27^{kip1} in RCC-TIL and HCC-TIL. Thus, an active AKT-pathway might sustain cell cycle progression in TIL, according to previous literature findings (24–27). Cyclin E is connected to cell cycle entry (26,27), but in most RCC-TIL and HCC-TIL a relation between pAKT(S473) and cyclin E was not found, as positivity of pAKT(S473) was detected in combination with both cyclin

E^{low} or cyclin E^{high}. These data could indicate that activation of the AKT-pathway is not sufficient to always lead to cell cycle progression. However, it needs to be taken into account that analysis of this thesis represents “snap-shots” catching TIL in a certain state and can, therefore, not address the dynamics and kinetics of the signaling cascades. Thus, observed high levels of cyclin E could indeed have been induced by pAKT(S473), but the phosphorylation of AKT might already have been degraded. Additionally, T cell subsets with nuclear pAKT(S473)$^+$cyclin E^{high} cannot be detected by the experimental setting using “Perm buffer III” (BD) which is required to preserve the phosphorylation state but does not permeabilize the nucleus. However, activated AKT is known to translocate into the nucleus to phosphorylate its nuclear targets 20 min – 30 min after its activation (94) which is followed by subsequent ubiquitin-mediated degradation of pAKT (95).

Considering that perforin and granzyme B are central mediators of tumor cell killing, these cytotoxic molecules also need to be considered when describing T cell quality. The paucity of perforin as described for $CD8^+$ RCC-TIL (40,96) and HCC-TIL (97) and also found in this thesis, can be considered as a nearly universal hallmark of $CD8^+$ TIL. The mechanism which regulate perforin expression are not fully elucidated, but a connection of the mTOR-pathway to perforin expression has been described (30). In contrast to the the predominance of perforin negativity in $CD8^+$ TIL, more than 80% of TIL were pmTOR(S2448), except for five HCC-TIL and five RCC-TIL, which had lower percentages. However, rpS6, the downstream target of mTOR (29), was much less phosphorylated as mTOR in RCC-TIL and HCC-TIL, hinting to an interrupted mTOR-pathway. The analysis between pmTOR(S2448), prpS6(S244) and perforin revealed that T cells positive for perforin were also positive for pmTOR(S2448) as well as for prpS6(S244), indicating that perforin regulation might require that mTOR is connected to the downstream activation of rpS6, which has until now not been described. Considering the combined expression of pmTOR(S2448) and prpS6(S244), two groups of TIL with either high or low frequencies of pmTOR(S2448)$^+$prpS6(S244)$^+$ were identified. Five HCC-TIL (HCC-TIL 4, HCC-TIL 12, HCC-TIL 13, HCC-TIL 16, HCC-TIL 17) having high percentages of pmTOR(S2448)$^+$prpS6(S244)$^+$ cells with four of these five TIL (HCC-TIL 4, HCC-TIL 12, HCC-TIL 13, HCC-TIL 17) having high frequencies of perforin compared with the rest of the HCC cohort. Interestingly, those HCC-TIL (HCC-TIL 4, HCC-TIL 12, HCC-TIL 13, HCC-TIL 17) were identified to harbor elevated frequencies of pAKT(S473) and cyclin E (see discussion above), too. None of the analyzed RCC-TIL showed evidence of active AKT and high levels of cyclin E an perforin$^+$ T cells were nearly absent in RCC-TIL, suggesting deeper suppression of the intracellular signaling in RCC compared with HCC.

8.2 Different types of unresponsiveness in $CD8^+$ RCC-TIL and HCC-TIL

The lack of perforin and also functional unresponsiveness are hallmarks of TIL. While unresponsiveness is commonly observed, the underlying mechanisms could be different and manifold. Various types of unresponsiveness have been described, including quiescence, anergy, exhaustion, tolerance or senescence. Quiescent T cells might not have been activated or been excluded from antigen and are at the quiescent G_0 phase of the cell cycle. Cell cycle analysis of TIL revealed that RCC-TIL and HCC-TIL were mainly in G_0, G_2 or M phase of the cell cycle. Only four HCC-TIL (HCC-TIL 4, HCC-TIL 12, HCC-TIL 13, HCC-TIL 17) had higher percentages of T cells being in the S phase of the cell cycle. Interestingly, a connection between positivity of pERK(T202/Y204) and cell cycle progression was found as T cells with pERK(T202/Y204)$^+$ were enriched for T cells in early S/late G^1, S or late S phase compared with pERK(T202/Y204)$^-$ subsets. This demonstrated, that proliferating TIL associated with good prognosis (72) also might be capable to degranulate due to the positivity of pERK(T202/Y204). Considering that phosphorylation of ERK is related to the capacity of T cells to degranulate (10), it is interesting that the cell cycle state might also control T cell function. Irreversible cell cycle arrest has also been associated with the hypo-responsive phenotype of senescence (98). Although senescence has been originally found with aging, it can also develop in the context of persisting antigen stimulation as present in the tumor (99) or in chronic viral infections (85). The extensive turnover leading to irreversible cell cycle state in senescent T cells is in line with the loss of cytotoxic molecules, and the development of perforin$^-$ granyzme B^+ T cells have been associated with a senescent phenotype in HIV-specific $CD8^+$ T cells (84,85). Perforin$^-$granzyme B^+ T cells were detected in $CD8^+$ TIL, in particular in RCC-TIL and less in HCC-TIL, indicating a different microenvironment of RCC and HCC that drives TIL into different developmental stages. Senescent T cells were also associated with positivity of PD-1 as PD-1 expression was increased in early stage chronic lymphatic leukaemia (CLL) patients who had also high levels of senescent T cells (100). However, PD-1 expression has not been identified as surface marker on senescent T cells, which could be achieved by flow cytometry, characterizing senescent T cells as $CD57^+CD28^-CD27^-$KLRG-1^+ (99,100) and examining co-expression of PD-1. This would further help to distinguish if PD-1^+perforin$^-$granzyme B^+ are senescent T cells.

Another type of unresponsiveness has been described as T cell anergy, defined by incomplete T cell activation without co-stimulation. The initial description of T cell anergy addressed the function unresponsive state of $CD4^+$ T cells (35). It was found our recently, that $CD8^+$ RCC-TIL (40) also showed hallmarks of anergic T cells such as upregulated DGK-α, subsequent degradation of DAG and reduced levels of phosphorylated AKT and

ERK (18,35). In both RCC-TIL and HCC-TIL, a group of TIL was identified, showing signs of an anergic T cell state by increased expression of DGK-α compared with corresponding NIL. DGK-α strictly correlated with FoxO1 in $CD8^+$ RCC-TIL and HCC-TIL. FoxO1 has been suggested as a transcription factor for DGK-α (18). The results of the TIL analysis further support this finding and indicate FoxO1 activity as one mechanism causing DGK-α expression.

FoxO1 is also considered to be the transcription factor for PD-1. In this thesis, however, PD-1 positivity was not exclusively related to $FoxO1^+$ cells, and PD-1 was also found in FoxO1- T cell populations. A possible explanation is, that different stages of PD-1 expression are regulated by different transcription factors; FoxO1 is thought to drive sustained PD-1 expression (21) whereas initial or temporary PD-1 expression upon T cell activation is induced by NFAT (81). Thus $PD\text{-}1^+$ T cells in $FoxO1^-$ subsets might not be those with sustained PD-1 expression and considered to represent the exhausted T cell subset but might rather correspond to activated T cells. The different PD-1 states are not distinguishable in this thesis as NFAT was not analyzed and further experiments are necessary to elucidate the relation of NFAT and PD-1+ T cells in FoxO1- subsets and to discriminate potentially exhausted from activated T cells. It is interesting to note, that the expression and transcriptional activity of FoxO1 is regulated by AKT-pathway, whereby activation of AKT leads to suppression of FoxO1 activity (21). Thus, the lack of AKT activation as observed in RCC-TIL and HCC-TIL may be the underlying cause for FoxO1 activity that drives DGK-α expression, the development and manifestation of anergy and possibly also exhaustion in TIL.

Exhaustion indicates a T cells state which is functionally poor. PD-1 expression is often used as surrogate for exhaustion (41,42). It is now increasingly appreciated that PD-1 is an imprecise marker to describe exhausted T cells because PD-1 is also expressed upon T cell activation (81). A better description of exhausted T cells can therefore be achieved by co-expression of multiple co-inhibitory receptors. In this thesis, co-expression of PD-1 and LAG-3 was addressed. However, very few T cells co-expressing both markers were found. The low percentages of TIL being $PD\text{-}1^+LAG\text{-}3^+$ might suggest that TIL are not exhausted. These findings need to be treated cautiously as only one additional co-inhibitory receptor (LAG-3) was evaluated and other co-inhibitory inhibitory receptors like TIM-3 and CTLA-4 were not analyzed. Interestingly, positivity of Ki-67 was mainly found in $PD\text{-}1^+LAG\text{-}3^+$ subsets in both RCC-TIL and HCC-TIL. As Ki-67 indicates a proliferative state, the $PD\text{-}1^+LAG\text{-}3^+$ T cells were exhausted but still maintained proliferation and might possess the potential to become re-invigorated after checkpoint blockade, as has been suggested (41,42). In previous studies, T cell exhaustion has not only been addressed by

co-inhibitory receptor expression, but also by transcription factors T-bet, Eomes, and PD-1. T cells being T-bet^{low}/Eomes^{+} were identified in all RCC-TIL, but HCC-TIL were divided into two groups: One group had (Tm^{+}HCC-TIL) and the second group did not have (Tm^{-}HCC-TIL) T-bet^{low}/Eomes^{+} T cells. Further analysis revealed that the T-bet^{low}/Eomes^{+} (Tm-like) T cell subset had the highest expression levels of PD-1 compared with the T-bet^{high}/Eomes$^{-/+}$ (CTL) and T-bet$^{-/low}$/Eomes^{-} (naïve) subsets, which is in line with findings that T-bet inversely and Eomes directly correlated with PD-1 expression (101). The T-bet^{low}/Eomes^{+}/PD-1^{+} subset could resemble the T-bet^{high}/Eomes^{low}/PD-1^{low} subset of exhausted CD8^{+} T cells described in literature as more responsive to anti-PD-L1 reinvigoration (42,82). This subset was absent in the larger subgroup of Tm^{-}HCC-TIL, and present in all RCC-TIL and Tm^{+}HCC-TIL. PD-1^{+} T cells were also enriched in the Tn-like T-bet^{low}/Eomes^{-} subsets of RCC-TIL and Tm^{+}HCC-TIL, suggesting that this population does not relate to naïve T cells, but to T cells that are antigen-experienced.

Interestingly, PD-1 expression levels in Tm^{-}HCC-TIL were found infrequently and equally distributed over the T-bet^{low}/Eomes^{-} (naïve) and T-bet^{high}/Eomes$^{-/+}$ (CTL) subsets. TIL of these patients might not have experienced antigen and might therefore not have been activated. Further research is necessary to reveal why CD8+ T cells had no antigen contact in these tumors. Mechanisms could be that i) the CD8^{+} TIL lack cognate TCRs for presented antigens, ii) antigen presentation could be disturbed and iii) tolerogenic mechanisms of the liver and immune suppressive cell types like regulatory T cells (90,91) or MDSCs (myeloid-derived suppressor cells) (91) could prevent activation. Indeed, some Tm^{-}HCC-TIL (HCC-TIL 19, HCC-TIL 20, HCC-TIL 22, HCC-TIL 23, HCC-TIL 24) had low percentages of T cells but high percentages of monocytes/macrophages.

Perforin^{+} T cells were mainly found among the T-bet^{high}/Eomes$^{-/+}$ (CTL) subset in all RCC-TIL and HCC-TIL, independently if HCC-TIL were Tm^{-} or Tm^{+}. In RCC-TIL, two groups with high and low percentages of perforin^{+}granzyme B^{+} in CTL were identified. RCC-TIL with a high percentage of perforin^{+}granzyme B^{+} in CTL were also those TIL that had high pmTOR(S2448)$^{+}$prpS6(S244)$^{+}$, emphasizing the connection between an active mTOR-pathway and perforin. Tm^{+}HCC-TIL also differed in perforin^{+}granzyme B^{+} cells, but a connection to increased percentages of pmTOR(S2448)$^{+}$prpS6(S244)$^{+}$ was not evident as perforin^{+}granzyme B^{+} cells were also high in TIL with low percentages of pmTOR(S2448)$^{+}$prpS6(S244)$^{+}$ cells. However, Tm^{+}HCC-TIL with pmTOR(S2448)$^{+}$ prpS6(S244)$^{+}$ but low perforin^{+}granzyme B^{+} CTL had high levels of PD-1. These cells might have lost perforin due to extensive activation and degranulation. On the other hand, Tm^{+}HCC-TIL having high percentages of perforin^{+}granzyme B^{+} CTL had low PD-1. They might not have been activated and thereby still harbor perforin and granzyme B.

8.3 "Best-fit" treatments based on CD8$^+$ TIL profiles

Based on the observed types of hypo-responsiveness, proliferation and lytic state (defined by perforin and granzyme B), a profile was assembled for each TIL. TIL of each individual patient showed a unique composition. Some TIL were dominated by non-lytic T cells, other TIL displayed a combination of non-lytic and anergic T cells, whereas others showed a combination of non-lytic and lytic T cells or had fewer non-lytic but mostly lytic and senescent T cells. Interestingly, there was only one profile (non-lytic/lytic) that was only represented by HCC-TIL; all other profiles were seen in RCC-TIL as well as in HCC-TIL. Should it turn out that a particular TIL profile correlates with a particular treatment response, the patient selection for the therapy will no longer be based on the tumor entity

Based on immune characteristics predominating in the TIL, "best-fit" treatments may rationally be selected, as some treatment options are currently available for some T cell states whereas for other types of unresponsiveness further research is necessary. Checkpoint inhibitors are in clinical use and response rates are around 25% for different tumor entities (52,64). Based on the TIL profile one might predict that those patients are likely to respond to checkpoint inhibitors who have PD-1$^+$ TIL with a lytic component. If TIL lack the lytic component, additional activation of TIL to induce perforin might be indicated. IL-2 is a potent inducer of perforin (102), but systemic toxicities currently limit its broader clinical application. If TIL contain a strong myeloid component (as observed for HCC-TIL 22 and HCC-TIL 23), PD-1 blockade might fail due to continued T cell inhibition by myeloid cells. A possible improvement might be achieved by combined therapy targeting the myeloid compartment.

A profile that contains T cells with anergic features (FoxO1$^+$DGK-α^{high}) might require re-invigoration by inhibition of DGK-α. DGK-α inhibition has been demonstrated to improve T cell function in *in-vitro* assays (40), however, drugs inhibiting DGK-α for clinical use are currently not available.

An interesting profile is mostly found in HCC-TIL, and is composed of T cells with lytic state, however, very low positivity of PD-1 and indication of senescence. Here it appears that T cells activation was impaired as T cells might be excluded from direct tumor contact or tumor cells may not present antigens. Further information is required, e.g. histological examination could help to define the position of the T cells in the tumor tissue. If an excluded state is observed, measures should be directed to enhance recruitment. Clinical success has been observed in combination therapies of checkpoint blockers and Bevazizumab in RCC-TIL (103), demonstrating enhanced infiltration. Successful targeting of senescence in leukocytes has not yet been reported, but some promising results with

senolytic drugs were obtained such as quercetin in senescent human endothelial cells (104).

9 Abbreviations

AKT	protein kinase B
AP-1	activating protein 1
APC	antigen presenting cell; allophycocyanin (fluorochrome)
APC-e Fluor 780	allophycocyanin e-Fluor 780
BCLC staging	Barcelona clinic liver cancer staging
BCR	B cell receptor
BV421	brilliant violet 421
ccRCC	clear cell renal cell carcinoma
CDK	cyclin dependent kinase
CLL	chronic lymphatic leukaemia
CTL	cytotoxic lymphocytes
CTLA-4	cytotoxic T cell associated protein 4
DAG	diacylglycerol
DC	dendritic cell
DGK-α	diacylglycerol kinase α
EDTA	ethylenediaminetetraacetic acid
Eomes	Eomesodermin
ERK	extracellular signal-related kinase
FACS	fluorescence activated cell corting
FBS	fetal bovine serum
FDA	Food and Drug Administration
FI	fluorescence intensity
FITC	fluorescein isothiocyanate

FMO	fluorescent minus one
FoxO1	forkhead box protein 1
GIT	gastro intestinal tract
GPC-3	glypican-3
HBSS	Hanks balanced salt solution
HBV	hepatitis B virus
HCC	hepatocellular carcinoma
HCV	hepatitis C virus
HIV	human immunodeficiency virus
HS	human serum
HTCR	human Tissue and Cell Research (HTCR) Foundation
ID	identification
IFN-α	interferon α, interferon β
IFN-β	interferon β
IP_3	inositol-1,4,5-trisphosphate
ITAMs	immunoreceptor tyrosine based motifs
IκB	inhibitor of NFκB
JNK	c-Jun-N-terminale kinase
KIR	killer cell immunoglobulin like receptors
KLR	killer cell lectin-like receptors
LAG-3	lymphocyte activation gene - 3
LAT	linker of activated T cells
LSECs	liver sinusoidal endothelial cells
MAP kinase	mitogen-activated protein kinase
MDSC	myeloid derived suppressor cells

MFI	mean fluorescent intensity
MHC, pMHC	major histocompatibility complex, protein major histocompatibility complex
mTOR C1/C2	mammalian target of rapamycin complex 1/complex 2
NASH	non-alcoholic steatohepatitis
NFAT	nuclear factor of activated T cells
NFκB	nuclear factor of κ light chain of activated B cells
NIL	infiltrating leukocytes from non-tumor harboring tissues
NK cells	natural killer cells
nv-HCC	non-viral hepatocellular carcinoma
p70S6	ribosomal protein kinase S6
PA	phosphatidic acid
PAMP	pathogen-associated molecular pattern
PB	pacific blue
PBMC	peripheral blood mononuclear cells
PBS	phosphate buffered saline
PCA	principal component analysis
PD-1	programmed cell death protein - 1
PDK-1	phosphoinositide-dependent kinase 1
PE	phycoerythrin
PE-Cy7	phycoerythrin–cyanin 7
PerCP-Cy5.5	peridinin-chlorophyll-cyanine 5.5
PI3K	phosphoinositide-3-kinase
PIP_2	phophatidyl-inositol-4,5-bisphophate
PIP_3	phosphatidyl-inositol-3,4,5-trisphopate
PKC-θ	protein kinase c-θ

PLC-γ	phospholipase C- γ
PMA/I	phorbol-12-myristate-13-acetate/ Ionomycin
PMT	photomultiplier
PRR	pathogen recognizing receptor
PTEN	phosphatase and tensin homolog
pTNM staging	pathological tumor node metastasis staging
RCC	renal cell carcinoma
RFA	radiofrequency ablation
RPMI	Roswell Park Memorial Institute
rpS6	ribosomal protein S6
SEM	standard error of the mean
SH2	Src homology 2
TAA	tumor associated antigen
TACE	transarterial chemoembolization
TAMs	tumor-associated macrophages
T-bet	T box transcription factor
TCL	Tumor circulating lymphocytes
TCR	T cell receptor
TIL	tumor-infiltrating leukocytes
TIM-3	T cell immunoglobulin and mucin domain containing3
TLR	toll-like receptor
Tm	memory-like T cells
Tn	naïve T cells
TNF- α	tumor necrosis factor α
Treg	regulatory T cell

UICC	Union International Contre le Cancer
V450	violet 450
V500	violet 500

10 References

1. Geiger C, Nößner E, Frankenberger B, Falk CS, Pohla H, Schendel DJ. Harnessing innate and adaptive immunity for adoptive cell therapy of renal cell carcinoma. J Mol Med. 2009;87:595–612.

2. Vogelzang NJ, Stadler WM. Kidney cancer. Lancet (London, England). 1998;352:1691–6.

3. Reeves DJ, Liu CY. Treatment of metastatic renal cell carcinoma. Cancer Chemother Pharmacol. 2009;64:11–25.

4. Schendel DJ, Oberneder R, Falk CSC, Jantzer P, Kressenstein S, Maget B, et al. Cellular and molecular analyses of major histocompatibility complex (MHC) restricted and non-MHC-restricted effector cells recognizing renal cell carcinomas: J Mol Med. 1997;75:400–13.

5. Schendel, DJ Gansbacher, B, Oberneder, R Kriegmair M, Hofstetter A, Riehtmüller G and SO. Tumor-specific lysis of human renal cell carcinomas by tumor-infiltrating lymphocytes. I. HLA-A2-restricted recognition of autologous and allogeneic tumor lines. J immunol. 1993;151:4209–20.

6. Leisegang M, Turqueti-Neves A, Engels B, Blankenstein T, Schendel DJ, Uckert W, et al. T-cell receptor gene-modified T cells with shared renal cell carcinoma specificity for adoptive T-cell therapy. Clin Cancer Res. 2010;16:2333–43.

7. Makarova-Rusher O V., Medina-Echeverz J, Duffy AG, Greten TF. The yin and yang of evasion and immune activation in HCC. J Hepatol. European Association for the Study of the Liver; 2015;62:1420–9.

8. Gravitz L. Liver cancer. Nature. 2014;516:S1.

9. de Riese W, Goldenberg K, Allhoff E, Stief C, Schlick R, Liedke S, et al. Metastatic renal cell carcinoma (RCC): Spontaneous regression, long-term survival and late recurrence. Int Urol Nephrol. 1991;23:13–25.

10. Murphy KM, Travers P, Walport M. Janeway Immunologie. Springer Verlag Berlin Heidelb. 2014;

11. McLane, Laura M. Banerjee, Pinaki P. Cosma, Gabriela L. Makedonas, George Wherry, E. John Orange, Jordan S. Betts MR. Differential localization of T-bet and Eomes in CD8 T-cell memory populations. J Immunol. 2013;190:3207–15.

12. Takemoto N, Intlekofer AM, Northrup JT, Wherry EJ, Reiner SL. Cutting Edge: IL-12 Inversely Regulates T-bet and Eomesodermin Expression during Pathogen-Induced CD8+ T Cell Differentiation. J Immunol. 2006;177:7515–9.

13. Cruz-Guilloty F, Pipkin ME, Djuretic IM, Levanon D, Lotem J, Lichtenheld MG, et al. Runx3 and T-box proteins cooperate to establish the transcriptional program of effector CTLs. J Exp Med. 2009;206:51–9.

14. Knox JJ, Cosma GL, Betts MR, McLane LM. Characterization of T-bet and Eomes in peripheral human immune cells. Front Immunol. 2014;5:1–13.

15. Joshi NS, Cui W, Dominguez CX, Chen JH, Hand TW, Kaech SM. Increased Numbers of Preexisting Memory CD8 T Cells and Decreased T-bet Expression Can Restrain Terminal Differentiation of Secondary Effector and Memory CD8 T Cells. J Immunol. 2011;187:4068–76.

16. Intlekofer AM, Takemoto N, Wherry EJ, Longworth SA, Northrup JT, Palanivel VR, et al. Effector and memory CD8+ T cell fate coupled by T-bet and eomesodermin. Nat Immunol. 2005;6:1236–44.

17. Boomer JS, Green JM. An enigmatic tail of CD28 signaling. Cold Spring Harb Perspect Biol. 2010;2:1–20.

18. Merida I, Andrada E, Gharbi SI, Avila-Flores A. Redundant and specialized roles for diacylglycerol kinases and in the control of T cell functions. Sci Signal. 2015;8.

19. Weichhart T, Säemann MD. The multiple facets of mTOR in immunity. Trends Immunol. 2009;30:218–26.

20. Manning BD, Toker A. AKT/PKB Signaling: Navigating the Network. Cell. Elsevier Inc.; 2017;169:381–405.

21. Staron MM, Gray SM, Marshall HD, Parish IA, Chen JH, Perry CJ, et al. The Transcription Factor FoxO1 Sustains Expression of the Inhibitory Receptor PD-1 and Survival of Antiviral CD8+ T Cells during Chronic Infection. Immunity. 2014;

22. Cunningham M a, Zhu Q, Hammond JM. FoxO1a can alter cell cycle progression by regulating the nuclear localization of p27kip in granulosa cells. Mol Endocrinol. 2004;18:1756–67.

23. Martinez-Moreno M, Garcia-Lievana J, Soutar D, Torres-Ayuso P, Andrada E, Zhong XP, et al. FoxO-dependent regulation of diacylglycerol kinase alpha gene expression. Mol Cell Biol. 2012;32:4168–80.

24. Incheol Shin, F.Michael Yakes, Federico Rojo, Nah-Young Shin, Andrei V. Bakin JB& CLA. PKB/Akt mediates cell-cycle progression by phosphorylation of p27Kip1 at threonine 157 and modulation of its cellular localization. Nat Med. 2002;8:1145–52.

25. Liang J, Slingerland JM. Multiple Roles of the PI3K/PKB (Akt) Pathway in Cell Cycle Progression. Cell Cycle. 2003;2:336–42.

26. Koff A, Giordano A, Desai D, Yamashita K, Harper JW, Elledge S, et al. Formation and activation of a cyclin E-cdk2 complex during the G1 phase of the human cell cycle. Science. 1992;257:1689–94.

27. Sheaff RJ, Groudine M, Gordon M, Roberts JM, Clurman BE. Cyclin E-CDK2 is a regulator of p27Kip1. Genes Dev. 1997;11:1464–78.

28. Saxton RA, Sabatini DM. mTOR Signaling in Growth, Metabolism, and Disease. Cell. Elsevier Inc.; 2017;168:960–76.

29. Laplante M, Sabatini DM. mTOR signaling at a glance. J Cell Sci. 2009;122:3589–94.

30. Finlay DK, Rosenzweig E, Sinclair L V., Feijoo-Carnero C, Hukelmann JL, Rolf J, et al. PDK1 regulation of mTOR and hypoxia-inducible factor 1 integrate metabolism and migration of CD8 $^{+}$ T cells. J Exp Med. 2012;209:2441–53.

31. Michelle C. Mendoza, E. Emrah Er and JB. The Ras-ERK and PI3K-mTOR Pathways: Cross-talk Compensation. Trends Biochem Sci. 2012;36:320–8.

32. Śledzińska A, Menger L, Bergerhoff K, Peggs KS, Quezada SA. Negative immune checkpoints on T lymphocytes and cancer immunotherapy. Mol Oncol. 2015;9:1936–65.

33. Iouzalen N, Andreae S, Hannier S. LAP , a lymphocyte activation gene-3 (LAG-3) - associated protein that binds to a repeated EP motif in the intracellular region of LAG-3 , may participate in the down-regulation of the CD3/TCR activation pathway. 2001;3:2885-91.

34. Parry R V, Chemnitz JM, Frauwirth K a, Lanfranco AR, Braunstein I, Sumire V, et al. CTLA-4 and PD-1 Receptors Inhibit T-Cell Activation by Distinct Mechanisms CTLA-4 and PD-1 Receptors Inhibit T-Cell Activation by Distinct Mechanisms. Mol Cell Biol. 2005;25:9543-53.

35. Schwartz RH. T cell anergy. Annu Rev Immunol. 2003;21:305–34.

36. Jenkins BYMK, Schwartz RH. Antigen presentation by chemically modified splenocytes indcues antigen-specific T cell unresponsiveness in vitro and in vivo. 1987;165.

37. Gajewski TF, Qian D, Fields P, Fitch FW. Anergic T-lymphocyte clones have altered inositol phosphate, calcium, and tyrosine kinase signaling pathways. Proc Natl Acad Sci USA. 1994;91:38–42.

38. Krishna, Sruti Zhong X-P. Role of diacylglycerol kinases in T cell development and function. Crit Rev Immunol. 2013;33:97–118.

39. Moon EK, Wang LC, Dolfi D V., Wilson CB, Ranganathan R, Sun J, et al. Multifactorial T-cell hypofunction that is reversible can limit the efficacy of chimeric antigen receptor-transduced human T cells in solid tumors. Clin Cancer Res. 2014;20:4262–73.

40. Prinz PU, Mendler AN, Masouris I, Durner L, Oberneder R, Noessner E. High DGK-α and disabled MAPK pathways cause dysfunction of human tumor-infiltrating CD8+ T cells that is reversible by pharmacologic intervention. J Immunol. American Association of Immunologists; 2012;188:5990–6000.

41. Wherry EJ. T cell exhaustion. Nat Immunol. Nature Publishing Group; 2011;12:492–9.

42. Pauken KE, Wherry EJ. Overcoming T cell exhaustion in infection and cancer. Trends Immunol. 2015;36:265–76.

43. Blackburn SD, Shin H, Haining WN, Zou T, Workman CJ. Coregulation of CD8+ T cell exhaustion during chronic viral infection by multiple inhibitory receptors. Nat immunol. 2009;10:29–37.

44. Twyman-Saint Victor C, Rech AJ, Maity A, Rengan R, Pauken KE, Stelekati E, et al. Radiation and dual checkpoint blockade activate non-redundant immune mechanisms in cancer. Nature. 2015;520:373–7.

45. Noessner E, Brech D, Mendler AN, Masouris I, Schlenker R, Prinz PU. Intratumoral alterations of dendritic-cell differentiation and CD8+ T-cell anergy are immune escape mechanisms of clear cell renal cell carcinoma. 2012;1451–3.

46. Jantzer P, Schendel DJ. Human renal cell carcinoma antigen-specific CTLs: Antigen-driven selection and long-term persistence in vivo. Cancer Res. 1998;58:3078–86.

47. Chunhong Zheng, Liangtao Zheng, Jae-Kwang Yoo, Huahu Guo, Yuanyuan Zhang XG, Boxi Kang, Ruozhen Hu, Julie Y. Huang, Qiming Zhang, Zhouzerui Liu, Minghui Dong, Xueda Hu WO, Jirun Peng and ZZ. Landscape of Infiltrating T Cells in Liver Cancer Revealed by Single-Cell Sequencing. Cell. Elsevier; 2017;169:1342–1356.e16.

48. Fridman WH, Pagès F, Sautès-Fridman C, Galon J. The immune contexture in human tumours: impact on clinical outcome. Nat Rev Cancer. Nature Publishing Group; 2012;12:298–306.

49. Galon J, Costes A, Sanchez-Cabo F, Kirilovsky A, Mlecnik B, Lagorce-Pagès C, et al. Type, Density, and Location of Immune Cells Within Human Colorectal Tumors Predict Clinical Outcome. Science. 2006;313:1960–4.

50. Gladney GLB and WL. Immune escape mechanisms as a guid for cancer immunotherapy. Clin Cancer Res. 2015;21:687–92.

51. Lipson EJ. Durable tumor regression and successful re-induction therapy using anti-PD1 antibodies Re-orienting the immune system. 2013;1–3.

52. El-Khoueiry AB, Sangro B, Yau T, Crocenzi TS, Kudo M, Hsu C, et al. Nivolumab in patients with advanced hepatocellular carcinoma (CheckMate 040): an open-label, non-comparative, phase 1/2 dose escalation and expansion trial. Lancet. Elsevier Ltd; 2017;389:2492–502.

53. Motzer RJ, Escudier B, McDermott DF, George S, Hammers HJ, Srinivas S, et al. Nivolumab versus Everolimus in Advanced Renal-Cell Carcinoma. N Engl J Med. 2015;373:1803–13.

54. Cottu P, D'Hondt V, Dureau S, Lerebours F, Desmoulins I, Heudel P-E, et al. CheckMate 214: Efficacy and safety of nivolumab 1 ipilimumab (N1I) v sunitinib (S) for treatment-naı¨ve advanced or metastatic renal cell carcinoma (mRCC), including IMDC risk and PD-L1 expression subgroups. Ann Oncol. 2017;28:2017–8.

55. Motzer RJ, Tannir NM, McDermott DF, Arén Frontera O, Melichar B, Choueiri TK, et al. Nivolumab plus Ipilimumab versus Sunitinib in Advanced Renal-Cell Carcinoma. N Engl J Med. 2018;NEJMoa1712126.

56. Bedke J, Stühler V, Stenzl A, Brehmer B. Immunotherapy for kidney cancer: Status quo and the future. Curr Opin Urol. 2018;28:8–14.

57. Leitlinienprogramm Onkologie (Deutsche Krebsgesellschaft, Deutsche Krebshilfe, AWMF): Diagnostik, Therapie und Nachsorge des Nierenzellkarzinoms, Langversion 1.2, 2017, AWMF Registernummer: 043/017OL. Leitlinienprogr Onkol der Arbeitsgemeinschaft der Wissenschaftlichen Medi- zinischen Fachgesellschaften eV (AWMF), Dtsch Krebsgesellschaft eV und Dtsch Krebshilfe (DKH). 2017;1–219.

58. Greten TF, Malek NP, Schmidt S, Arends J, Bartenstein P, Bechstein W, et al. Leitlinienprogramm Onkologie (Deutsche Krebsgesellschaft, Deutsche Krebshilfe, AWMF): Diagnostik und Therapie des hepatozellulären Karzinoms, Langversion 1.0, AWMF Registrierungsnummer: 032-053OL. Leitlinienprogr Onkol der AWMF, Dtsch Krebsgesellschaft eV und Dtsch Krebshilfe eV. 2013;1–153.

59. Prieto J, Melero I, Sangro B. Immunological landscape and immunotherapy of hepatocellular carcinoma. Nat Rev Gastroenterol Hepatol. Nature Publishing Group; 2015;12:681–700.

60. Crispe IN. Hepatic T cells and liver tolerance. Nat Rev Immunol. 2003;3:51–62.

61. Knolle PA, Lohse AW, Gerken G. Endotoxin downregulates T cell activation by antigen-presenting liver sinusoidal endothelial cells. Hepatology. 1999;162:1401–7.

62. Böttcher JP, Schanz O, Wohlleber D, Abdullah Z, Debey-Pascher S, Staratschek-Jox A, et al. Liver-primed memory T cells generated under noninflammatory conditions provide anti-infectious immunity. Cell Rep. 2013;3:779–95.

63. Ringelhan M, Pfister D, O'Connor T, Pikarsky E, Heikenwalder M. The immunology of hepatocellular carcinoma. Nat Immunol. Springer US; 2018;19:222–32.

64. Escudier B, Sharma P, McDermott DF, George S, Hammers HJ, Srinivas S, et al. CheckMate 025 Randomized Phase 3 Study: Outcomes by Key Baseline Factors and Prior Therapy for Nivolumab Versus Everolimus in Advanced Renal Cell Carcinoma [Figure presented]. Eur Urol. European Association of Urology; 2017;72:962–71.

65. Thasler WE, Weiss TS, Schillhorn K, Stoll PT, Irrgang B, Jauch KW. Charitable state-controlled foundation human tissue and cell research: Ethic and legal aspects in the supply of surgically removed human tissue for research in the academic and commercial sector in Germany. Cell Tissue Bank. 2003;4:49–56.

66. Wilde S, Sommermeyer D, Frankenberger B, Schiemann M, Milosevic S, Spranger S, et al. Dendritic cells pulsed with RNA encoding allogeneic MHC and antigen induce T cells with superior antitumor activity and higher TCR functional avidity. Blood. 2009;114:2131–9.

67. Soos TJ, Sims TN, Barisoni L, Lin K, Littman DR, Dustin ML, et al. CX3CR1+interstitial dendritic cells form a contiguous network throughout the entire kidney. Kidney Int. Elsevier Masson SAS; 2006;70:591–6.

68. Sun C, Sun H, Xiao W, Zhang C, Tian Z. Natural killer cell dysfunction in hepatocellular carcinoma and NK cell-based immunotherapy. Acta Pharmacol Sin. Nature Publishing Group; 2015;36:1191–9.

69. Finke JH, Rayman P, Alexander J, Edinger M, Tubbs RR, Connelly R, et al. Characterization of the cytolytic activity of CD4+ and CD8+ tumor-infiltrating lymphocytes in human renal cell carcinoma. Cancer Res. 1990;50:2363–70.

70. Chatila, Talal, Silverman Lewis MR and GR. Mechanisms of T cell activation by the calcium ionophore ionomycin. J Immunol. 1989;143:1283–9.

71. Sobecki M, Mrouj K, Colinge J, Gerbe F, Jay P, Krasinska L, et al. Cell-cycle regulation accounts for variability in Ki-67 expression levels. Cancer Res. 2017;77:2722–34.

72. Nakano O, Sato M, Naito Y, Suzuki K, Orikasa S, Aizawa M, et al. Proliferative Activity of Intratumoral CD8 + T-Lymphocytes As a Prognostic Factor in Human Renal Cell Carcinoma : Clinicopathologic Demonstration of Antitumor Immunity Proliferative Activity of Intratumoral CD8+ T-Lymphocytes As a Prognostic Factor in Hu. Cancer Res. 2001;61:5132–6.

73. Urbani S, Amadei B, Tola D, Massari M, Schivazappa S, Missale G, et al. PD-1 Expression in Acute Hepatitis C Virus (HCV) Infection Is Associated with HCV-Specific CD8 Exhaustion. J Virol. 2006;80:11398–403.

74. Trautmann L, Janbazian L, Chomont N, Said EA, Gimmig S, Bessette B, et al. Upregulation of PD-1 expression on HIV-specific CD8+T cells leads to reversible immune dysfunction. Nat Med. 2006;12:1198–202.

75. Ahmadzadeh M, Johnson L a, Heemskerk B, Wunderlich JR, Dudley ME, White DE, et al. Tumor antigen-specific CD8 T cells infiltrating the tumor express high levels of PD-1 and are functionally impaired. Blood. 2009;114:1537–44.

76. Maki A, Matsuda M, Asakawa M, Kono H, Fujii H, Matsumoto Y. Decreased expression of CD28 coincides with the down-modulation z and augmentation of caspase-3 activity in T cells from of CD3z hepatocellular carcinoma-bearing patients and hepatitis C virus-infected patients. J Gastroenterol Hepatol. 2004;1348–56.

77. Borthwick NJ, Lowdell M, Salmon M, Akbar AN. Loss of CD28 expression on CD8(+) T cells is induced by IL-2 receptor gamma chain signalling cytokines and type I IFN, and increases susceptibility to activation-induced apoptosis. Int Immunol. 2000;12:1005–13.

78. Sherr CJ. G1 phase progression: Cycling on cue. Cell. 1994;79:551–5.

79. Sherr CJ, Roberts JM. Inhibitors of mammalian cyclin-dependent kinases. Genes Dev. 1995;1149–63.

80. Rao RR, Li Q, Shrikant PA. Fine-tuning CD8+ T cell functional responses: mTOR acts as a rheostat for regulating CD8+ T cell proliferation, survival and differentiation? Cell Cycle. 2010;9:2996–3001.

81. Oestreich KJ, Yoon H, Ahmed R, Boss JM. NFATc1 Regulates PD-1 Expression upon T Cell Activation 1. J Immunol. 2008;181:4832–9.

82. Blackburn SD, Shin H, Freeman GJ, Wherry EJ. Selective expansion of a subset of exhausted CD8 T cells by alphaPD-L1 blockade. Proc Natl Acad Sci U S A. 2008;105:15016–21.

83. Paley MA, Kroy DC, Odorizzi PM, Johnnidis JB, Dolfi V, Barnett BE, et al. Progenitor and Terminal Subsets of CD8+ T Cells Cooperate to Contain Chronic Viral Infection. 2012;338:1220–5.

84. Harari A, Enders FB, Cellerai C, Bart P-A, Pantaleo G. Distinct Profiles of Cytotoxic Granules in Memory CD8 T Cells Correlate with Function, Differentiation Stage, and Antigen Exposure. J Virol. 2009;83:2862–71.

85. Yang OO, Lin H, Dagarag M, Ng HL, Effros RB, Uittenbogaart CH. Decreased perforin and granzyme B expression in senescent HIV-1-specific cytotoxic T lymphocytes. Virology. 2005;332:16–9.

86. Couzin-Frankel J. Cancer Immunotherapy. Science. 2013;342:1432–3.

87. Azijli K, Stelloo E, Peters GJ, Van Den Eertwegh AJM. New developments in the treatment of metastatic melanoma: Immune checkpoint inhibitors and targeted therapies. Anticancer Res. 2014;34:1493–506.

88. Noy, Roy Pollarad WJ. Tumor-associated macrophages : from mechanisms to therapy. Immunity. 2014;41:49–61.

89. Liu Y, Cao X. The origin and function of tumor-associated macrophages. Cell Mol Immunol. 2015;12:1–4.

90. Schmidt N, Flecken T, Thimme R. Tumor-associated antigen specific CD8(+) T cells in hepatocellular carcinoma- a promising target for immunotherapy. Oncoimmunology. 2014;3.

91. Kalathil S, Lugade AA, Miller A, Iyer R, Thanavala Y. Higher frequencies of GARP+CTLA-4+Foxp3+ t regulatory cells and myeloid-derived suppressor cells in hepatocellular carcinoma patients are associated with impaired t-cell functionality. Cancer Res. 2013;73:2435–44.

92. Monu N, Frey AB. Suppression of proximal T cell receptor signaling and lytic function in CD8+ tumor-infiltrating T cells. Cancer Res. 2007;67:11447–54.

93. Kamphorst AO, Kamphorst AO, Wieland A, Nasti T, Yang S, Zhang R, et al. Rescue of exhausted CD8 T cells by PD-1 – targeted therapies is CD28-dependent. 2017;0683.

94. Meier R, Thelen M, Hemmings BA. Inactivation and dephosphorylation of protein kinase Ba (PKBa) promoted by hyperosmotic stress. EMBO J. 1999;17:7294–303.

95. Suizu F, Hiramuki Y, Okumura F, Matsuda M, Okumura AJ, Hirata N, et al. The E3 Ligase TTC3 Facilitates Ubiquitination and Degradation of Phosphorylated Akt. Dev Cell. Elsevier Ltd; 2009;17:800–10.

96. Rooney MS, Shukla SA, Wu CJ, Getz G, Hospital G, Diseases I, et al. Molecular and genetic properties of tumors associated with local immune cytolytic activity. Cell. 2015;160:48–61.

97. Unitt E, Rushbrook SM, Marshall A, Davies S, Gibbs P, Morris LS, et al. Compromised lymphocytes infiltrate hepatocellular carcinoma: The role of T-regulatory cells. Hepatology. 2005;41:722–30.

98. Brenchley JM, Karandikar NJ, Betts MR, Ambrozak DR, Hill BJ, Crotty LE, et al. Expression of CD57 defines replicative senescence and antigen-induced apoptotic death of CD8. Blood. 2003;101:2711–20.

99. Apetoh L, Smyth MJ, Drake CG, Abastado J-P, Apte RN, Ayyoub M, et al. Consensus nomenclature for CD8 $^{+}$ T cell phenotypes in cancer. Oncoimmunology. 2015;4:e998538.

100. Nunes C, Wong R, Mason M, Fegan C, Man S, Pepper C. Expansion of a CD8+PD-1+ replicative senescence phenotype in early stage CLL patients is associated with inverted CD4:CD8 ratios and disease progression. Clin Cancer Res. 2012;18:678–87.

101. Kao C, Oestreich KJ, Paley MA, Crawford A, Angelosanto JM, Ali MA, et al. Transcription factor T-bet represses expression of the inhibitory receptor PD-1 and sustains virus-specific CD8+ T cell responses during chronic infection. Nat Immunol. Nature Publishing Group; 2011;12:663–71.

102. Liu, Chau-Ching Rafii, Shahin Granelli-Piperno Angela, Trapani, Joseph A Young JD-E. Perforin and serine esterase gene expression in stimulated human T cells. J exp med. 1989;170:2105–18.

103. Wallin JJ, Bendell JC, Funke R, Sznol M, Korski K, Jones S, et al. Atezolizumab in combination with bevacizumab enhances antigen-specific T-cell migration in metastatic renal cell carcinoma. Nat Commun. 2016;7:1–8.

104. Zhu Y, Tchkonia T, Pirtskhalava T, Gower AC, Ding H, Giorgadze N, et al. The Achilles' heel of senescent cells: from transcriptome to senolytic drugs. Aging Cell. 2015;14:644–58.

11 Publications

Ramona Schlenker, Luis Felipe Olguín-Contreras, Matthias Leisegang, Julia Schnappinger, Anja Disovic, Svenja Rühland, Peter J. Nelson, Heinrich Leonhardt, Hartmann Harz, Susanne Wilde, Dolores J. Schendel, Wolfgang Uckert, Gerald Willimsky and Elfriede Noessner: **Chimeric PD-1:28 receptor upgrades low-avidity T cells and restores effector function of tumor-infiltrating lymphocytes for adoptive cell therapy.** *Cancer Research* 2017 Jul 1;77(13):3577-3590

Data of this thesis, in particular the analysis concerning T-bet, Eomes, PD-1, perforin and granzyme B, have been presented at Immunotherapy of Cancer Conference (ITOC) 2018 as oral presentation entitled:

“Immune landscape analysis to identify targets for immunotherapy across human carcinomas”.

The abstract has been published as follows:

J. Schnappinger, T. Straub, S. Lee, T. Schiergens, R. Oberneder, E. Noessner: **Immune landscape analysis to identify targets for immunotherapy across human carcinomas.** *European Journal of Cancer*, 2018 (92) Supplement 1, Page S1

12 Acknowledgements

Many thanks to Prof. Dr. Elfriede Nößner for making this thesis possible, her supervision, support, advise, patience, time and availability during day or nighttime – which cannot be taken for granted.

I am grateful to Prof. Dr. Mathias Heikenwälder and Prof. Dr. Percy Knolle, who were not only part of my thesis committee of HELENA organization but also helped moving this project forward by discussions, support and advice.

Many thanks to my colleagues, Anna Brandl and Carmen Amerhauser, who were of fantastic help with experimental issues when time was short and experimental settings and plans were large. Carmen Amerhauser made my life a lot easier by taking over some stimulation experiments based on the previously developed protocol. In return, I provided her with gating strategies and strategies of how to visualize the stimulation data in graphs that she used to create a great master thesis. Thanks a lot for our great collaboration!

I am thankful to Dr. Tobias Straub who helped with bioinformatics issues. I would also like to thank him for his time, our meetings and discussions; his input let the project grow.

I would like to thank Dr. Ralph Oberneder, Dr. Serene Lee, Maresa Demmel and their teams at the urological clinic Planegg and the Clinic of the LMU, Großhadern, for providing tissues. The cooperation went always smoothly.

I am thankful to my former colleagues Dr. Petra Prinz and Dr. Ramona Schlenker who introduced me to the field of tumor immunology. Many thanks to Dr. Petra Prinz who showed me that multi-parameter flow-cytometry is nothing to be afraid of.

Many thanks to Dr. Thomas Hofer who had always time for discussion and helped me with LSR II issues, settings and problems.

I would like to thank all colleagues I have met at the institute, Luis Olguin Contreras, Anja Disovic, Dr. Anna Mendler, Angelika Fischbeck, Anna Herbstritt, Svenja Rühland, Nadine Hömberg, Dr. Fatima Ahmelic, Anne Scheuerpflug, Dr. Dorothee Brech and all bachelor and master students that created such a great working atmosphere and delicious lunch/coffee/chocolate breaks that made life a lot easier.

Thank you, Thomas, for bearing strange working hours and moods, thanks for your encouragement, belief, motivation and help with small or large technical issues.

Foremost, I send many thanks to my parents for their support, love, belief and encouragement not only during this thesis but also during all my life. Without you, this thesis would not have been possible.

13 Affidavit

I herby declare that the submitted thesis “Profiling human tumor infiltrating leukocytes comparing renal cell and hepatocellular carcinoma” is my own work. I have only used the indicated sources and have not made unauthorized use of services of a third party. Where the work of others has been quoted or reproduced, the source is always given.

I further declare that the submitted thesis or parts thereof have not been presented as part of an examination degree to any other university.

Munich, 07/25/2018
Place, date

Julia Schnappinger